THE STUDY OF ULTRASONIC PULSE-ECHO SUBWAVELENGTH DEFECT DETECTION MECHANISM

BY

XIANGTAO YIN

B.S., Nanjing University, 1994
M.S., Nanjing University, 1997

THESIS

Submitted in partial fulfillment of the requirements
for the degree of Doctor of Philosophy in Electrical Engineering
in the Graduate College of the
University of Illinois at Urbana-Champaign, 2003

Urbana, Illinois

THE STUDY OF ULTRASONIC PULSE-ECHO
SUBWAVELENGTH DEFECT DETECTION MECHANISM

Xiangtao Yin, Ph.D.
Department of Electrical and Computer Engineering
University of Illinois at Urbana-Champaign, 2003
Dr. William D. O'Brien, Jr., Adviser

Popularly used flexible food packages are produced by hermetically heat-fusing the opposing seal surfaces to avoid postprocess contamination of the product. Seal integrity issues such as channel leaks and imperfect bonds must be inspected reliably and efficiently for food safety and quality assurance purpose.

The ultrasonic pulse-echo backscattered amplitude integral (BAI)-mode imaging technique has been developed to detect microchannels in flexible food package seals. Requiring no *a priori* sample information, this technique detects 38-μm-diameter channels reliably and 6-μm-diameter channels occasionally using a 17.3-MHz focused transducer in degassed water (20 ^{o}C, $\lambda \approx 86$ μm, total sample thickness 220 μm), which are in subwavelength scale and much smaller than human observer inspection limit ($\sim$50 μm). The technique can perform blind inspection and has the potential to become a real-time inspection methodology.

To bring the BAI-mode image closer to real world application, a zigzag raster scanning protocol has been proposed to simulate the real-time package product line inspection scenario. An experimental procedure was established to investigate the engineering trade-off between the BAI-mode image quality and the zigzag spatial

sampling pattern. Quantitative image quality assessment showed that the zigzag pattern prompted scanning speed and the optimal spatial sampling step size was between one and two times the -6-dB pulse-echo transducer focal beam lateral diameter.

A theoretical modeling study has been undertaken to understand the subwavelength channel defect detection mechanism associated with the BAI-mode image. A generalized impedance model was proposed through both microscopic optical imaging and acoustic impedance measurement of package sample cross-section. The validity of the generalized model was evaluated numerically by simulating the echo signal behaviors using finite-difference time-domain simulation. The normalized correlation coefficients between the simulated and the measured RF echo waveforms were greater than 95% for this generalized model.

In summary, the dissertation identified and solved two research challenges in ultrasonic pulse-echo nondestructive evaluation through both experimental and numerical approaches. The spatial sampling study will provide quantitative engineering guideline for real-time on-line package inspection implementation. The subwavelength defect detection mechanism study prompts our understanding about nondestructive characterization and evaluation of materials.

To my wife Lixin, for her love, encouragement and care over the years of my academic pursuit. To my dear parents, parents-in-law, my sister, and her family, for their great support during every step I have gone through in my life. To my grandma, who was unable to see the completion of my study. And last but not least, to my lovely son Ben, who brings so much joy in the journey of my life.

ACKNOWLEDGMENTS

I would like to express my gratitude to Dr. William D. O'Brien, Jr., my adviser, for his guidance, patience, encouragement and support during the course of my study in the Bioacoustics Research Laboratory at the University of Illinois. I would like to thank Dr. Scott A. Morris, my co-adviser, for his guidance, instructive discussion and help. I also thank to my committee members, Dr. Leon A. Frizzell and Dr. Andreas Cangellaris, for their advice and for reviewing this manuscript.

It is worth mentioning the individuals who worked in the ultrasonic food packaging inspection project: Dr. Kate Fraizer, Dr. Ayhan Ozgular, Baoshen Sun, Qi Tian, Neil Shah, Paul Rooney, and Jianrong Lin. Their contribution laid a solid ground for me to continue my dissertation research that is closely related with the project.

I would like to acknowledge the following individuals for their contributions to the completion of my study: Dr. James F. Zachary and Mr. James Blue for their professional assistance with optical microscopic images in Chapter 7; Dr. Michael L. Oelze for his discussion and help with the impedance measurement experiment in Chapter 7; Dr. Rita Miller for her help with experimental schedule and equipment preparation; Mr. Osama Nayfeh and Mr. Jason Windedahl for their assistance with data acquisition experiments in Chapter 5.

I would express my sincere appreciation to Ms. Sue Clay for her kind help during my study.

I am very grateful to Mark Haun, Tim Bigelow, Stacie Sakai, Jonathan Mamou, Yuhui Liu, Madhur Nigam, Eric Wort, and all other lab mates, for their friendship, advice, discussion and help. It is my great pleasure to work with and learn from them in the past two and half years.

Finally, I would like to thank Bioacoustics Research Laboratory, the Department of Electrical and Computer Engineering, the Food Packaging Laboratory, the Department of Food Science and Human Nutrition, and the Value-Added Research Opportunities Program, University of Illinois for providing the opportunities and financial aid to my academic pursuit and research practices.

It would be impossible to accomplish this dissertation without the above acknowledgments.

TABLE OF CONTENTS

CHAPTER **PAGE**

LIST OF FIGURES

FIGURE **PAGE**

LIST OF TABLES

TABLE **PAGE**

LIST OF ABBREVIATIONS

A/D	Analog-to-digital
ABC	Absorbing boundary condition
BAI	Backscattered amplitude integral
BEM	Boundary element method
BRL	Bioacoustics Research Laboratory
BW	Bandwidth
CNR	Contrast-to-noise ratio
DPI	Dot per inch
FDTD	Finite-difference time-domain
FEA	Finite element analysis
FEM	Finite element method
FVTD	Finite-volume time-domain
GPIB	General purpose interface bus
GUI	Graphic user interface
LSF	Line spread function
MRE	Meals ready to eat
MRI	Magnetic resonance imaging
NDE	Nondestructive evaluation
NDI	Nondestructive inspection
NDT	Nondestructive test
NFPA	National Food Processors Association
PII	Pulse intensity integral
PML	Perfectly matched layer
PRF	Pulse repetition frequency
PSF	Point spread function
PVDC	Polyvinylidene chloride
RF	Radio frequency
RFCE	RF correlation-entire range
RFCS	RF correlation-specific range
RFS	RF sample

ROC	Radius of curvature of a spherical focusing transducer
RTT	Round trip time
SLAM	Scanning laser acoustic microscopy
SNR	Signal-to-noise ratio
TOT	Time of transition
USDA	United States Department of Agriculture

LIST OF SYMBOLS

α	attenuation coefficient (frequency independent, dB/mm)
$\tilde{d}$	image lateral resolution definition
$\hbar$	thermal conductivity (W/(m·K))
κ	compressibility of medium (kg·m^{-1}·s^{-2})
λ	wavelength (m)
ω	radian frequency (rad/s)
π	a transcendental number, approximately 3.14159, that expresses the ratio of the circumference to the diameter of a circle.
ρ	mass density of medium (kg/m^3)
θ_i	incidence angle
θ_r	reflection angle
θ_t	refraction angle
$\Delta f_{(-3\text{dB})}$	-3-dB frequency bandwidth (Hz)
$BD_{(-6\text{dB})}$	-6-dB pulse-echo beam lateral diameter of a spherical focusing ultrasonic transducer (μm)
D	transducer diameter (mm)
F_L	focal length of a spherical focusing transducer (mm)
F_z	-6-dB pulse-echo depth of focus of a spherical focusing transducer (mm)
P	fluid or gas pressure (N/m^2)
Z	acoustic impedance of medium ($rayl$ = kg·m^2·s^{-1})
$\mathcal{T}$	temperature (K or $^{\circ}$C)
T	period (s)
$\mathbf{k}$	wave vector (rad/m)
$\mathbf{r}$	displacement vector (m)
$\mathbf{u}$	velocity vector (m/s)
c	speed of sound (m/s)
c_v	specific heat (J/(kg·K))
f	frequency (Hz)
$f^{\#}$	numerical aperture of transducer

f_0	center frequency (Hz)
p	acoustic pressure (N/m^2)
q'''	heat generation rate per unit volume
t	time (s)

CHAPTER 1

FUNDAMENTALS OF ULTRASONIC NONDESTRUCTIVE EVALUATION

This chapter presents a brief introduction to the nature of ultrasound, acoustic wave propagation, ultrasonic pulse-echo defect detection, and backscattered imaging techniques, which constitute the fundamentals for the rest of the chapters in this thesis.

1.1 Nature of Ultrasound

Sound is the rapid oscillatory motion of molecules and is produced when a body vibrates. A wave is a disturbance whose position in space changes with time. Sound propagates in waves. Unlike electromagnetic waves, which can travel in vacuum, the propagation of sound waves requires some physical elastic medium, such as gas, liquid or solid. Sound waves are of an elastic or mechanical nature. If a particle of the medium is displaced from its equilibrium position by any applied stress, internal forces tend to restore the system to its original equilibrium. Particles making up the medium are not propagating away from the disturbance source but are only vibrating back and forth about their equilibrium positions. Mechanical vibrations become vibrating pressure waves, transferring energy to the medium and to objects that the wave contacts by intimate contact between masses of the medium. The mechanical energy moves progressively from particle to particle when a sound wave propagates in a medium [1], [2].

There exist five major modes of sound waves in terms of their particle motion in relation to the sound wave propagation direction. The *longitudinal wave* is a compressional wave in which the particle motion is parallel to the wave propagation direction. The *transverse wave* is shear wave motion in which the particle motion is perpendicular to the wave propagation direction. *Surface waves* have an elliptical particle motion and travel across the surface of the material, with the major axis of the

ellipse perpendicular to wave propagation direction. *Plate (Lamb) waves* propagate in thin plates or specimen of uniform thickness less than a wavelength of the ultrasound introduced into it, resulting in flexural vibration of plate. *Torsion waves* occur in rods or wires when the driving source performs an oscillatory, twisting action about the rod axis. Longitudinal waves can propagate in any elastic/compressible medium (solid, liquid, or gas). However, the other wave modes barely propagate in liquids or gases [2]-[4] .

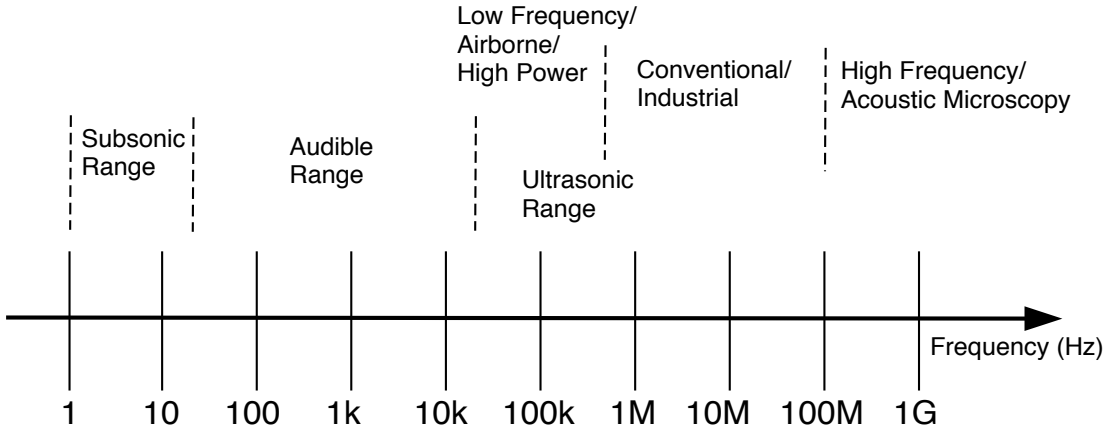

Figure 1.1 Acoustic spectrum.

Frequency is defined as the number of cycles per second of a harmonic vibrating disturbance. The acoustic spectrum breaks down sound into three ranges of frequencies: subsonic range, audible range, and ultrasonic range. Ultrasound wave refers to the human-inaudible sound wave whose frequency range is above 20 kHz, the upper frequency response limit of the human ear. The ultrasonic range is then further broken down into three subsections (Figure 1.1). Ultrasound behaves in a similar manner to audible sound except that it has a much shorter wavelength. The frequency range normally employed in ultrasonic nondestructive evaluation (NDE) is 100 kHz to 50 MHz. Therefore, it can reflect off very small surfaces such as defects inside materials. This property makes ultrasound useful for nondestructive testing of materials [4].

1.2 Ultrasonic Nondestructive Evaluation: Principles and Techniques

Ultrasonic NDE, also popularly referred to as nondestructive inspection (NDI) or nondestructive testing (NDT), applies low-intensity ultrasound waves to a test object to obtain information about the object without altering or damaging it in any way [4]. The use of low-amplitude ultrasound waves for signaling and testing purposes started early in the history of sonics. In 1929 and 1935, Sokolov studied the use of ultrasonic waves in detecting metal objects. Mulhauser, in 1931, obtained a patent[1] for using ultrasonic waves, using two transducers to detect flaws in solids. Firestone (1940) and Simons (1945) developed pulsed ultrasonic testing using a pulse-echo technique [5]. The testing of materials by means of ultrasonic waves has become a standard method within a few years of its introduction. Since the 1940s, the applications have been fully developed as transducer technology advanced and electronic circuitry became more sophisticated [2]. Nowadays ultrasonic NDE techniques have many popular applications for their capability to inspect defects and flaws embedded inside material in a nondestructive, fast, and inexpensive manner. Some typical examples are the determination of flaw size, shape, and distribution; inclusions; voids; cracks; delaminations; disbonds; and other departures from specifications. Other NDE applications include the determination of phase, microstructure, and nodularity; thickness; position; composition; anisotropy and texture; grain size in metals; stress and strain; acoustic emission; imaging; and holography [6], [7]. Ultrasonic NDE techniques have also been successfully applied to biomedical applications as a noninvasive technique to probe living tissue and generate diagnostic images for clinical usage [8]-[13].

The physical essences behind these applications are the mechanical interactions between ultrasonic waves and materials. Ultrasonic waves carry information about such interactions. Different ultrasonic wave modes are used for specific NDE applications. For example, a Rayleigh wave is useful for detecting surface defects because its energy penetration depth is approximately equal to one wavelength. Lamb

[1]German patent 569,598.

waves are good at detecting defects in plates and tubes. Longitudinal ultrasonic wave pulses are primarily used in NDE applications in fluids [2]-[4].

According to the means by which pulses are coupled into the test object, there are two major test methods: contact test and immersion test. In contact tests, acoustic pulses are coupled though a thin film of liquid as a coupling medium for the mechanical vibrations. In immersion tests, acoustic pulses are usually coupled through a substantial distance of liquid as a medium for mechanical wave propagation [3], [4].

As a key component in ultrasonic NDE applications, the transducer is an electro-to-mechanic device that can convert electrical energy into mechanical energy, in the form of ultrasound, for emitting an ultrasonic wave, and verse vice for receiving an ultrasonic wave [3]. The role of an ultrasonic transducer in an NDE system could be either as a transmitter that converts electrical signal to ultrasound and sends it out, or as a receiver which receives ultrasonic waves and converts them into electrical signals (RF waveforms).

According to the configuration of transmitter and receiver, NDT can be grouped as through-transmission test and pulse-echo test. Through-transmission testing involves two transducers on opposite sides of a test piece facing each other. One transducer works as a transmitter, while the other works as a receiver. Pulse-echo testing usually uses one single transducer as both transmitter and receiver [3].

The work in this thesis will focus on the immersion pulse-echo test techniques using longitudinal ultrasonic waves in fluid media. Unless specifically stated, the discussion in the rest of this thesis assumes longitudinal waves in fluid media.

1.3 Acoustic Wave Equation

A physical wave can be described in mathematical form. The acoustic wave equation in a fluid medium can be derived from three fundamental physical laws: conservation of mass (the equation of continuity (1.1)), momentum equation (the equation of motion (1.2)) and pressure-density relation for a perfect gas (the equation

of state (1.3)) [14]:

$$\frac{\partial \rho}{\partial t} + \nabla \cdot (\rho \mathbf{u}) = 0 \tag{1.1}$$

$$\rho \frac{\partial \mathbf{u}}{\partial t} + (\mathbf{u} \cdot \nabla)\mathbf{u} + \nabla \cdot P = 0 \tag{1.2}$$

$$P = K\rho^{\gamma} \tag{1.3}$$

where $\mathbf{u}$ is the particle velocity, P is the pressure, ρ is the mass density, K is a constant, and γ is the ratio of specific-heats ($\gamma = 1.4$ for air).

The medium is assumed to be ideal. That is, (1) the medium has no viscosity and energy dissipation; (2) the medium is quiescent when there is no acoustic disturbance; (3) the sound propagation process is adiabatic; and (4) the amplitude of the acoustic disturbance is very small compared to the ambient medium condition. The linear, lossless acoustic wave equation in fluids with phase speed c_0 can be written as [1], [14]

$$\nabla^2 p = \frac{1}{c_0^2} \frac{\partial^2 p}{\partial^2 t} \tag{1.4}$$

The variable $p = P - P_0$ is the acoustic pressure, where P_0 is the quiescent pressure in the ambient medium. The plane wave solution to (1.4) is

$$p(\mathbf{r}, t) = A \exp[j(\omega t - \mathbf{k} \cdot \mathbf{r})] \tag{1.5}$$

where $\omega = 2\pi f$ is the radian frequency, $\mathbf{r}$ is the location of the point (x, y, z) with respect to the origin of the coordinate system, and $\mathbf{k}$ is the propagation vector perpendicular to the constant-phase surface, which points in the wave propagation direction and has magnitude $|\omega/c_0|$. The phase speed c_0 is a real number for a lossless medium. A purely imaginary phase speed corresponds to an evanescent wave whose amplitude decays as the wave propagates. Therefore, the wave vector $\mathbf{k}$ could be a complex vector, with its real part representing a progressive wave and its imaginary part representing a nonprogressive wave.

1.4 Acoustic Properties of a Medium

The speed of sound and the mass density are fundamental acoustic properties of a medium. The propagation speed of a longitudinal sound wave in a fluid medium is defined as $c = \sqrt{1/\kappa\rho}$, where κ is the compressibility of the medium and ρ is the mass density of the medium. Generally, sound propagates faster in solids than in liquids and faster in liquids than in gases. The wavelength $\lambda = c/f$ equals the sound wave

propagation distance while medium particles finish one complete vibration cycle at frequency f [1].

In mechanics, a ratio of a force amplitude to a velocity amplitude is referred as an impedance [14]. Impedance was introduced into acoustics by Webster in 1914 [15] and independently by Kennelly and Kurokawa in 1921 [16]. The specific acoustic impedance of an acoustic field is defined as the ratio of acoustic pressure to the associated particle speed in a medium. The specific acoustic impedance for a plane wave is $Z = \pm\rho_0 c_0$, where ρ_0 is the mass density of the medium, c_0 is the propagation speed of the sound wave. The choice of sign depends on the propagation direction. The unit of specific acoustic impedance is kilogram per meter squared per second, also referred as *rayl* [1].[2] The characteristic acoustic impedance of a medium is defined as the product of the mass density ρ_0 and the speed of sound c_0 of the medium $Z_0 = \rho_0 c_0$. It also has the unit of *rayl*. The specific acoustic impedance for a plane wave equals the characteristic acoustic impedance of a medium.

1.5 Wave Propagation: Reflection and Refraction

When an acoustic wave traveling in one medium encounters the boundary of a second medium, reflected and transmitted (or refracted) waves are generated (Figure 1.2) [1]. At a boundary ($x = 0$), a portion of the sound may be transmitted to the second medium and the remainder reflected back to the first medium. Assuming that both the incident wave and the boundary between the two media are planar and that both media are fluids, the incident wave p_i, the reflected wave p_r and the transmitted wave p_t are all longitudinal waves (1.6).

$$\begin{aligned} p_i(\mathbf{r},t) &= \quad A\exp[j(\omega t - \mathbf{k_1}\cdot\mathbf{r}] \\ p_r(\mathbf{r},t) &= RA\exp[j(\omega t + \mathbf{k_1}\cdot\mathbf{r}] \\ p_i(\mathbf{r},t) &= TA\exp[j(\omega t - \mathbf{k_2}\cdot\mathbf{r}] \end{aligned} \tag{1.6}$$

where $\omega = 2\pi f$ is the radian frequency, R and T are the acoustic pressure reflection and transmission coefficients, respectively. The wave propagation vectors in media 1 and 2 are $\mathbf{k}_1 = \frac{\omega}{c_1}(\hat{i}\cos\theta_i + \hat{j}\sin\theta_i)$ and $\mathbf{k}_2 = \frac{\omega}{c_2}(\hat{i}\cos\theta_t + \hat{j}\sin\theta_t)$.

[2] The rayl is in honor of William Strutt and Baron Rayleigh (1842-1919).

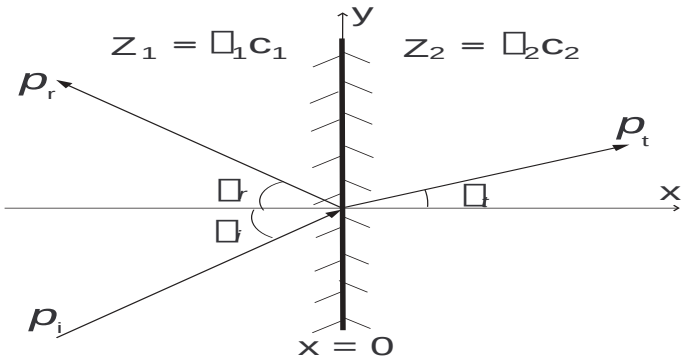

Figure 1.2 Reflection and refraction of a plane wave at the planar boundary between two fluid media.

The three waves in (1.6) must satisfy two boundary conditions at all points on the boundary: (1) The acoustic pressures on both sides of the boundary must be equal, and (2) The normal components of the particle velocities on both sides of the boundary must be equal. These two conditions state nothing but the continuity of normal specific acoustic impedance across the boundary. The acoustic pressure reflection (R) and transmission (T) coefficients (1.7) are solved from the two boundary conditions and Snell's law, which states that $k_1 \sin\theta_i = k_1 \sin\theta_r = k_2 \sin\theta_t$, where θ_i, θ_r and θ_t are the incidence, reflection and refraction angles, respectively [1].

$$R = \frac{\frac{Z_2}{\cos\theta_t} - \frac{Z_1}{\cos\theta_i}}{\frac{Z_2}{\cos\theta_t} + \frac{Z_1}{\cos\theta_i}}, \qquad T = 1 + R = 1 + \frac{\frac{Z_2}{\cos\theta_t} - \frac{Z_1}{\cos\theta_i}}{\frac{Z_2}{\cos\theta_t} + \frac{Z_1}{\cos\theta_i}} \tag{1.7}$$

The coefficients R and T depend on the characteristic impedance of both media and the incidence angle. At normal incidence ($\theta_i = 0$), they become

$$R = \frac{Z_2 - Z_1}{Z_2 + Z_1}, \qquad T = \frac{2Z_2}{Z_2 + Z_1} \tag{1.8}$$

1.6 Wave Propagation: Diffraction and Scattering

Diffraction at the source and scattering by obstacles are two factors that may cause the ultrasonic wave to spread or diverge in its propagation path in the medium. Diffraction is defined as the bending of waves around small obstacles and the spreading out of waves beyond small apertures. Diffraction occurs at the edge of a finite source aperture. Because an aperture has to be finite in reality, any practical sound wave that is radiated by a source will diffract eventually. Scattering may be defined as the change of amplitude, frequency, phase velocity, or direction

of propagation of a wave as a result of spatial or temporal nonuniformities of the medium. The inhomogeneities arise because of variations in compressibility or acoustic impedance differences [8]. The secondary sound spreads out in a variety of directions when scattering of the sound wave occurs [14], [17].

Scattering causes spatial redistribution of acoustic energy, which in turn changes signal amplitude. The scattering behavior depends on several factors such as absorption, acoustic impedance mismatch, spatial distribution and scale of inhomogeneities, shape of scatter, number of scatterers per unit volume and medium motion, and so on [8], [14], [17].

Absorption of ultrasound is defined as the transformation of ultrasonic energy to heat by frictional forces and heat conduction [8]. Absorption attenuates the signal amplitude. The energy loss mechanisms in ultrasound absorption are both classical and relaxational in nature [1], [18]. The higher the frequency, the greater the absorption in general.

Acoustic impedance mismatch occurs whenever there is a magnitude difference of speed of sound, mass density, or compressibility between the scatterer inhomogeneity and its surrounding medium. Greater mismatch means more significant inhomogeneity and produces stronger scattering.

The scale of inhomogeneities, including the size of scatterers and the interspacing between them, is often used to categorize different scattering phenomena. If the scale is significantly less than a wavelength, Rayleigh scattering occurs. If the scale is comparable to a wavelength, diffraction occurs. If the scale is very large compared to a wavelength and the surface roughness is small in scale compared to a wavelength, the object behaves like a polished surface (specular reflector) and geometric phenomena like reflection and refraction dominate.

The scattered acoustic energy distribution is affected by the shape of scatterers and their spatial distribution. Different scatterer shapes generate different scattering patterns in space and scattering cross section.[3] The spatial distribution of inhomogeneities, whether periodic, random, or intermediate between the two limits, produces either long-range or short-range scattering.

[3]The *scattering cross section* is defined as the power scattered per unit solid angle and per unit incident intensity. The scattering cross section depends on the distance between scatterer and receiver and the direction from scatterer to receiver [14].

Changes in the number of scatterers per unit volume also influence the echogenicity of the medium by multiple scattering. Multiple scattering affects the effective scattering cross section.

A scatterer's motion can cause a Doppler shift in the echo detected by a distant receiver. This in turn allows a deduction from the echo's frequency of one of the velocity components. The motion of the medium causes a frequency shift, echo modulation and temporal shift.

In ultrasonic NDE and biomedical applications, each of these factors affects scattering behavior. The physics behind these factors is the mechanical interaction between the acoustic disturbance and material composition and structure. Our understanding about material properties comes from analyzing the consequences induced by these factors.

1.7 Ultrasonic Transducer: Radiation and Reception

Piezoelectricity[4] was first discovered by the Curie brothers, Pierre and Jacques-Paul, in 1880 [3]. Piezoelectric materials are dielectric materials that produce charge when they are subjected to strain or produce strain when the electric field distribution across them is altered [8]. As the actual "front-end"of an NDE system, the ultrasonic transducer has dual roles by acting both as a radiation device to generate ultrasound from an electric signal and as a reception device to convert ultrasound to an electric signal.

The main components of a transducer are the active element, backing, and wear plate (Figure 1.3). The active element, which is piezoelectric or ferroelectric material, provides electric-mechanic energy transduction, and vice versa. The most commonly used piezoelectric materials are polarized ceramics. New materials such as piezo polymers and composites are also used for their benefit to transducer and system performance. The backing is usually a highly attenuating, high density material that absorbs the energy radiating from the back surface of the active element. It is used to increase the bandwidth of the transducer. For immersion applications, the wear

[4]The generation of electricity or of electric polarity in dielectric crystals subjected to mechanical stress, or the generation of stress in such crystals subjected to an applied voltage. Literally, *piezoelectricity* means "electricity due to pressure."

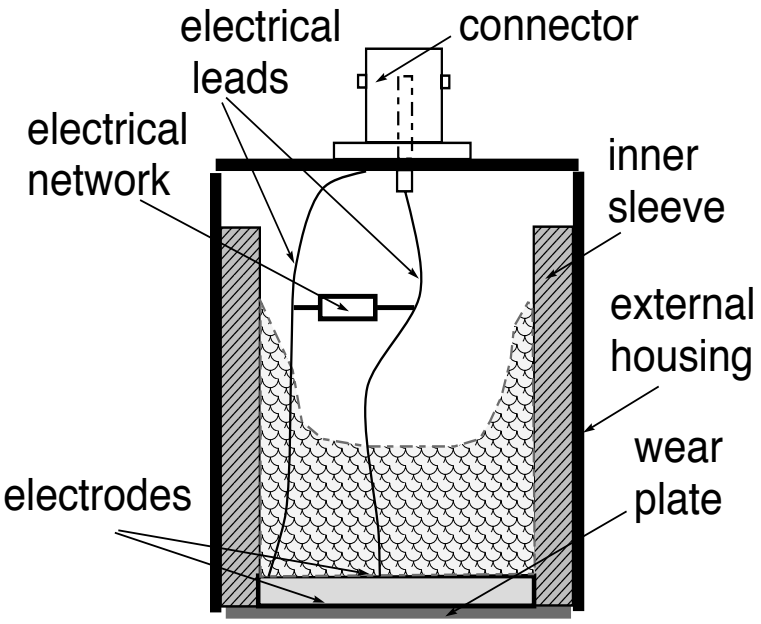

Figure 1.3 Transducer components.

plate not only provides protection to the active element but also serves as an acoustic impedance transformer between the high acoustic impedance of the active element and the low acoustic impedance of the liquid (usually a quarter-wavelength-thick matching layer to achieve in-phase output) [3], [4].

The electrical-to-mechanical energy transduction of ultrasonic transducers can be modeled by a three-port network called Mason's equivalent circuit, with two acoustic ports representing two surfaces of the active element and one electrical port. The coupling between the stress in the acoustic ports and voltage in the electrical port is modeled by an electromechanical transformer [17].

Unfocused transducer (plane piston transducer) emits an ultrasonic beam that spreads radially due to diffraction. The beam intensity falls off and the beam diameter is too large to obtain good lateral resolution when probing an object in the far field. Therefore, a focused acoustic beam is often employed, as in optics, to obtain good lateral resolution and high acoustic beam intensity at a point of interest [17]. The use of focused ultrasound pulse waves prompts inspection sensitivity because the ultrasound energy is concentrated in a focal region so that the response of the microstructure in this focal region to the incident ultrasound wave could be probed with high sensitivity.

Focused ultrasound pulse waves can be generated by a single element transducer with concave surface such as spherical or cylindrical surface which functions similarly to a focusing optical lens. There are essentially three approaches to focus an ultrasound beam: shaping the actual transducer vibrating element, attaching a concave lens to the transducer face, and inserting a biconvex lens into the ultrasound energy path which is similar to focusing the light from the sun using a magnifying glass [3].

The sound field of a transducer is a beam within which sound intensity varies. An unfocused beam can be divided into the near field and the far field. The near field is the region directly in front of the transducer where the echo amplitude goes through a series of maxima and minima and ends at the last axial maximum, at distance $N = D^2/4\lambda$ from the transducer, where D is the diameter of the transducer surface. The far field is the region at distances greater than N [3]. Attenuation is effectively a gradual loss of energy. The ultrasound beam attenuates as it progresses through a medium. Attenuation in the near field is associated with edge diffraction, absorption (friction and heat) and scattering. In far field, beam spread joins the three factors to attenuate sound intensity of the beam [3].

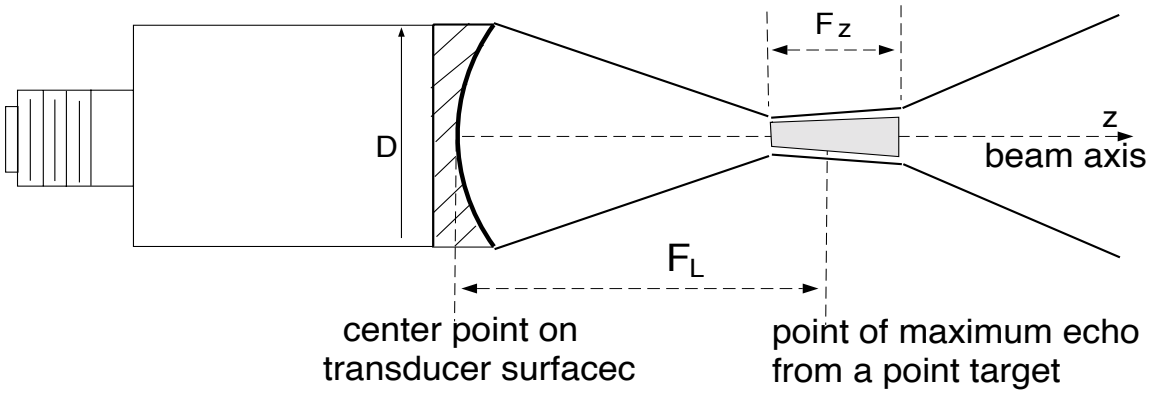

Figure 1.4 The beam of a spherical focusing transducer.

A spherical focusing transducer has the following important characteristics (Figure 1.4): diameter (D), focal length (F_L) which is the distance between the center point on transducer surface and the point of maximum echo from a point target, focal depth (F_z) which is the pulse-echo beam axial distance between two points whose echo amplitudes are -6 dB relative to the focal point amplitude, beam diameter ($BD_{(-6dB)}$) which is the -6-dB pulse-echo beam lateral diameter at F_L (Figure 1.4).

The numerical aperture of a transducer is defined as the ratio of its focal length to its diameter ($f^{\#} = F_L/D$). The waveform of a transducer has the following parameters: center frequency (f_0), -3-dB frequency bandwidth ($\Delta f_{(-3dB)}$), pulse duration (PD) which is the waveform duration at the -20 dB level or 10% amplitude of peak, pulse repetition frequency (PRF) which is the number of pulses produced per second. A transducer is often described by its waveform center frequency f_0, diameter D and numerical aperture $f^{\#}$.

The lateral acoustic pressure distribution in the focal plane ($z = ROC$, the transducer's curvature) of a spherical focusing transducer is described by [17]-[20]

$$\left|\frac{p(\rho = r, z = ROC)}{p(\rho = 0, z = ROC)}\right| = \left|\frac{2J_1(k\frac{D}{2}r)/ROC}{(k\frac{D}{2}r)/ROC}\right| \tag{1.9}$$

where the z axis is the beam axis originated at the transducer surface center point, and the ρ axis is the lateral axis. The axial acoustic pressure distribution of a spherical focusing transducer is described by [17]-[20]

$$\left|\frac{p(\rho = 0, z)}{p(\rho = 0, z = ROC)}\right| = \frac{ROC}{z}\left|sinc\left[\frac{D^2/4}{2\lambda ROC}\left(\frac{ROC}{z} - 1\right)\right]\right| \tag{1.10}$$

The -6-dB pulse-echo beam lateral diameter ($BD_{(-6\text{dB})}$)and the -6-dB pulse-echo beam axial focal depth (F_z) can be found through (1.9) and (1.10) as [17]

$$BD_{(-6dB)} = 1.028\lambda f^{\#} = 1.028\lambda\frac{F_L}{D} \tag{1.11}$$

$$F_z = 7.08\lambda f^{\#2} \tag{1.12}$$

1.8 Immersion Ultrasonic Pulse-Echo Detection

The ultrasonic pulse-echo detection technique has rapidly grown to be a generally accepted NDE technique in a very short time [2], [6], [7], [21]. Pulse-echo detection involves the generation of an ultrasound pulse wave by an ultrasonic source, the propagation of the ultrasound pulse wave, the reception of ultrasound echoes that are being bounced back by the targets to be detected, and the signal processing and interpretation of the RF echo waveform as well. Basically, in pulse-echo detection, an ultrasound beam is sent into a test object in which it travels without appreciable loss until it meets an obstacle. Echoes are generated when the ultrasound wave intercepts inhomogeneities in a medium which reflect part of the incident energy back to the receiver [2].

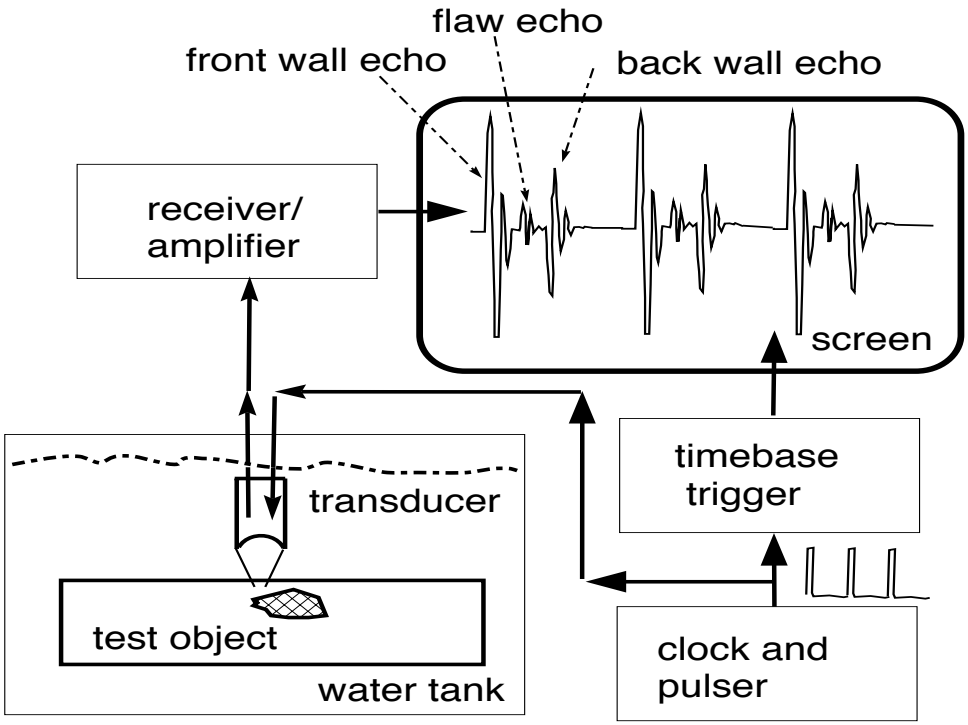

Figure 1.5 Immersion pulse-echo detection system.

A typical ultrasonic immersion pulse-echo detection system (Figure 1.5) consists of water tank, transducer, pulser (clock), receiver/amplifier and display (screen) [3]. The pulser generates a short, high-voltage pulse to excite the transducer while simultaneously supplying a voltage to the time-base trigger module. The transducer operates in transmit/receive mode, sending out an ultrasonic pulse into water and receiving echoes from the test object. The echoes are then converted to electrical voltages by the transducer, received, and amplified by the receiver/amplifier. The pulser generates a series of pulses at the pulse repetition frequency (PRF) so that repeated time-delayed pulses are used in the pulse-echo detection.[5] Synchronized by the trigger, the received electrical signals are displayed as a time sequence signal on the screen. The amplitude and the delay of these waveforms correspond with

[5]Compared with continuous wave signal, short echo-pulses generated by multiple reflections are less likely to overlay with each other because the pulse duration is finite. This is especially useful when the test object has multiple interfaces that are very close in space. The axial resolution is improved by using broadband pulses.

amplitude and arrival time of the echoes, which are proportional to the scattering strength and the distance of the targets. To acquire echoes at different positions over the test object, the transducer is usually mounted on a positioning system and moved with the positioning system.

In radar terminology, the pulse-echo detection setup is a monostatic configuration where the transmitter and the receiver are at the same or at closely spaced locations [14], [22]. An ultrasonic pulse-echo detection experiment is often called *backscattered measurement*. A spherical focusing transducer works as both transmitter and receiver. Generally, the amplitude of the backscattered echo indicates the scattering strength of a target, such as its size, shape, and the impedance difference between the target and its surrounding medium. Assuming constant speed of sound (c) in the medium, the arrival time (τ) of the backscattered echo tells the distance ($z(\tau)$) between the receiver and the target ($z(\tau) = c\tau/2$). The estimation of the distance and the target size is generally a difficult problem in practice considering medium inhomogeneity, noises, target motion, attenuation, multiple scattering.

Contact scanning techniques are mostly used for in-service inspection of small component areas and for scanning large components that cannot be moved to an immersion set-up. Immersion techniques are more convenient for scanning large areas of plates, pipes, and wrought products during manufacture with automated scanning and data acquisition systems. Immersion pulse-echo detection offers four major advantages over contact pulse-echo detection: (1) uniform coupling reduces sensitivity[6] variations, (2) reduction in scan time due to automated scanning, (3) focusing of immersion transducers increases sensitivity to small reflectors, and (4) improved near-surface resolution[7] and use of higher frequencies [3], [4]. However, the immersion pulse-echo technique requires that the test object be compatible with water or some other liquid. It is vulnerable to bubbles and system set-up is complicated [3].

1.9 Pulse-Echo Detection: Echo Signal Interpretation

The received RF echo waveforms require signal processing and interpretation to reveal information contained in the waveforms. Such information could be simply a

[6]See Section 1.9 for definition.

[7]See Section 1.9 for definition.

yes/no decision on whether or not there is a defect, or quantitative determination of defect location and size, attenuation coefficient in material, or target motion. To detect a defect (larger than one wavelength) in a homogeneous medium whose speed of sound is known, the echo arrival time and amplitude are needed. Because the speed of sound is known, the echo arrival time can be converted to distance information. If the defect interface is planar, the echo amplitude provides impedance mismatch information. However, not all echo signal interpretations are this straightforward. Complicated signal processing techniques are often employed to extract desired information. Quantitative NDE has always been a challenge for researchers for years. It is an inverse problem to reconstruct material geometry, properties and features through analyzing echo signals. A thorough understanding of the fundamental wave-structure interaction mechanisms will undoubtedly improve our NDE capability.

Ultrasonic pulse-echo detection has three typical signal representations. The A-scan utilizes a horizontal baseline to indicate pulse traveling distance (or time) and a vertical deflection from the baseline to indicate echo amplitude. The B-scan takes the same information, but displays a cross section of the test object, indicating the approximate length (as detected per scan) of reflectors and their relative positions. The C-scan takes the same information again, but presents it as a plane view of the test object and discontinuities from the front or in the same direction as the travel of the ultrasound [2], [3]. The B-scan requires the transducer to scan a row in the test object. The C-scan requires the transducer to scan an area of the test object at multiple positions. The scanning can be accomplished by using an automated positioning system to do mechanical scan or using the electronic focusing feature if a transducer array is used [23]. The B-scan and C-scan actually contain multiple A-scans, but they provide more intuitive information about the test object because echo waveform difference among these multiple A-scans can be easily observed by comparison.

Sensitivity is the ability of an ultrasonic system to detect defects at a given depth in a test material. The greater the signal that is received from these defects, the more sensitive the system. Sensitivity is a measure of the smallest reflector that produces a discernible signal on the display of an ultrasonic system.

The ability of an ultrasonic system to discriminate between two reflectors that are close together is called resolution [3]. Near surface resolution is the ability of the

ultrasonic system to detect defects located close to the surface of the test piece [4]. Axial resolution is the ability of an ultrasonic system to produce simultaneous and distinct indications from defects located at nearly the same position with respect to the sound beam. Axial resolution (1.13) depends on the transducer bandwidth but not on the center frequency [8]:

$$\tilde{d}_{axial} = 1.37/\triangle f_{(-3\text{dB})}(\text{mm}) \tag{1.13}$$

where $\triangle f$ is in megahertz. The broader the bandwidth, the better the axial resolution. In other words, it depends on the pulse duration. A shorter pulse duration provides better axial resolution. That is why short pulses are more popularly used than continuous wave in defect detection systems. Lateral resolution is the ability of an ultrasonic system to distinguish from defects located at nearly the same position with respect to the transverse direction of the sound beam. Lateral resolution of an ultrasound transducer depends on the size of the aperture in wavelengths. A -3-dB lateral resolution definition is

$$\tilde{d}_{lateral} = 1.02\lambda\frac{F_L}{D} \tag{1.14}$$

The larger the transducer diameter, the better the focus in general [3], [4], [8]. A detailed discussion on lateral resolution can be found in Section 1.10.

1.10 Ultrasonic Backscattered Imaging Techniques

Echo waveforms are acquired during a backscattered pulse-echo detection experiment. The results are usually presented in images that provide intuitive representation for people to know the material characteristics. Acoustic imaging techniques have successfully been used to detect voids, flaws, and cracks in epoxy-fiber composites, metals, and biological materials. Virtually all acoustic imaging techniques use pulse-echo techniques [24]. The ultrasonic pulse-echo imaging techniques are extensively used in biomedical applications [25], [26].

For backscattered pulse-echo detection, 2D ultrasonic images are mostly used. Mathematically, a 2D image refers to a 2D function $z = f(x, y)$, where x and y denote spatial coordinates and the value of f at any point (x, y) is proportional to the brightness of the image at that point. A 2D digital image $z_i = f(x_i, y_i)$ is the discretized version of $z = f(x, y)$ in spatial coordinates and in brightness. As the basic element in a digital image, a pixel is fully described by pixel value z_i, pixel

location (x_i, y_i) and pixel size that is the spatial coordinates discretization size. The pixel value z_i is the quantitative index of the brightness at point (x_i, y_i) [27].

To produce an ultrasonic backscattered pulse-echo image, one needs to construct a one-to-one mapping between certain a feature of the echo waveforms and the pixel value. Such a feature represents some physical property of the test medium. Mapping the echo waveform quantity to the image pixel value is usually a signal processing procedure. A very common and simple choice is to use the echo amplitude as the pixel value [3], which is a pictorial representation of the reflection coefficient. Another example of choice is to use the matched filter output amplitude [3], which is an illustration of the similarity between the echo waveform and the reference signal for the correlation operation. A much more complicated choice is to use the estimated parameter such as elasticity [28], [29].

One also needs to know the pixel locations in order to produce an image. The image plane could be either the transducer focal plane such as a C-scan image, or a plane containing the transducer beam axis such as a B-mode image. In the former case, the transducer performs a 2D scan in its lateral plane. The two axes of the resulting 2D image correspond with the two scan axes. In the latter case, the transducer does a 1D lateral scan. The resulting 2D image has two axes, one for the lateral scan row and the other for the time axis, which could be eventually converted to axial depth position if the sound speed of the medium is known.

The response of a linear system to a temporal impulse is called the impulse function of that system [30]. In optics, the impulse response is often called the point spread function (PSF), referring to a linear system response to a point source of light [31]. It is sometime called line spread function (LSF), referring to a linear system response to a line source of light. Borrowing the concept of PSF, a linear imaging system is fully characterized by its impulse function (PSF). The PSF is usually a curved smooth surface with spreading-out sidelobes which will output a degraded image of the true point source. It is a quantitative measurement of how much degradation an imaging system would produce for a point source. An ultrasonic pulse-echo backscattered imaging system can be treated as a linear system, where the input is the excitation pulse to the transducer and the output is the received echo waveform. The received echo waveform is the convolution between the input and the PSF. In image terms, the image pixel values represent the convolution output

between the test object and the PSF of the imaging system. The PSF is the key characteristic of an ultrasonic imaging system because it limits the image spatial resolution.

There are two types of image resolution: spatial and contrast [8]. Spatial resolution is associated with high-contrast objects in the image (such as two point reflectors). It is defined as the minimum separation permissible between two point reflectors that will produce two just-resolvable reflectors. Contrast resolution allows one to identify a region of echoes (reflectors) whose amplitude is slightly greater or less than the amplitude of the surrounding echoes (reflectors). It is associated with low-contrast objects in the image. Both types of image resolution find their counterparts in an ultrasonic pulse-echo detection system. Spatial resolution of an ultrasonic backscattered pulse-echo image has axial and lateral resolution. The contrast resolution corresponds with system sensitivity.

A transducer's transverse pressure distribution (1.9) on its focal plane has mainlobes and sidelobes. There are several lateral resolution definitions based on various mainlobe-sidelobe cancellation criteria for coherent[8] or incoherent imaging systems. The sources in a coherent imaging system work at the same single frequency. Therefore, the phase term cannot be ignored when calculating total intensity of coherent signals. On the other hand, an incoherent imaging system is a broadband system in which the total intensity is merely the summation of amplitude squares of these incoherent signals. An acoustic imaging system using very short pulses is, to a limited extent, an incoherent imaging system [17].

The most straightforward lateral resolution definition (1.15) is the -3-dB two-point definition which uses half-power criterion to distinguish two sources [17].

$$\tilde{d}_r(-3\text{dB}) = 1.02\lambda f^{\#} \tag{1.15}$$

The $\tilde{d}_r(-3\text{dB})$ equals transducer pulse-echo focal beam lateral diameter $BD_{(-6\text{dB})}$ (1.11).

It is more common to use the Rayleigh two-point definition, saying that two neighboring point sources can be distinguished from each other if the maximum

[8]Definition in physics: Of, relating to, or having waves with similar direction, amplitude, and phase that are capable of exhibiting interference.

response to one is located at the first zero of response to the second point. For two in-phase coherent sources with peak-null cancellation, the definition is [17]

$$\tilde{d}_{cr}(Rayleigh) = 1.22\lambda f^{\#} \tag{1.16}$$

The Rayleigh two-point criterion for incoherent imaging states that two points can be distinguished if there is a 26.5% dip in intensity at the midpoint between them [17].

$$\tilde{d}_{ir}(Rayleigh) = 1.22\lambda f^{\#} \tag{1.17}$$

for two incoherent sources, and

$$\tilde{d}_{cr}(Rayleigh) = 1.64\lambda f^{\#} \tag{1.18}$$

for two coherent in-phase sources. The use of incoherent sources improves the Rayleigh definition by a factor of 1.34 over the worst-case for coherent sources.

The Sparrow criterion says that the intensity halfway between the two points is just equal to the total intensity at one point [32]. Calculations define the Sparrow criteria as [17]

$$\tilde{d}_{ir}(Sparrow) = 1.02\lambda f^{\#} \tag{1.19}$$

for two incoherent sources, and

$$\tilde{d}_{cr}(Sparrow) = 1.42\lambda f^{\#} \tag{1.20}$$

for two coherent in-phase sources. The use of incoherent sources improves the Sparrow definition by a factor of 1.39 over the worst-case for coherent sources too.

Any erroneous information included in the ultrasonic image can be considered image noise. There are many sources of image noise. Electronic signals picked up by transducer structure or generated by system electronics mimic low-level echoes. The finite size of the sample volume and the coherent interference of the resulting echo signals at the transducer receiving aperture produce an image speckle pattern that reduces the sharpness of the high-contrast boundaries and limits the low-contrast region visualization [9]. Image noise jeopardizes image quality (resolution and contrast) and degrades system performance.

CHAPTER 2

SEAL INTEGRITY INSPECTION OF FLEXIBLE FOOD PACKAGES

This chapter briefly reviews the development of retortable flexible food packages. The increased use of flexible containers has created continuing concerns about food safety and package quality. The postprocessing contamination of the packaged foods are mostly related with seal integrity issues. Seal integrity inspection techniques are discussed and evaluated thereafter. A new nondestructive inspection modality that utilizes ultrasonic backscattered imaging techniques is recapped in the last two sections of this chapter.

2.1 Retortable Flexible Food Packages

Dating back to 1956, researchers at the University of Illinois proposed the concept of using retortable pouches to package food products [33]-[35]. Since then they have joined glass and metal containers to package and provide shelf-stable thermally processed food products [36], [37]. In 1979, the U.S. military started to replace the canned "C-Ration" with the retort pouch for the "meals ready to eat" (MRE) advantage [38], [39]. Scientific studies and consumer surveys have shown that flexible packages have many advantages over glass bottles or metal cans, such as better product quality and nutrition preservation for various types of foods [40]-[43], less energy consumption and processing time in manufacture [44]-[46], cheaper product shipping cost, less storage space requirement [36], and more enjoyable convenience [36], [39]. Retortable flexible food packages are gaining more and more popular usage nowadays for offering consumers cheap, lightweight, microwaveable, portable, durable and easy-opening and disposing-of soft containers [47].

Flexible food packages are produced by hermetically fusing opposing sheets on film seal surfaces. As an integrated step in modern retort food manufacturing systems, the closing of the flexible packages are usually done by heat fusing sheets

on plastic film seal surfaces [48]. Generally, the inner component of the plastic film structure is a thermoplastic material that softens with application of heat and pressure and solidifies when the source of heat is removed. Clamped by rigid heating bars, the outer surfaces of each film sheet immediately contacts the heating bars without melting and transmits heat to the sealing interface to join the two seal surfaces. The increased use of flexible containers has created continuing concerns about food safety and package quality. Container integrity has been well studied for traditional packages, particularly cans, for more than 60 years. But the understanding of factors affecting the integrity of plastic containers is still in its infancy [47], [49]. The Flexible Package Integrity Committee of the National Food Processors Association (NFPA) was established in 1984 as a response to the continuing concerns. The committee has divided seal defects in plastic containers into three main categories: critical, major, and minor defects. Critical defects are defects that cause the hermeticity loss of the container or evidence that there is, or has been, microbial growth in the package contents (such as channel leakers or nonbonding). Major defects are defects that bring about a container that does not show visible indications of having lost its hermetic seal but is defective such that it may have lost its hermetic seal, such as delamination, wrinkles, contaminated seals, or blisters. Minor defects are defects that have no adverse affect on the hermetic seals, such as stringly seal, crooked seal, delamination, or blisters. Some defects fall into both major and minor defect categories. That is, if the defect is pronounced, it becomes a major defect; otherwise if it is slight and does not affect hermeticity, it becomes a minor defect.

Seal integrity is defined as a seal continuum that is complete fusion in the sealing area with no discontinuities [47]. Sealing is the critical step in the production of flexible packages because post-process contamination of the processed products is frequently linked to seal integrity issues such as channel leakers and imperfect bonds [50]-[53]. Channel leakers provide pathways for microbial penetration from the external environment to the product inside, which results in product spoilage eventually. Imperfect bonds are generally caused by wrinkles, surface irregularities, delamination and product involvement in the seal area. They decrease seal strength and cause product deterioration during storage. Both of them are critical and major defects that are negative to seal integrity. The NFPA flexible package integrity

committee indicated that critical defects would be considered a potential public health problem. If these defects are found in any lot during the packaging or storage, the NFPA recommends a thorough inspection to ensure that no containers with broken hermetic seal are distributed. The package seal integrity must be tested for potential defects formed during or post production because poor seal integrity could cause product loss and compromise safety and public health, and the U.S. government is pressing for zero tolerance of pathogens in foods [50].

2.2 Channel Defects in Flexible Food Packages

Researchers are particularly interested in detecting channel defects in the seal area, which is the most hazardous critical defect allowing microbial contamination. Despite numerous efforts in the past years, the minimum detectable size that permits microbial contamination is still in question. Blakistone et al. [50] compiled a table (Table 2.1) for the minimum detectable sizes from the investigation done by various researchers. The table demonstrates a broad diameter variation of the critical channel defects ranging from 0.2 to 80 μm, possibly due to different experimental procedures. Although there is no standard procedure as to determining the minimum detectable size, a majority of these independent results (7 out of 11) shows that the minimum detectable size for critical channel defects is about 10 μm in diameter.

2.3 Overview of the Developed Methodologies

Package integrity testing can be divided into two categories: destructive and nondestructive testing. Destructive tests result in partial or complete loss of package and product. Nondestructive tests examine the package sample noninvasively such that they do not impair its usefulness for future applications. A detailed summary about the testing methods has been surveyed by Ozguler [49].

Nondestructive tests include methods for leak detection: biotests, bubble testing, dye penetration, electrolytic test; and methods for measuring seal structural integrity testing: burst testing, compression test, drop/impact tests, tear/tensile testing, and vibration test. Destructive tests are good at examining the seal strength of the package. However, they are not good indicators of a loss in seal integrity because they cannot detect channel microleaks reliably. For example, a food-plugged channel

Table 2.1 Critical defect diameter for bacterial penetration

Defect Diameter (μm)	Experimental Procedure	Year
10	Predictive equation [54]	1994
0.2	Filtration of certain water borne bacteria [55]	1980
11	Immersion test on pouches [56]	1980
$\sim$10	Aerosol test [57]	1995
$<$10	Immersion test [50]	1996
80	Electrolytic test on aseptic packages [58]	1990
22	Immersion test on pouches [59]	1989
10	Immersion test on vials [60]	1991
5	Spray in vials [60]	1991
$<$10	Biocell test [47]	1995
$<$7	Microperfusion test [61]	1994

leak will not let gas or liquid flow through during testing immediately after the seal is made. But the food product in the leak will provide a path for microorganisms to "grow through"the seal in the long run [56].

Commonly, food processing industry uses destructive testing and visual inspection to check package seal integrity [47], [62]. Destructive testing, such as burst testing and bubble testing, only provides statistical assurance, having no safety guarantee of untested packages [47]. Visual inspection suffers from unpredictable variation and human observation limit, e.g., the smallest possible channels detectable by human observers are about 50 μm in diameter in transparent food packages. However, independent studies [47] have shown that certain microorganisms can transit through 10-μm-diameter or smaller channels. And in reality, most plastic packages are imprinted with color ink for product description and decoration, which is an interference factor for visual inspection. Both destructive testing and visual inspection are time-consuming and expensive due to personnel costs, product loss and unsatisfactory defect detection rates. Effective and reliable nondestructive seal integrity tests are critically needed to ensure the safety and shelf life of the products in hermetically sealed flexible packages for quality assurance purposes.

Nondestructive tests span various NDT modalities, such as acoustics, eddy cur-

rent, infrared thermography, infrared laser, fiber optic array, capacitance, magnetic resonance imaging (MRI), machine vision imaging, pressure difference method, and X-ray. Although each of them has some application possibilities, only X-ray, MRI, and acoustics methods can detect microchannels in the seal region [47]. X-ray systems have excellent resolution (~ 30 μm) for water-filled microchannels but not for air-filled mircochannels [47]. MRI systems are unable to detect air-filled microchannels [47]. However, scanning laser acoustic microscopy (SLAM), an ultrasonic transmission technique, has shown promising performance in detecting microchannels (as small as 10 μm in diameter, at an ultrasonic frequency of 100 MHz) in seal region, regardless if they are water filled or air filled, transparent or opaque [63]. From a previous broad-scale survey [47] and trials of leak-detection methods, acoustic imaging was left, by elimination, as the best alternative for the development of a sensor which would provide the needed sensitivity, spatial resolution, and temporal resolution (when used as a dedicated linear scanning sensor to provide high feed-through speeds) [63]. Ultrasound offers a promising nondestructive testing modality for detecting microchannels in flexible food package seals.

2.4 Ultrasound Inspection of Flexible Food Packages: An NDE Application

The SLAM (Sonomicroscope 100, Sonoscan, Inc., Bensenville, IL) can characterize and image various materials and defects by exploiting the differences in acoustic (mechanical) transmission properties within different materials [63]. Although SLAM inspection has demonstrated the feasibility of using an acoustic microscope to accurately detect and characterize artificially created voids in a heat-sealed packaging system, the cumbersome equipment may prevent the SLAM from being a practical on-line inspection technique. A more practical approach is required to detect defects nondestructively in the seal region of flexible packages.

The Packaging Laboratory and the Bioacoustics Research Laboratory, both at the University of Illinois at Urbana-Champaign, have collaborated on the development of nondestructive ultrasonic pulse-echo detection methodologies for flexible food package seal integrity inspection [64], [65]. A transducer scanning motion control and data acquisition system (Appendix A) has been built for the project in the Bioacoustics Research Laboratory.

Using a 20-MHz spherical focusing transducer, the system can collect ultrasonic RF echo waveforms from the package channel defect sample (Appendix B) surface at each scan point. These waveforms construct a 3D ultrasound data set $\{p(x_i, y_i, t_j)$: scanning location $x_i, y_i \in$ planar sample surface to be scanned, sampling time instance $t_j \in [t_1, t_2], j = 0, 1, \cdots, 255\}$. The data set is stored as binary data files for off-line data processing and image formation on a Unix workstation using MATLAB (The Math Works, Inc., Natick, MA) [66]. By applying different signal processing and image formation strategies to the 3D ultrasound data set, several ultrasound pulse-echo detection and imaging methods for food package seal integrity inspection have been developed.

The RF sample (RFS) image aligns RF echo waveforms to pick up the pressure amplitude value at a specific depth in the sample and displays the pressure amplitude values as image pixel values [67]. The alignment requires accurate localization of the echo signal onset that involves with complicated operation if high accuracy is desired [68], [69]. Selecting a specific depth requires *a priori* knowledge of the packaging material, which has to be obtained off-line [67].

The RF correlation-entire (RFCE) range image and the RF correlation-specific (RFCS) range image map the correlation outputs at each scanning position to image pixel values [67]. The RFCS image differs from RFCE image in using a specific portion, rather than the entire range, of the RF echo waveform to do the correlation detection. This specific range usually covers the time portion corresponding with the channel defect region. Both correlation-based imaging techniques are matched filter detection techniques, which require a good *a priori* reference signal that should contain no delay and distortion introduced by an unknown defect. The shape distortion could cause the cross-correlation estimator to become biased and degrade its optimality [68], [70]. Such a "good" reference signal varies from sample to sample and is not always handy in real world experiments. Furthermore, the choice of correlation window length is critical for the RFCS technique. And the computational cost of correlation operation is expensive for real-time operation.

The parametric ARX-modeling imaging technique uses system identification theory to model the pulse-echo detection process between the pulse transmitting and the echo reception as a system impulse response function [71]. Assuming a linear ARX system model, the task becomes the estimation of the coefficients for

the parametric model. The image pixel value corresponds with the summation of the normalized absolute impulse response function at each transducer position. To achieve accurate estimation for multilayer structure of the package sample (Appendix B), the parametric model might have to be very complex, which inevitably results in expensive computational cost. Consequently, the parameter optimization becomes a troublesome mission.

Unlike RFS, RFCE, and RFCS, the backscattered amplitude integral (BAI)-mode imaging technique [72] requires little *a priori* knowledge about the sample. The single quantity used to construct the composite BAI-mode image is called the BAI-value, and is computed by integrating the RF echo signal envelope at each transducer sampling position. If a defect is present, the BAI-value will be different from that of the intact region because of a change in the backscattered signal. Both the ARX parametric-imaging technique and the BAI-mode imaging technique can perform blind detection. But the implementation of BAI-mode imaging is much simpler than that of the ARX parametric-imaging.

2.5 Observations

Table 2.2 shows the statistic evaluation of robustness based on the detection rate for water-filled and air-filled channel defects in two commonly used package materials: plastic and aluminum foil [67]. The air-filled channel defects represent high impedance difference. The water-filled channel defects represent low impedance difference.

From Table 2.2, all these methods are capable of detecting channel defects embedded in bonded 2-sheet package samples. The detectable channel defect sizes are much smaller than human observer inspection in all cases. It is observed that the detection rates of ARX are unstable for different materials. The ARX-mode image is material-dependent. For instance, the detection rate of the ARX-mode image for water-filled 38-μm-diameter channel in aluminum foil is zero out of five experiments. While the corresponding detection rate for water-filled 38-μm-diameter channel in a plastic sample is five out of five. It is also observed that the high impedance difference samples (channels in aluminum foil) are easier to detect than the low impedance samples (channels in plastic films). Except for ARX, the other three methods (RFS, RFCS, and BAI) have 100% detection rates for channels as

Table 2.2 Evaluation of robustness based on the detection rate for different channel defects

Channel defect type	Diameter (μm)	BAI	RFS	RFCS	ARX
water-filled plastic	50	5/5	5/5	5/5	5/5
	38	5/5	5/5	5/5	5/5
	15	2/7	3/7	5/7	5/7
	10	4/5	3/5	4/5	4/5
	6	1/4	1/4	2/4	1/4
Air-filled plastic	50	5/5	5/5	5/5	5/5
	38	5/5	5/5	5/5	5/5
	15	6/6	6/6	6/6	6/6
	10	3/5	3/5	5/5	4/5
	6	1/4	1/4	2/4	2/4
Water-filled aluminum foil	50	5/5	5/5	5/5	5/5
	38	5/5	5/5	5/5	0/5
	15	3/5	4/5	5/5	2/5
	10	0/6	5/6	4/6	2/6
	6	3/4	4/4	2/4	1/4
Air-filled aluminum foil	50	5/5	5/5	5/5	5/5
	38	5/5	5/5	5/5	2/5
	15	2/8	7/8	8/8	1/8
	10	4/5	4/5	5/5	5/5
	6	4/4	4/4	4/4	0/5

small as 38 μm in diameter in bonded 2-layer package samples. Both RFCS and RFS have improved detection rates relative to BAI for channels of 15 μm or smaller [67], with the disadvantage of requiring *a priori* knowledge and the price of increased implementation cost.

The ultrasound propagation speeds are about 1485 m/s, 2600 m/s (mean speed) and 6420 m/s [73] in 20 ^{o}C degassed water, plastic package film, and aluminum foil, respectively. The corresponding wavelengths at 17.3 MHz frequency are 86 μm, 150 μm, and 371 μm, respectively. Thus, these channels are in subwavelength scale. The ultrasonic pulse-echo detection techniques have subwavelength detection capability.

Compared with RFS, RFCS and ARX, the BAI-mode imaging technique utilizes the simplest concept and has the minimal implementation cost. The BAI-mode imaging technique has been demonstrated to detect channels as small as 38 μm in diameter in bonded two-sheet plastic film samples (thickness 110 μm per sheet) with 100% detection rate for the tested samples at the frequency of 17.3 MHz. The acoustic image formation process is quite simple and does not require a heavy computational burden. Moreover, channel defects as small as 6 μm in diameter could be detected occasionally [67], [71]. It has been found that there is a direct relationship between the defect size and BAI-mode image contrast (the difference between the mean BAI-values in defective and intact region). Different defect types and packaging materials have a significant impact on the BAI-mode image contrast [49], [73], [74].

These observations lead to a conclusion that the BAI-mode imaging technique is a simple, general pulse-echo blind detection method for microchannel defects in food package samples with a decent detection rate. It has the potential to be a fast on-line food package seal integrity inspection technique. For this reason, the BAI-mode imaging technique will be studied in this dissertation.

CHAPTER 3

UNKNOWNS AND CHALLENGES

It has been shown in Chapter 2 that the aforementioned ultrasonic pulse-echo detection techniques have superior channel defect detection capability than the conventional detection methods. For example, the ultrasonic pulse-echo techniques have excellent resolution (as small as 6 μm) for both water-filled and air-filled channels, while X-ray cannot detect air-filled channels and MRI is even unable to detect voids. The BAI-mode imaging technique has 100% detection rate for the 38-μm-diameter channels tested, which is much better than the human inspection limit ($\sim$50 μm). Not only can these developed methods detect the channel defects, but also they are able to locate the channel defects with a high degree of accuracy. The ultrasonic pulse-echo detection techniques can be further used to evaluate and improve the performance of the packaging machinery by studying the package sealing properties and identifying the packaging machinery system deficiency. Furthermore, unlike the traditional post-seal quality control techniques such as destructive testing and visual inspection, these ultrasonic pulse-echo detection techniques have the potential to inspect seal integrity in real-time and to become on-line quality assurance techniques.

Since the BAI-mode imaging technique has advantages over the other pulse-echo detection techniques aforementioned, this study will be focused on the development of the BAI-mode imaging technique.

3.1 How Can We Use BAI-Mode Imaging in On-Line Inspection?

There are a number of variables that can affect an ultrasonic examination, such as temperature, speed of sound, attenuation, frequency, grain size, resolution, couplant, surface conditions (roughness and curvature), transducer beam size, angle, bandwidth [3]. In an automated on-line package inspection system, dynamic variables

such as speed and acceleration of the ultrasonic transducer relative to the continuous speed of the inspection line might contribute mechanical noise, which would adversely affect the quality of the received RF echo waveforms and consequently the ultrasonic image quality such as lateral resolution and contrast. For example, the continuous motion of the sample could cause local turbulence in the degassed water. Such a local turbulence might produce time shifts and amplitude distortion when the transducer receives the ultrasonic echo signals. Or even worse, the transducer might not be able to collect the entire RF echo waveform if the sample moves too fast. To further develop the ultrasonic pulse-echo BAI-mode imaging technique for on-line inspection, the question comes out as "How can we use the BAI-mode imaging technique in real-time operation?"

The BAI-mode imaging technique makes it possible and promising to construct an appealing real-world food package integrity inspection system. The development of the fast and reliable real-time on-line food package inspection techniques would benefit the food industry in the sense of reducing product loss, extending the shelf life of the products, and thus improving the productivity. To achieve this goal, a real-time transducer spatial sampling pattern for the BAI-mode imaging has to be established. And the engineering trade-offs for the real-time operation must be studied.

There is an engineering trade-off for the BAI-mode image of channels embedded inside thin layered materials: image quality and transducer scanning speed. According to the discussion in 1.10, image quality can be quantitatively described by lateral resolution and contrast resolution for a C-scan-type[1] image like the BAI-mode image. The smaller the transducer beam size, the better the lateral resolution. Fast scanning speed reduces inspection time, which is desirable in on-line real-time inspection. Intuitively, increasing scan step size will improve scanning speed, but the image lateral resolution will drop. This is because the beam size is fixed for a given transducer and the spatial sampling becomes sparser as the scanning step size goes larger.

A real-time transducer spatial sampling pattern will be proposed in Chapter 4 to simulate the on-line food package inspection scenario. The engineering trade-off between the BAI-mode image quality (image contrast and lateral resolution) and

[1]See Section 1.9 for the definition of C-scan signal presentation.

the real-time transducer spatial sampling pattern will be studied in an experimental approach. We are particularly interested in the effects of the -6-dB pulse-echo focal beam size of an ultrasonic transducer on the real-time pulse-echo BAI-mode image quality. This is an engineering know-how study that will be described in detail in Chapter 5.

3.2 Why Do We "See" the Subwavelength Defect?

The BAI-mode image pixel values are associated with the BAI-values, which are indeed the indications of backscattered echo signal strength. The subwavelength defect detection capability shows that the BAI-mode imaging technique is sensitive to small scale scatterers. A region of impedance departure from its surrounding medium causes scattering [14]. But as the region is subwavelength in scale, the scattering strength will be very weak, compared with specular reflection from the large flat interfaces between package sample and water. Thus, the echo caused by the subwavelength channel would be expected to be weaker than the specular reflection echoes. The water-filled subwavelength channel in thin stratified package samples represents a small geometrical region with the minimum impedance departure from its surrounding medium (see Appendix B for package sample preparation details). Considering system noise and multiple reflections caused by package sublayer interfaces, such a small perturbation in stratified medium tends to be too weak to be probed by transducer.

Figure 3.1 displays two echoes collected in an experiment. The solid line is the echo from the intact region. The dashed line is the echo from the channel. The overall amplitude of the defect echo is smaller than the intact echo because of the wave propagation divergence caused by the small scatterer, not the specular reflection from a large flat surface. The two echoes have equal amplitude between time 16.82 μs and 16.92 μs, which corresponds to specular reflection from the package front wall facing the transducer. The specular reflection from the package sample back wall appears at around 17.01 μs. The time interval of 16.92 -17.01 μs is 0.09 μs, which corresponds to a distance of approximately 100 μm. (The average speed of sound in the plastic medium is 2500 m/s (Appendix B) and the time portion considers pulse-echo round-trip time).

Two interesting features about the echoes are observed in the time interval [16.92

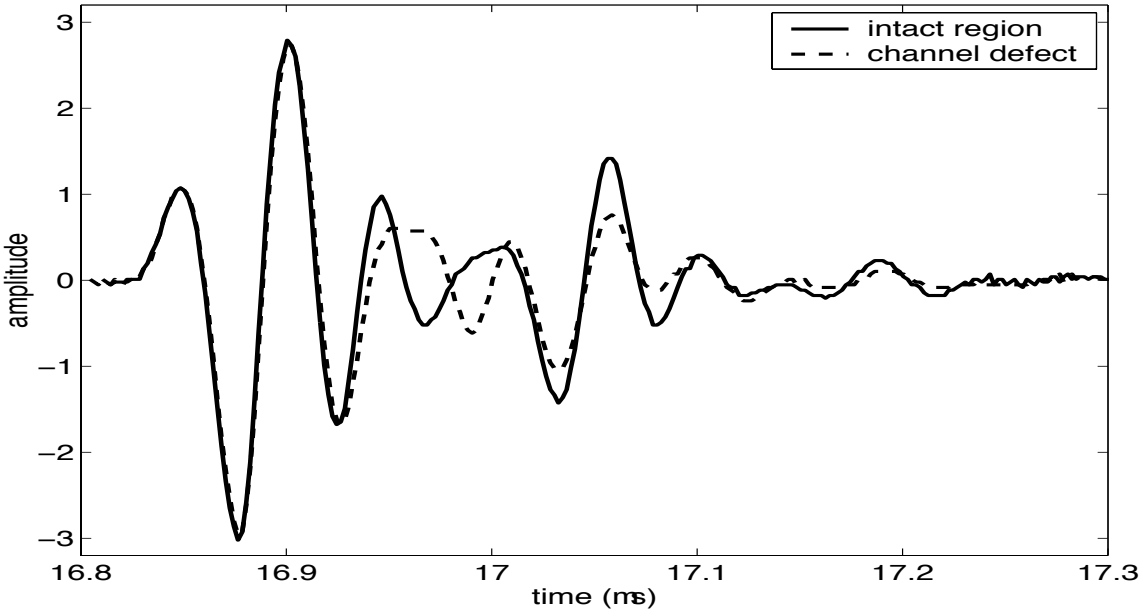

Figure 3.1 RF echo waveforms collected in experiment (from a water-filled 38-μm-diameter channel defect in 220-μm-thick plastic package, transducer frequency 17.3 MHz).

μs, 17.01 μs]. First, the intact echo amplitude is not zero. However, the corresponding spatial portion in the packaging sample is supposed to be homogeneous, which should not produce any echoes. "Is there any impedance mismatch in this region?" Second, it is clearly seen that the channel defect has an obvious influence on the backscattered echo in this time interval, indicating a significant echo amplitude change due to the subwavelength channel defect. As we know, the backscattered strength tends to be very little when the scatterer size approaches subwavelength. "Is a subwavelength channel defect itself alone able to produce such a significant echo amplitude change?"

It seems that the echo response of the channel defect to the ultrasound beam is not confined within its geometrical size (38-μm-diameter). What causes this elongation in time for the defect echo? Are there any other factors that could contribute to the defect echo portion? Is there any quantitative relationship between the defect echo time portion and the channel defect size? Or any criteria that could be used for quantitative characterization of the channel defect size or shape by looking at the amplitude difference between intact echo and defect echo. These subtle differences affect image quality, both in lateral resolution and in contrast

resolution. Then the question comes out as "Why do we see what we see?" The sensitive subwavelength defect detection performance of those developed pulse-echo defect detection techniques is poorly understood.

We are interested in why such a small subwavelength defect structure can be detected with the BAI-mode imaging technique. What factors would affect the echo waveform returned from the sample with subwavelength defect? We hypothesize that the defect sample microstructure, such as the bonding layer between the two plastic films and the impedance perturbation of the defect to the plastic film layers during the hermetical-sealing process, might be part of the answer. Because it is hard to control the defect sample microstructure as we wish during the hermetical-sealing process, numerical simulation will be a better approach to reveal the answer than experimental study. With the finite-difference time-domain (FDTD) method and the perfectly matched layer (PML) absorbing boundary technique, we have developed a numerical simulation tool to virtually implement the ultrasonic pulse-echo BAI-mode imaging technique in computer (Chapter 6). The hypothesis will be examined by experimentally characterizing channel defect sample (Chapter 7) and by numerical evaluation of the pulse-echo behavior according to a generalized channel defect sample microstructure model (Chapter 8). This will be a know-why study toward better understanding of the fundamental ultrasonic pulse-echo subwavelength defect detection mechanism.

3.3 Objective of the Study

The study in this dissertation aims to achieve a fundamental understanding of the mechanisms of the ultrasound pulse-echo NDE imaging techniques and bring them closer to real-world applications through both numerical simulation and experimental study.

CHAPTER 4

REAL-TIME SPATIAL SAMPLING

For on-line inspection purposes, a real-time zigzag raster scanning protocol is proposed in this chapter. This spatial sampling protocol requires a quantitative assessment when being adopted to the ultrasonic BAI-mode images. A quantitative BAI-mode image quality evaluation procedure for the zigzag scanning protocol is proposed in this chapter.

4.1 Toward Real-World Application: Real-Time Zigzag Raster Scan

The major differences between the real-world food package product line and the laboratory setting are the scale of the sealing region to be inspected and the product line speed. In our previous studies [67], [71]-[74], pulse-echo RF echo waveform data were acquired in a rectilinear stop-and-go transducer spatial sampling pattern (Figure 4.1(a)) over a 3 mm by 2 mm rectangular region. The dashed arrow lines are the transducer spatial scanning motion trajectories. The shaded circles represent the -6-dB pulse-echo focal beam spots. The transducer spatial sampling pattern refers to its spatial scanning pattern during the RF data acquisition over the sample. In this static pattern, the sample remains motionless in the y direction while the focused transducer scans the sample in the x direction. After the current scanning line is done (point A to B), the sample moves to another position (point C) for the next scanning line (point C to D) (Figure 4.1(a)). The equally distributed scanning grid in this static scanning pattern provides uniform spatial sampling lateral resolution, which is desirable in generating a high fidelity image. However, the stop-and-go behavior is impractical and costly for real-time product line package inspection because package product line motion is continuous. To inspect large packaging area more efficiently in time, a real-time spatial sampling pattern that does on-line nonstop detection would be more practical than the static pattern.

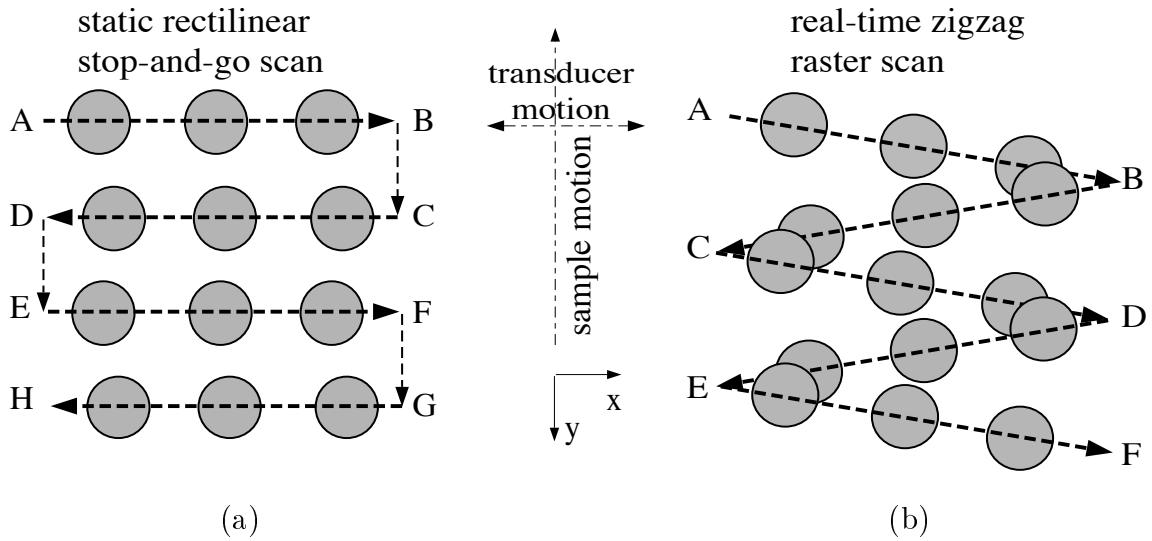

Figure 4.1 Static rectilinear stop-and-go scanning pattern (a) and real-time zigzag raster scanning pattern (b).

A new 2D scanning protocol is adopted to simulate a continuous on-line product line whereby an ultrasonic transducer scans a moving package in a zigzag raster pattern (Figure 4.1(b)). During RF data acquisition, the zigzag raster scanning pattern is produced by the spatial scanning motion where the package sample moves continuously in the y direction while the focused transducer moves back and forth in the x direction (Figure 4.1(b)). The combination of the sample motion and the transducer motion yields the zigzag raster pattern where the transducer moves from point A to B, B to C, and so on. Unlike the static rectilinear scanning pattern (Figure 4.1(a)), each scanning row of the real-time zigzag raster scanning pattern sweeps horizontally and vertically simultaneously.

4.2 Image Quality Evaluation

The feasibility of using the 2D real-time zigzag scanning pattern to detect channel defects has been demonstrated [75]. The acquired 3D ultrasonic data set (Appendix A) was reduced to a 2D matrix of BAI-values by backscattered amplitude integration on RF echo waveform envelopes. Because the zigzag scanning pattern was not in a rectilinear grid, a flexible interpolation technique was used to lay the BAI-values from the zigzag raster pattern onto a rectilinear grid for image formation. This was

accomplished by using the MATLAB function, "griddata()" with the "inverse distance interpolation" option [66], [76].[1]

The interpolated BAI-value matrix in rectilinear grid was normalized to the maximum BAI-value over the scan area. A gray-scale image was formed from this new normalized matrix (Figure 4.2).

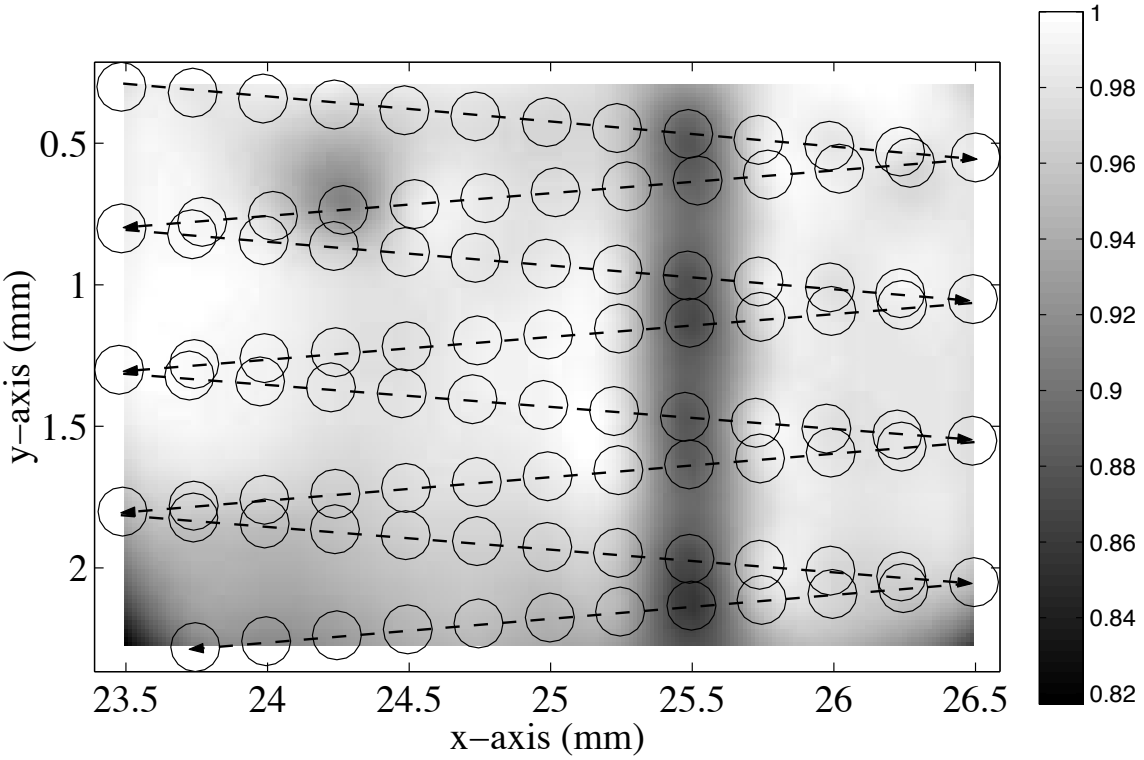

Figure 4.2 A BAI-mode image showing a 2D zigzag raster scanning pattern. The vertical black region at $x \approx 25.5$ mm is a 38-μm-diameter water-filled channel. Transducer scanning step size $x_{step} = 0.25$ mm (center-to center distance between two neighboring overlaid circles in the x direction), $y_{step} = 0.5$ mm (distance between two neighboring row turning points in the y direction). The circles overlaid on the zigzag raster pattern are the beam spots at transducer scanning locations.

Two statistical descriptors, the average BAI value difference (ΔBAI) between

[1]This option utilizes the biharmonic spline interpolation method, which is a very flexible algorithm to find the minimum curvature surface that passes through a set of nonuniformly spaced data points.

defective and intact regions and the contrast-to-noise ratio (CNR), are defined quantitatively to assess the BAI-mode image quality [67], [73]:

$$\mu_b = \frac{1}{N_b}\sum_{i=1}^{N_b} p_{b_i} \qquad \mu_d = \frac{1}{N_d}\sum_{i=1}^{N_d} p_{d_i} \tag{4.1}$$

$$\sigma_b = \left[\frac{1}{N_b}\sum_{i=1}^{N_b}(p_{b_i} - \mu_b)^2\right]^{\frac{1}{2}} \tag{4.2}$$

$$\Delta BAI = \frac{\mu_b - \mu_d}{\max_i\{p_i\}} \tag{4.3}$$

$$CNR = \frac{1}{\sigma_b}\frac{\mu_b - \mu_d}{\max_i\{p_i\} - \min_i\{p_i\}} \tag{4.4}$$

Subscripts b and d represent background (intact) and defective regions, respectively, and N_b and N_d are the total numbers of pixels in the background and the defective regions, respectively. Image pixel value p represents the corresponding BAI-value at the specific point. The terms μ_b and μ_d are mean BAI-values for background and defective regions, respectively, and σ_b is the standard deviation of the BAI-values for the background region.

The expression ΔBAI (4.3) is defined as the difference between the average BAI-values of the background and the defective regions, normalized by the maximum BAI-value in the image. It represents the sensitivity of the detection method to the RF echo signal variation between background and defective regions. In terms of the signal detection theory, the CNR can be viewed as a likelihood threshold of a binary hypothesis testing where the signal (BAI values in defective region) and the noise (BAI values in background region) are both modeled as Gaussian random variables. CNR (4.4) is the ratio of the average value difference between signal pixels and noise pixels to the overall dynamic range of the image pixels, divided by the standard deviation of the noise pixel values. In this sense, CNR is a measure of the robustness of the defect detection against noise. The higher the CNR is, the more distinguishable the defect image is. The pixels were selected by cropping separate rectangles in background and defective regions.

4.3 Spatial Sampling Resolution Study

It has been well known that for a pulse-echo image system, the image lateral resolution depends on the half-power beam width at transducer's focal plane [17], [77].

The Sparrow criterion for incoherent image states that the distance required to distinguish two points is defined as $d_{ir}(Sparrow) = 1.02\lambda f^{\#}$, where λ is the wavelength and $f^{\#}$ is the numerical aperture of the probe [32] (see Section 1.10 for detailed discussion). However, the image quality dependency between the probe spatial sampling step size and the probe beam width has not been studied in-depth, especially in the situation where both the target and the probe are in motion. In such a scenario, the spatial sampling pattern of the probe could affect image quality. There is an engineering trade-off between the BAI-mode image quality and the product line speed. Thus, to migrate the ultrasonic pulse-echo BAI-mode imaging technique from laboratory setting to real-world application, it is necessary to investigate this engineering trade-off. The real-time zigzag raster scanning pattern requires a quantitative evaluation of spatial sampling to form the BAI-mode image.

The purpose of the experimental study in Chapter 5 is to understand how the real-time zigzag raster pattern variables affect the ultrasonic pulse-echo BAI-mode image quality and thereby advance the BAI-mode imaging technique closer to being useful in real-world applications. In this study, two focused transducers were used to acquire RF data in a 2D zigzag raster scanning pattern from plastic film samples. The samples had point reflectors arranged in a rectilinear grid of varying center-to-center distances. Each point reflector produces a point spread function for evaluation of the ultrasonic imaging system. BAI-mode images were constructed with the experimental data collected by each transducer for each sample. Quantitatively, the contrast-to-noise ratio (CNR) and the average BAI-value difference (ΔBAI) between defective and intact regions were assessed to evaluate the image quality versus (1) the changing grid sizes (distance between adjacent point reflectors), (2) the changing transducer spatial scanning step sizes, and (3) the different ultrasonic focal beam spot sizes.

CHAPTER 5

EXPERIMENTAL SPATIAL SAMPLING STUDY

This chapter presents the experimental spatial sampling study on the ultrasonic pulse-echo BAI-mode imaging technique using the real-time zigzag raster transducer scanning pattern (see Section 4.1). Point-reflector array samples are prepared for image evaluation purposes. The experimental setup and procedure are then described. The BAI-mode images of the point-reflector array samples are obtained, and their image quality is evaluated quantitatively. Finally, the results are discussed, and the conclusion about the spatial sampling resolution criterion is proposed for the real-time zigzag scanning pattern.

5.1 Sample Preparation

Introduced by Adobe in 1985, Postscript is a programming language optimized for printing graphics and text with precise printing resolution up to a single toner dot size of a printer. In the experimental study, Postscript files were composed to generate the rectilinear point-reflector array pattern as shown in Figure 5.1. The point-reflector array samples were made by using a 1200-DPI (dot-per-inch) laser printer (Hewlett Packard LaserJet Series II-8100DN, Palo Alto, CA) to print the Postscript files on 114-μm-thick transparency films (CG5000 type, 3M Visual Systems Division, Austin, TX, ingredient: acrylate copolymer $< 94\%$, urea-formaldehyde polymer 1% - 5%, others $< 1.0\%$) (Figure 5.1). The diameter of each printed single toner dot is 21.2 μm (1/1200 inch) for a 1200-DPI laser printer. Each toner deposit is a solid circle with diameter of 127.2 μm (6 dots). The toner deposits formed a rectilinear point-reflector array with different grid sizes. The five samples, labeled from grid-a through grid-e, have grid spacings (center-to-center distances) 848, 742, 636, 530, and 424 μm (40, 35, 30, 25, and 20 dots), respectively.

The high-resolution rectilinear toner-deposit array provides a "template" of strong reflectors with nearly uniform target size and precise locations. It is desirable to have

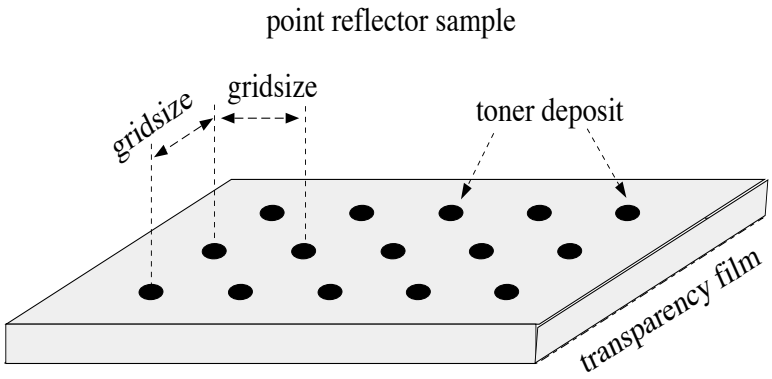

Figure 5.1 A point-reflector (toner-deposit) array sample on transparency film.

uniform targets because variation in individual target characteristics would cause variations in target echo waveforms, which are interference factors in image evaluation and comparison among different samples. Furthermore, the round-shaped deposits yield equal echo strengths in evaluating spatial sampling resolution in both the x and the y directions, rather than using defect channels whose target strengths are variable. Each point reflector produces a point spread function for evaluation of the ultrasonic imaging system, ideal for image evaluations (see Section 1.10). A preliminary study has demonstrated that the toner-deposit array sample is a suitable target for image quality study [78].

5.2 Experiments

Two focused transducers (labeled as TDR-A and TDR-B, Table 5.1) were characterized using the pulse-echo wire characterization technique [19]. They have similar operating frequency (TDR-A: 17.3 MHz and TDR-B: 20.3 MHz) but different beam width (-6-dB pulse-echo focal beam lateral diameters, TDR-A: 173 μm and TDR-B: 247 μm) and were used to acquire RF echo data in a zigzag raster pattern above from the five point-reflector array samples. Three spatial sampling variables were studied by using the two transducers to perform multiple scans over the five grid sizes of toner-deposit array samples with the 2D zigzag raster scanning pattern. For each transducer, the transducer scanning step size and the toner-deposit array grid size were varied, and the third spatial sampling variable was the -6-dB pulse-echo focal beam width.

Table 5.1 Characteristics of TDR-A and TDR-B transducers

Label	TDR-A	TDR-B
Model: Panametrics	V317	V317
Transducer diameter D (mm)	6.35	6.35
Numerical aperture $f^{\#}$	2	3
Center frequency f_0 (MHz)	17.3	20.3
Bandwidth $\Delta f_{(-3\text{dB})}$ (MHz)	7.35	7.09
Fractional BW	43.5%	34.8%
Focal length F_L (mm)	12.4	17.1
Pulse-echo round trip time RTT (μs)	16.8	23.0
-6-dB pulse-echo beam axial depth F_z (mm)	2.15	5.16
-6-dB pulse-echo beam lateral diameter $BD_{(-6\text{dB})}$ (μm)	173	247

The scanning area was a rectangle, 3 mm in the x direction and 2 mm in the y direction. The spatial scanning steps were variable in both x and y directions, denoted as x_{step} and y_{step} (Figure 5.2). The x_{step} was defined as the center-to-center distance between two adjacent data acquisition locations in the x direction. The y_{step} was defined as the travel distance in the y direction when the transducer completed one back-and-forth scan cycle in the x direction.

The measured x_{step} for the data set collected from toner-deposit array samples was 25 μm for all scans. Changing the x_{step} was simulated off-line by parsing step sizes at the desired sampling locations from the 3D ultrasound data set as described in Appendix A. For instance, to simulate a 50-μm x_{step} and a 100-μm x_{step} from the measured x_{step} of 25 μm, RF echo waveforms were parsed every two and every four sampling locations, respectively. The x_{step} was chosen to be 25, 50, 75, 100, 125, 150, 200, 250, 300, 375, 500, 600, 750, and 1000 μm, which corresponded with 121, 61, 41, 31, 25, 21, 16, 13, 11, 9, 7, 6, 5, and 4 sampling points evenly spanned in the 3-mm distance in the x direction, respectively. Figure 5.2(a)-(c) illustrates the oversampling, critical-sampling, and undersampling situations in the x direction compared to the -6-dB pulse-echo focal beam width. For each sample, y_{step} was set to be 200, 300, 400, and 500 μm. Note that the y_{step} is determined by the sample's continuous motion speed. The faster the sample moves, the larger the y_{step} is. Figure

5.2(d)-(f) demonstrates the effect of sample motion speed on the y_{step}. Thus, only four scans ($x_{step} = 25$ μm, $y_{step} = 200$, 300, 400, and 500 μm) were needed for each sample per transducer to cover 56 pairs of (x_{step}, y_{step}), which reduced data acquisition labor drastically.

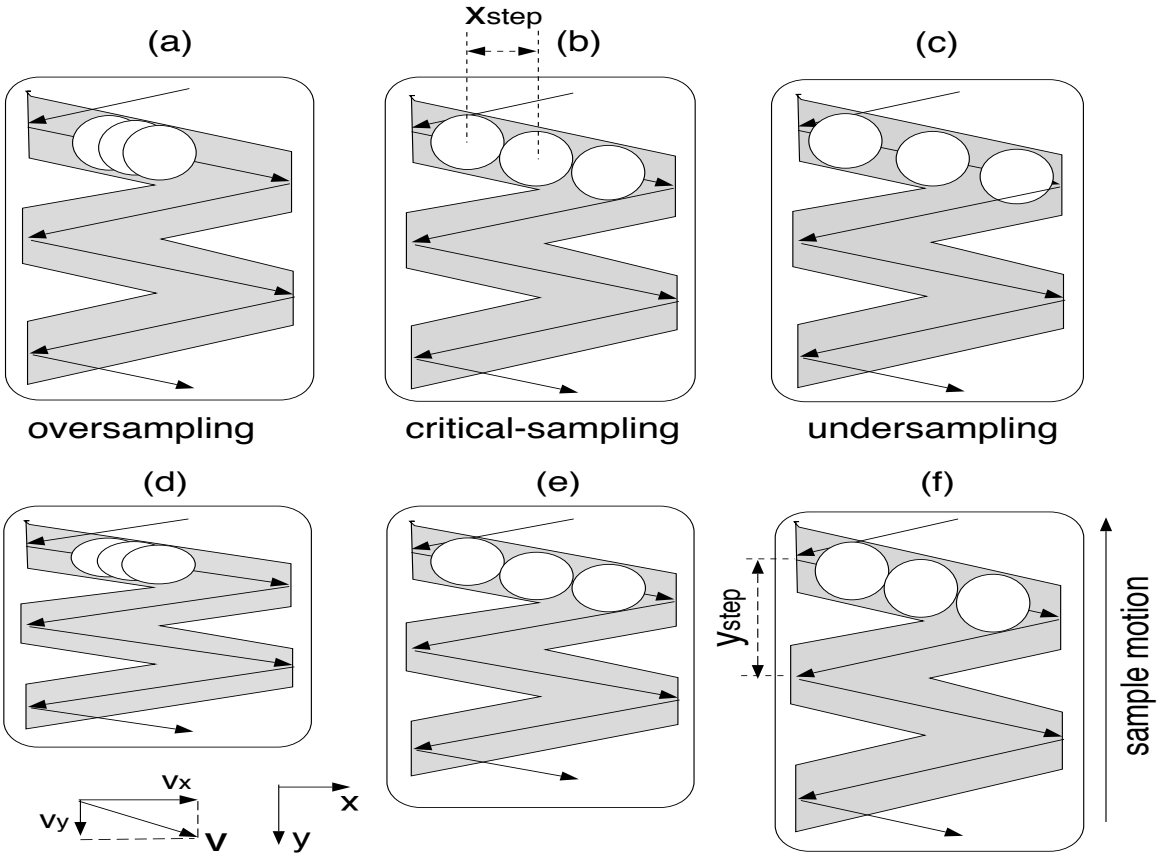

Figure 5.2 Changing x_{step} (a), (b), (c) and changing y_{step} (d), (e), (f).

The transducer's scanning motion velocity $\mathbf{v}$ has x and y components, v_x and v_y, which obey (5.1) for any given x_{step} and y_{step}:

$$\frac{v_y}{v_x} = \frac{y_{step}/2}{x_{step} \cdot (NS_x - 1)} = \frac{y_{step}}{2x_{total}} \qquad |\mathbf{v}| = \sqrt{v_x^2 + v_y^2} \tag{5.1}$$

where NS_x is the total number of sampling points in the x direction and x_{total} is the total transducer traveling distance in the x direction. In the experiments, the speed $|\mathbf{v}|$ was set to be 1 mm/s for all scans to allow ample time for the experimental system to acquire RF echo data. While in practice, the speed $|\mathbf{v}|$ could be much higher as long as the following two conditions are satisfied: (1) the time interval between two echo

receptions at neighboring spatial sampling locations is greater than the pulse-echo round trip time plus the echo pulse duration and (2) the data acquisition hardware speed is fast enough.

5.3 Results

Four real-time zigzag raster scans were performed for each of the five samples with each transducer. Figure 5.3 displays RF echo waveforms and their Hilbert transforms in two typical cases: the on-target case (solid-line waveform and dotted-line envelope) and the off-target case (dashed-line waveform and dash-dotted-line envelope). Because the point reflector (toner deposit) is on the top surface of the transparency film, the major amplitude variation occurs in the front part of the RF echo waveform.

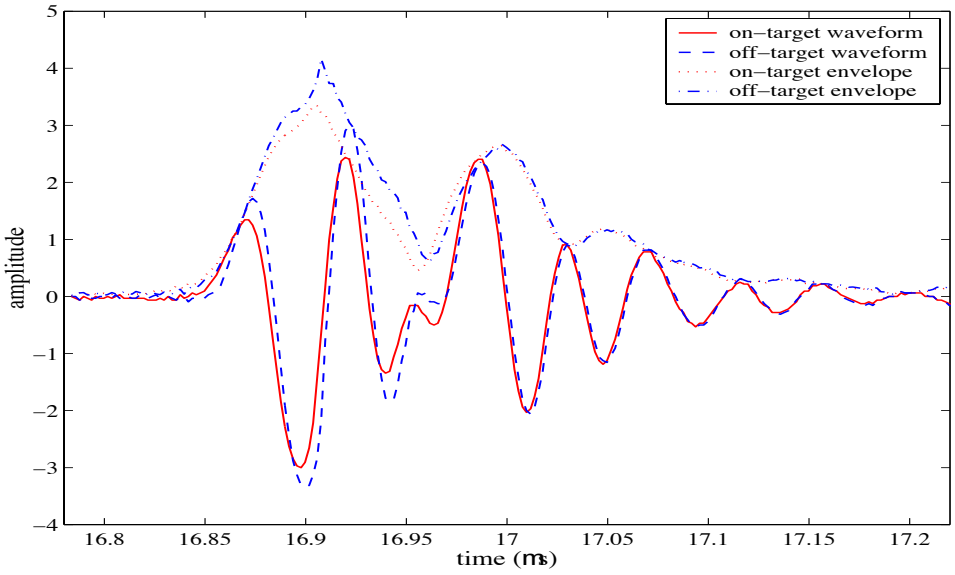

Figure 5.3 RF echo waveforms and their envelopes from point-reflector sample (single layer transparency film with a rectilinear toner-deposit array), using TDR-A.

Figure 5.4 shows an example of image quality as a function of x_{step} using TDR-A. The y_{step} is 200 μm. Each subimage displays the BAI-mode image for a different x_{step}. Subjective evaluation of the subimages showed that the image quality degraded as the x_{step} increased. Figure 5.5 further depicts the BAI-mode images for all five samples in the oversampled, critical-sampled, undersampled and extremely undersampled cases

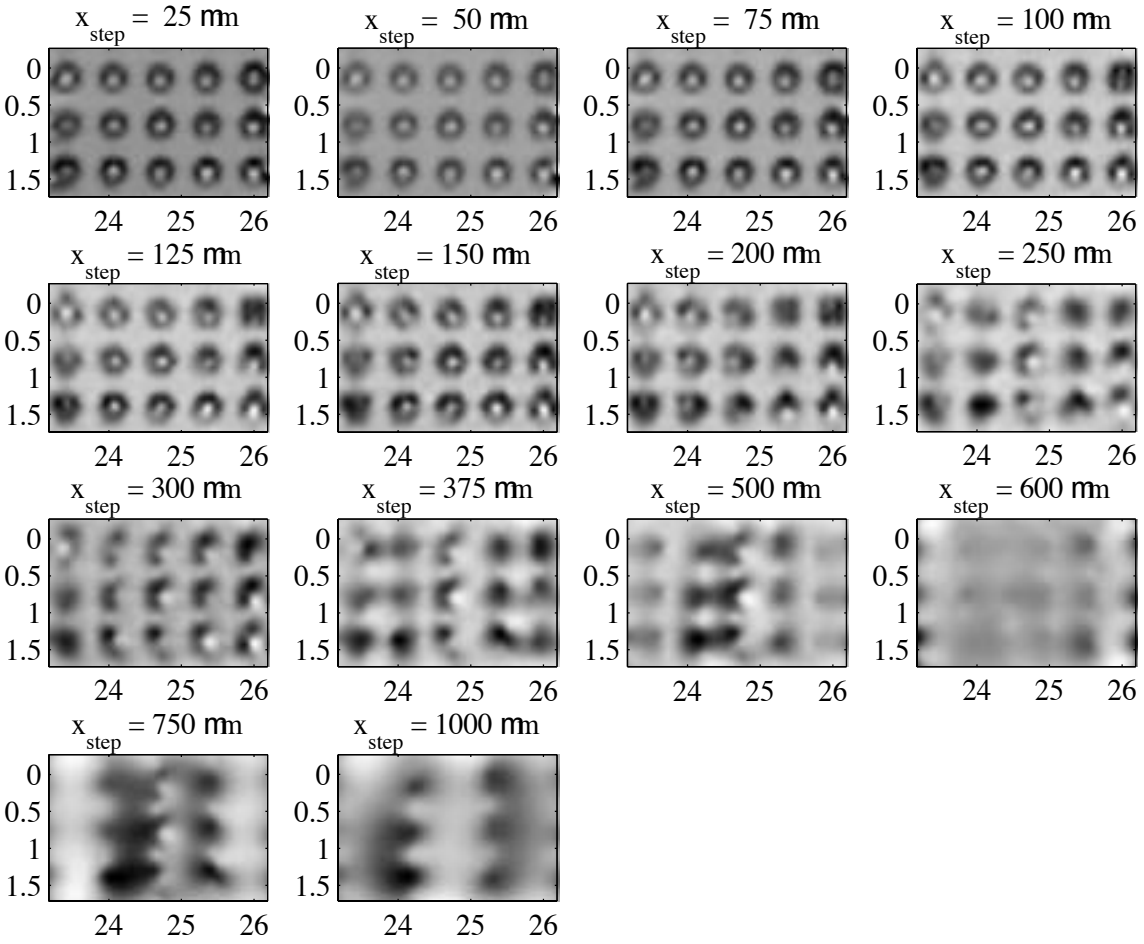

Figure 5.4 Simulation of changing x_{step} using TDR-A, y_{step} = 200 μm. For each subimage, the horizontal and the vertical dimensions are the x and y axes in mm, respectively.

using TDR-A. The y_{step} is 200 μm. As in Figure 5.4, the image quality degraded as the x_{step} increased for all five samples. Figure 5.6 shows the ΔBAI and CNR curves for sample grid-c versus the spatial scanning step sizes (x_{step} and y_{step}) for TDR-A.

Take the the BAI-mode images (Figure 5.4, x_{step} varies, y_{step} = 200 μm) and the corresponding ΔBAI and CNR curves (solid lines in Figure 5.6, y_{step} = 200 μm) as an example. For the oversampled cases ($x_{step} < 200$ μm), there was no significant change in image quality according to both subjective evaluation and quantitative assessment of the ΔBAI and CNR curves. Both curves appeared relatively flat when the x_{step} ranged in [25 μm, 200 μm]. For the undersampled cases ($x_{step} > 200$

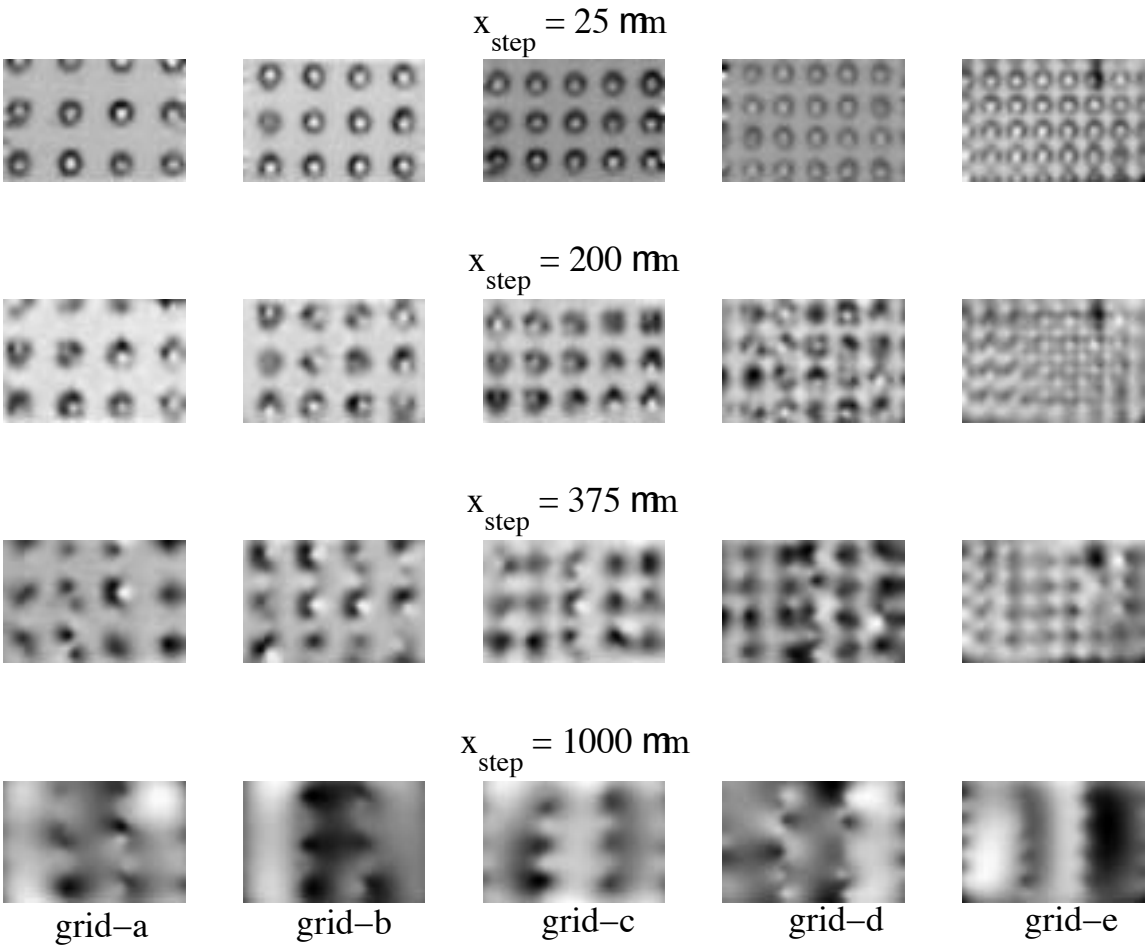

Figure 5.5 Comparison of oversampled (x_{step} = 25 μm), critical-sampled (x_{step} = 200 μm), undersampled (x_{step} = 375 μm) and extremely undersampled (x_{step} = 1000 μm) situations using TDR-A. y_{step} = 200 μm. Each column represents one of the five point-reflector array samples. Each subimage takes 3 mm by 2 mm rectangular area.

μm), the image quality degraded gradually but noticeably as the x_{step} increased. Subjective assessment shows that when x_{step} was greater than twice the beam width ($x_{step} > 375$ μm), the BAI-mode image started losing the true details of sample structure. After x_{step} exceeded 375 μm, the ΔBAI and CNR values degraded much faster than the value-dropping rate in the range of [200 μm, 375 μm]. But the array's point reflectors were detectable up to an x_{step} of 600 μm. Even when the x_{step} was 1 mm, the transducer was still able to detect some of the point reflectors, but this was only when the ultrasound beam happened to intercept the toner deposits.

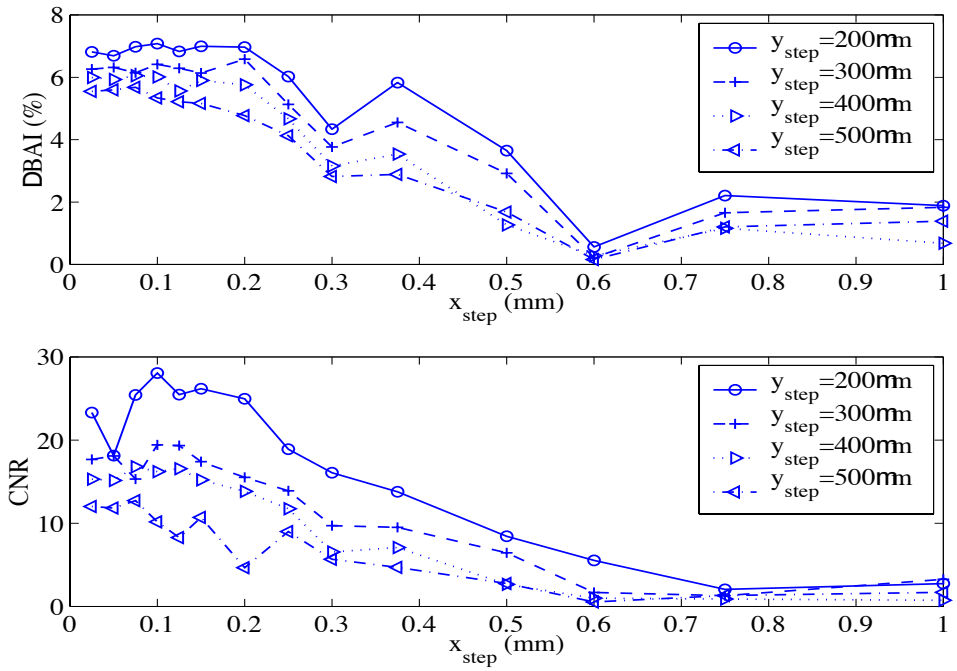

Figure 5.6 ΔBAI and CNR curves for varying spatial scanning step sizes using TDR-A. The four curves in each subplot represent the four different values for y_{step} (200, 300, 400, and 500 μm).

For a given point-reflector array grid size, the CNR and ΔBAI values degraded as scanning step size in each spatial dimension increased (Figure 5.6), as did the image quality (Figures 5.4 and 5.5). This observation was consistent with our previous spatial sampling study results for channel defects [75]. The BAI-mode image quality versus the y_{step} had been studied in [75]. This study extended the spatial sampling study in both the x and the y directions with pointlike targets (refer to Section 5.1), aiming to find the optimal spatial sampling step sizes in both directions by quantitative assessment. The ΔBAI curves dropped with different rates in the four different x_{step} intervals: no obvious degradation in [25 μm, 200 μm], moderate degradation in [200 μm, 375 μm], significant degradation in [375 μm, 600 μm] and abnormal enhancement in [600 μm, 1000 μm]. The CNR curves had the similar behavior as the x_{step} increased, except for the last interval [600 μm, 1000 μm] where the CNR curves went asymptotically flat.

Figure 5.7 shows the ΔBAI and CNR curves versus the point-reflector array grid size for TDR-A at y_{step} = 300 μm. The image quality was expected to degrade

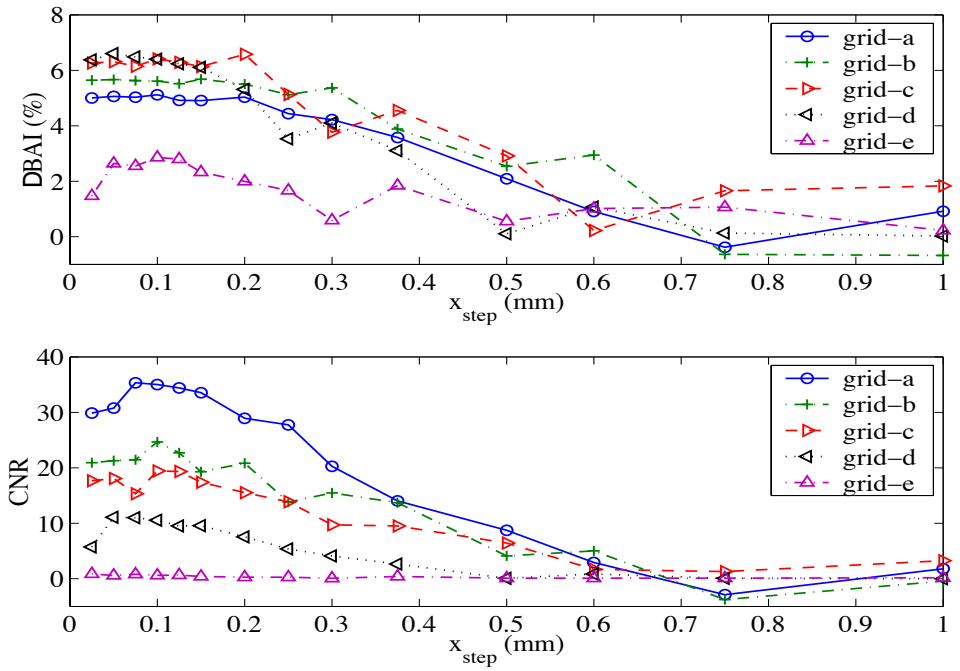

Figure 5.7 ΔBAI and CNR curves for different grid sizes using TDR-A. y_{step} = 300 μm. The five curves in each subplot represent the five samples with different grid size.

because it is more difficult to separate two toner deposits as the distance between them decreases. However, the ΔBAI curves (top plot) did not show a consistent decreasing pattern as the point-reflector array grid size reduced, i.e., the ΔBAI curve for sample grid-b was above the ΔBAI curve for grid sample grid-a, although the grid size of sample grid-b was smaller than that of sample grid-a. The CNR curves (lower plot) monotonically decreased as the point-reflector array grid size reduced.

As a comparative study of the focal beam spot diameter, the BAI-mode images using TDR-B were also obtained. Figure 5.8 shows the BAI-mode image quality as a function of y_{step} using TDR-A and TDR-B. The x_{step} is 100 μm. For the given x_{step}, the best image quality for TDR-A and TDR-B occurred when y_{step} = 200 μm and y_{step} = 300 μm, respectively. After y_{step} was greater than the beam width (173 μm for TDR-A and 247 μm for TDR-B), the BAI-mode image quality degraded as the y_{step} increased. As the spatial sampling in the y dimension became coarser, the point reflectors showed position shift and size distortion. But the three point reflectors in the middle column had less position shift and size distortion than other point-reflector

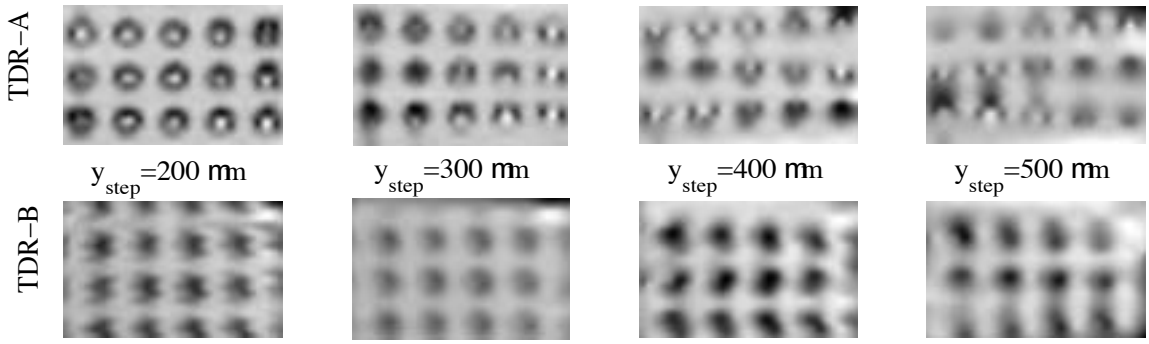

Figure 5.8 Comparison of the BAI-mode images with changing y_{step} using TDR-A (top) and TDR-B (bottom), x_{step} = 100 μm. Each subimage takes 3 mm by 2 mm rectangular area.

columns. The spatial sampling density (the overlap extent of the beam spots) of the zigzag raster pattern was higher in the central part than on the left and right margin of the image.

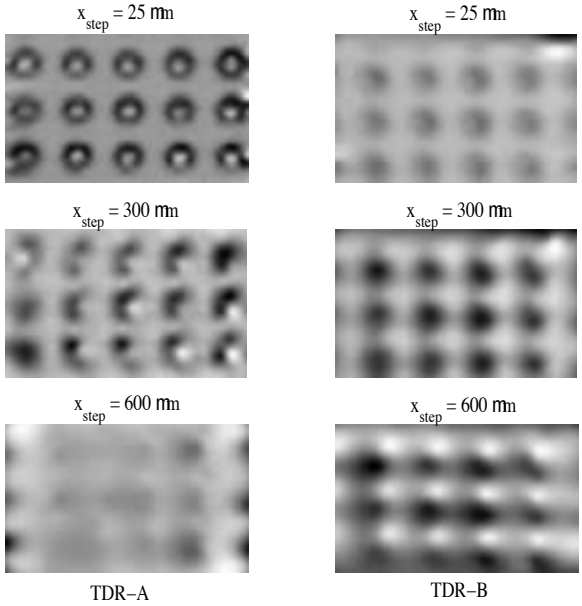

Figure 5.9 Comparison of the BAI-mode images with changing x_{step} using TDR-A (left, y_{step} = 200 μm) and TDR-B (right, y_{step} = 300 μm). Each subimage takes 3 mm by 2 mm rectangular area.

Figure 5.9 compares the BAI-mode images using both transducers. The left three images were constructed by using TDR-A with x_{step} = 25, 300, and 600 μm, y_{step}

= 200 μm. The right three images were constructed by using TDR-B with x_{step} = 25, 300, and 600 μm, y_{step} = 300 μm. In the oversampled case (x_{step} = 25 μm), the BAI-mode image obtained by TDR-A showed better details of each toner deposit than the BAI-mode image obtained by TDR-B because of the smaller beam width of TDR-A. But the toner-deposit array pattern was more clearly detected by TDR-B than by TDR-A when the x_{step} increased. This is because TDR-B has a larger beam width so that the ratio change of the scanning step size to the beam width is less significant than TDR-A.

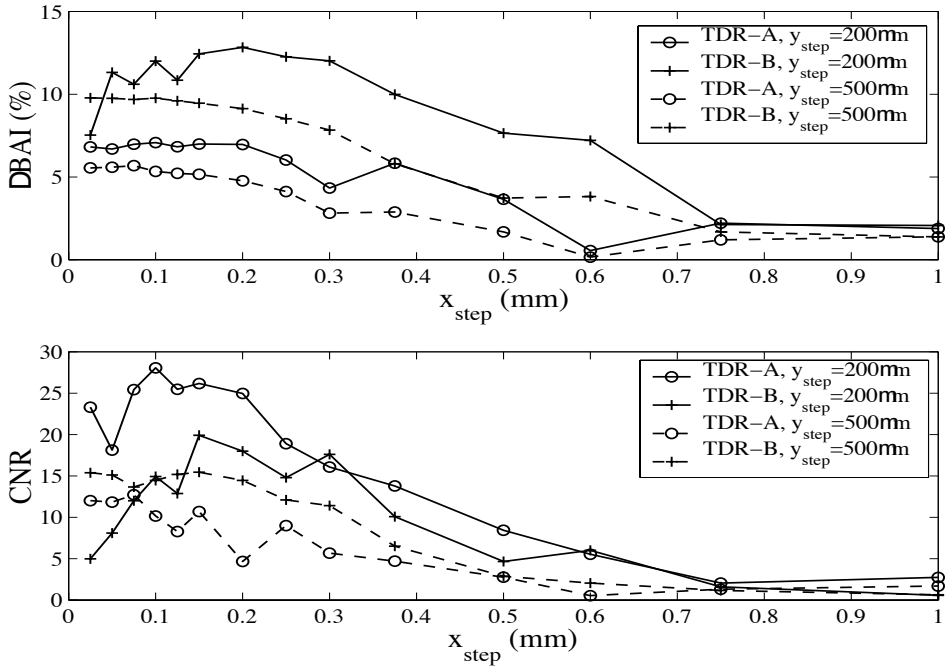

Figure 5.10 ΔBAI and CNR curves for varying spatial scanning step sizes using TDR-A and TDR-B for sample grid-c. Solid lines represent y_{step} = 200 μm cases. Dashed lines represent y_{step} = 500 μm cases.

Figure 5.10 compares the ΔBAI and CNR curves versus the spatial scanning step sizes using both transducers at y_{step} = 200, 500 μm for sample grid-c. The ΔBAI and CNR values degraded as scanning step size in each spatial dimension increased. For TDR-B, the ΔBAI and CNR curves dropped with different rates in the four different x_{step} intervals: no obvious degradation in [25 μm, 250 μm], moderate degradation in [250 μm, 500 μm], significant degradation in [500 μm, 700 μm] and asymptotically flat in [700 μm, 1000 μm]. The rate-dropping intervals of the ΔBAI and CNR curves

for TDR-A have been identified in Figure 5.6 as [25 μm, 200 μm], [200 μm, 375 μm], [375 μm, 600 μm], and [600 μm, 1000 μm]. The first intervals of no obvious degradation represented the oversampled case and the upper bounds of the intervals revealed the beam width of both transducers (200 μm for TDR-A and 250 μm for TDR-B). The second intervals of moderate degradation fell in between each of the transducer's beam width and twice that size. The third and fourth intervals of significant degradation represented extremely undersampled cases. There existed a turning point between $x_{step} = 300$ μm and 375 μm in the ΔBAI curves of TDR-A and a turning point between $x_{step} = 500$ μm and 600 μm in the ΔBAI curves of TDR-B after which the degradation rates of the ΔBAI values achieved their maximum. The ΔBAI curves of TDR-B changed more gradually than those of TDR-A as the x_{step} increased. The CNR value difference between $y_{step} = 200$ μm and 500 μm of TDR-A was much greater than that of TDR-B.

5.4 Discussion

In general, for those point-reflector array samples evaluated herein, the CNR and the ΔBAI values degraded gradually as scanning step size in each spatial dimension increased for each transducer. Significant image quality degradation occurred after either the x_{step} or the y_{step} exceeded twice the -6-dB pulse-echo focal beam lateral diameter of each transducer. For simple detection purposes, however, the x_{step} and the y_{step} could be fairly large.

On the other hand, the BAI-mode images obtained by TDR-A (Figures 5.8, top and 5.9, left) showed better defect structure details than those obtained by TDR-B (Figures 5.8, bottom and 5.9, right) because TDR-A has a smaller beam width than TDR-B. With a larger beam width, the heavily oversampled case might not be the best choice to obtain the best possible images. For example, TDR-B has a 247-μm beam width. The best image quality in Figure 5.8, bottom occurred when $y_{step} = 300$ μm > 247 μm, instead of in the oversampled case ($y_{step} = 200$ μm). This suggests that reducing the inspection speed of the production line below some critical speed will not necessarily improve the defect-detection fidelity. Also in Figure 5.10, the CNR values dropped as oversampling became heavier in either the x or y direction (TDR-A and TDR-B, $y_{step} = 200$ μm). The heavily oversampled case works as an aggressive smoothing filter to the images and sacrifices the image contrast. As to

the undersampled situation with the same step size, TDR-B yields better detection of the array pattern than TDR-A (Figure 5.9). What really matters is the ratio of the beam width to the spatial sampling step size. A small ratio offers better defect details but a large ratio gives consistent sample pattern detection.

At each sampled location and at each time instance, the focused ultrasonic transducer spatially averages the received RF echo over its spherical aperture. The envelope-integral operation (backscattered amplitude integral) sums the RF echo signal envelope temporally. The BAI-value is a quantity that describes the average characteristic of a RF echo waveform containing the sample structure information. These BAI-values are then distributed to each image pixel by inverse-distance interpolation. Although a smooth data interpolation method, the inverse-distance interpolation introduces interpolation error, especially when the given spatially sampled data points are not distributed densely enough. The more aggressive the transducer undersampling is, the coarser the sampled data points are and the more independent those BAI-values are. The structure variation of the sample could not be reconstructed with high fidelity when the spatial sampling density fell below a threshold, which was about twice that of the beam width in this study ($x_{step} > 375$ μm for TDR-A and $x_{step} > 500$ μm for TDR-B). We hypothesize that, geometrically, a virtual -6-dB pulse-echo focal beam spot can partially or fully fit into the space between the two sampled spots because of the relative motion between transducer and sample (Figure 5.11). Imagine each beam spot as a half-power threshold probe, as the transducer proceeds from the left real probe to the right real probe, each real probe detects a portion of the virtual spot area, more or less. With this hypothesis, the overlapped portion between the real probes and the virtual spot works as a virtual probe that could collect information about the virtual spot area. The ideal situation is that the virtual spot area should not exceed the real spot area at the best because the half-power energy concentration at the transducer's focal plane is confined in the -6-dB spot size. Neither of the two real probes illuminates out of the virtual spot area when the di stance is greater than twice that of the beam width (Figure 5.11). This explains why the image quality dropped significantly after the scanning step size exceeds twice the beam width. The relative motion between the transducer and the sample effectively increased the beam width with the virtual probe hypothesis. Although the scanning speed is improved, increasing scanning step sizes in both

spatial dimensions sacrifices the image quality. The transducer beam width should be a major factor in determining the optimal transducer spatial scanning step sizes.

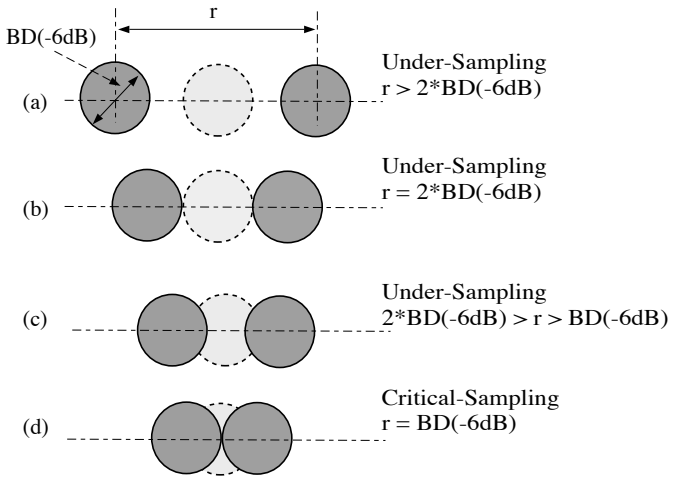

Figure 5.11 Distance between -6-dB pulse-echo focal beam spots in different sampling situations. BD(-6dB) is the -6-dB pulse-echo focal beam lateral diameter of the transducer. The dark circles represent actual focal beam spots. The light dashed circles are the virtual focal beam spots.

Based on the factors of the beam width and the uneven sampling density of the zigzag raster scanning pattern, we hypothesize that the optimal spatial sampling of the zigzag raster scanning pattern occurs when both the x_{step} and the y_{step} are greater than the beam width but less than twice of this lateral diameter. For TDR-A, the critical-sampled case is (x_{step} = 200 μm, y_{step} = 200 μm) where the BAI-mode image preserves the true details of the sample structure; (x_{step} = 375 μm, y_{step} = 300 μm) for rough and quick imaging; (x_{step} = 1000 μm, y_{step} = 400 μm) for simple and rapid detection purposes. For TDR-B, they are (x_{step} = 250 μm, y_{step} = 300 μm), (x_{step} = 450 μm, y_{step} = 400 μm), and (x_{step} = 1000 μm, y_{step} = 500 μm), respectively.

Suppose that the two assumptions in Section 5.2 about the scanning system were satisfied, using (5.1), Table 5.2 gives the estimated scanning speed using the BAI-mode imaging technique with the proposed 2D real-time zigzag raster scanning pattern. The echo pulse duration is about 0.2 μs for a 220-μm-thick package sample. The pulse-echo round trip times are 16.8 μs and 23.0 μs for TDR-A and TDR-B, respectively (5.1). Consider the minimal spatial sampling time intervals required for both transducers, the pulse repetition frequency could be chosen as 56 kHz for TDR-A and 42 kHz for TDR-B, corresponding with 17.9 μs and 23.8 μs spatial sampling

Table 5.2 Estimated scanning speed for the three typical inspection cases

case	TDR-A	TDR-B
x_{total} = 5 mm	PRF = 56 kHz	PRF = 42kHz
	(x_{step}, y_{step}) (μm), [v_x, v_y] (m/s)	
detailed imaging	(200, 200) [11.2, 0.23]	(250, 300) [10.5, 0.32]
rough and quick imaging	(375, 300) [21.0, 0.63]	(450, 400) [18.9, 0.76]
simple and rapid detection	(1000, 400) [56.0, 2.24]	(1000, 500) [42.0, 2.1]

time intervals, respectively. The x_{total} is 5 mm, which is a typical width of plastic sealing region. For instance, if x_{step} = 250 μm and y_{step} = 300 μm, a 5-mm distance in the x direction would require spatially sampled points (20 pulses), which would take t_x = (number of pulses)/PRF = 20/(42 kHz) = 0.476 ms for TDR-B to travel across the 5-mm distance one way. So the transducer scanning velocity x component $v_x = x_{total}/t_x$ = 10.5 m/s. Then, using (5.1), v_y is 0.32 m/s. They are approximately the upper speed limits for TDR-B when x_{step} = 250 μm and y_{step} = 300 μm. The scanning speed is a function of (1) the scanning width in the x direction; (2) spatial sampling step sizes in both directions, which are related to focal beam width; and (3) the pulse repetition frequency, which is limited by pulse-echo round trip time and echo pulse duration. The inspection could be further speeded up with multiple sensors working in parallel configuration.

Since the five point-reflector array samples were scanned separately, the measurement conditions (e.g., misalignment of focusing, mechanical movement, temperature, noise) differ from each other. The ΔBAI curves for different samples were more vulnerable to the change of measurement conditions than the CNR curve. The CNR curves showed a more consistent decreasing pattern than the ΔBAI curves did when the grid size was reduced (Figure 5.7). The variable measurement conditions could contribute different offset conditions to the BAI-values for each individual sample. The ΔBAI-value (4.3) is normalized to the maximum BAI-value in the image, which contains such offset and does not account for the overall dynamic range of pixel

values. The ΔBAI-value could be a good performance index for evaluating an individual sample under different x_{step} and y_{step}, e.g., the ΔBAI curves was capable of characterizing the degradation rate change of ΔBAI values for each individual sample (Figure 5.6) but the CNR curves failed to identify this characteristic. On the other hand, CNR (4.4) considers the overall dynamic range of pixel values. Furthermore, CNR is a ratio-based threshold index for evaluating image pixel values. It might suggest that CNR is a more appropriate performance index for quality assessment of the BAI-mode image, especially for the image comparison among different samples.

5.5 Conclusions

The ultrasonic pulse-echo BAI-mode imaging technique with a real-time zigzag raster transducer scanning pattern was investigated experimentally. The static stop-and-go transducer scanning pattern is impractical for real-time product line package inspection because package motion is continuous. The zigzag raster pattern simulates the real-world package inspection scenario where the sample is in linear motion with constant speed in the y direction while the ultrasonic transducer scans the sample back and forth in the x direction. The zigzag raster pattern reduces the risk of missing small defects horizontally oriented in the x direction in the pulse-echo detection, especially when the sample motion speed is very high. This real-time zigzag raster scanning pattern offers a more efficient spatial sampling scheme on the entire sample surface and thus has the potential to examine a larger area with higher inspection speed in real-time than the stop-and-go scanning pattern could do.

By evaluating the image quality indices (ΔBAI and CNR) degradation rate, it was found that with the proposed real-time zigzag raster transducer scanning pattern, the BAI-mode image quality depended on the relative ratio between the scanning step sizes in each spatial dimension and the beam width. The optimal scanning occurs when the x_{step} and the y_{step} are both greater than, but less than twice, the beam width. The scanning speeds related to different inspection purposes were also estimated. We conclude through the quantitative evaluation that the transducer scanning speed could be prompted with the real-time zigzag scanning pattern. The optimal spatial sampling step sizes help reduce inspection time compared to a value calculated using the sparrow criterion [32]. For a focused ultrasonic transducer, a larger -6-dB pulse-echo focal beam spot size allows for an increased inspection speed

and a better detection of the defect pattern, but does not provide for as much image detail. This is because the transducer's beam spot size not only becomes larger but also can be attributed to the relative motion between the transducer and the sample, which effectively increases the beam width.

CHAPTER 6

SIMULATION OF THE PULSE-ECHO DETECTION TECHNIQUE

From a review on numerical wave propagation simulation techniques, this chapter presents the rationale for choosing an FDTD method with perfectly matched layer absorbing boundary condition to simulate the pulse-echo channel defect detection process. The implementation and validation of the numerical simulation code are described in this chapter.

6.1 Toward Insightful Understanding: Numerical Simulation

As mentioned in Section 3.2, although the pulse-echo BAI-mode imaging technique has been proven to be reliable for channel defect detection, the underlying detection mechanism is poorly understood. We want to know why the pulse-echo BAI-mode imaging technique can detect such a channel defect small compared to a wavelength. We hypothesize that the defect sample microstructure, such as the bonding layer between the two plastic films and the impedance perturbation of the defect to the plastic film layers during the hermetical-sealing process, might be part of the answer.

The pulse-echo defect detection process is indeed a wave-structure interaction problem. This problem cannot be solved analytically because the microstructure involved has no regular geometric shape and the interaction between the ultrasonic wave and the microstructure cannot be modeled analytically. The relationship between the hermetical-sealing conditions (such as temperature, sealing time, vacuum condition) and the resulting sample microstructure remains unknown so far. Neither can this problem be explored experimentally because it is impossible to control the defect sample microstructure as we wish during the hermetical-sealing process.

Scattering by rigid or elastic objects of simple shape, such as a sphere and a

cylinder, has been well studied for years [79]-[81]. However, for complex scatterers such as the channel defect embedded in the plastic material, numerical solution has to be used. The wave-structure interaction problem will be investigated using a numerical approach to evaluate the underlying parameters that could influence the pulse-echo detection behavior.

To simulate the pulse-echo detection process, the acoustic wave equation must be solved numerically. There is a huge body of computer-based numerical methods available to solve wave propagation equations in electromagnetics and acoustics. Without making *a priori* assumptions about which field interactions are most significant, numerical techniques analyze the entire geometry provided as input. They calculate the solution to a problem based on a full-wave analysis.

Numerical methods for wave propagation can be divided into two major categories: frequency-domain methods such as finite element method (FEM) [82] and boundary element method (BEM) [83], and time-domain methods such as finite-difference time-domain (FDTD) method [84], [85] and finite-volume time-domain (FVTD) methods [86]. By assuming time-harmonic wave nature, frequency-domain methods compute wave field distribution at certain frequencies. They generally convert the wave equation to a discrete matrix equation by (1) dividing the computational domain into small elements; (2) applying basis functions to each element and expanding wave field variables into a set of unknown coefficients associated with the basis functions; and (3) assembling the contribution from the basis functions at each node to the discrete matrix. After enforcing boundary conditions and applying incident field variables, the overall discrete matrix equation represents the original wave-structure interaction problem mathematically, which is ready to be solved in computer. Although it is possible to obtain a time-domain solution by doing inverse Fourier transfer from the frequency-domain solution, time-domain methods provide a more efficient and direct way than frequency-domain methods to solve for time-domain wave propagation problems. Time-domain methods are especially appropriate to simulate transient wave propagation such as ultrasonic pulse-echo detection behavior.

The most original and popular FDTD technique is the uniform grid FDTD algorithm proposed by Yee in 1966 [84]. In this algorithm, both time and space are discretized, and second-order central-difference approximations of derivatives are

used to obtain a set of simple equations which yield future field values based on the past and present field quantities. The original Yee algorithm achieves great success in solving for problems with enclosed structure such as internal field in a waveguide. However, the original Yee algorithm is unable to solve an open space problem for any significant period of time because the computational domain truncation brings mathematical reflections when the outgoing wave is incident on the domain boundary where no specific boundary condition is determined. Therefore, an absorbing boundary condition (ABC) is often used to truncate the computational domain to simulate a free space condition. The quest for an ABC that produces negligible reflections has been, and continues to be, an active area of FDTD research. Numerous ABCs have been proposed. The material-based PML ABC appears to yield a major improvement in the reduction of boundary reflection compared to any differential-based and material-based ABCs proposed previously [87], [88].

The FDTD method provides a simple and efficient means of solving wave equations for a wide variety of problems. The main advantages of FDTD techniques are simplicity and the ability to handle complex geometries (in principle). The derivation of computer-implementable FDTD formulation from wave equation is based on traditional mathematical methods of approximating derivatives by finite differences. The equations are numerically exact; i.e., no physical assumptions are made regarding energy propagation and interaction with scattering materials. The implementation is thus very straightforward. The simplicity of the Yee algorithm makes it suitable for parallel computation for the large-scale or fine-computational grid problem. However, the Yee algorithm is inherently dispersive and anisotropic [89]. For large problems, forty wavelengths or larger, errors from dispersion and anisotropy are significant (a phase difference greater than $\pi/8$ is considered significant) unless the spatial discretization is very small. This can lead to prohibitive memory requirements and high computational cost [87], [90].

Both the FDTD and the PML are well developed techniques. As a time-domain numerical simulation tool, FDTD is good at simulating the transient wave propagation and scattering phenomena such as the ultrasonic pulse-echo defect detection problem [91]-[94]. The PML absorbs outgoing waves at the truncated computational domain so that a simulated free space can be realized [88]. With the FDTD and the PML, we have developed a numerical simulation tool to

computationally implement the ultrasonic pulse-echo defect detection process.

6.2 Methodology and Implementation

Simulation of the ultrasonic pulse-echo defect detection behavior has been implemented by solving for the linear acoustic wave equation in a homogeneous, lossy fluid medium (6.1) using FDTD with PML:

$$\begin{aligned} \nabla p(\mathbf{r},t) &= -\rho\frac{\partial}{\partial t}\mathbf{u}(\mathbf{r},t) - \alpha^*\mathbf{u}(\mathbf{r},t) \\ \nabla\cdot\mathbf{u}(\mathbf{r},t) &= -\kappa\frac{\partial}{\partial t}p(\mathbf{r},t) - \alpha p(\mathbf{r},t) \end{aligned} \tag{6.1}$$

where p is the acoustic pressure field, $\mathbf{u}$ is the vector particle velocity field, $\mathbf{r}$ represents the vector field point, t represents time, ρ is the mass density of the medium, κ is the compressibility of the medium, α is the attenuation coefficient associated with compressibility, and α^* is the attenuation coefficient associated with mass density. The absorption in PML is achieved by setting $\alpha^* = \alpha\rho/\kappa$ in the PML region and $\alpha^* = 0$ in the acoustic medium [95] (Appendix D). Further research on PML for the FDTD solution to wave-structure interaction problems can be found in [96].

A measured data set from a 38-μm water-filled channel defect is available by using a spherical focusing transducer (TDR-A in Chapter 5) to collect RF echo waveforms. The numerical simulation uses the transducer parameters in order to compare the simulated echo waveforms with the measured echo waveforms. The diameter and the characterized focal length of the spherical focusing transducer are 6.35 mm and 12.44 mm, respectively, which are 74λ and 145λ in degassed water ($\mathcal{T} \approx 20$ ^{o}C, $c \approx 1485$ m/s, $f_0 = 17.3$ MHz, $\lambda \approx 86$ μm). It is prohibitive to include the transducer and the entire transducer-to-sample wave propagation path in the FDTD computational domain due to impractical computational cost and large dispersion errors (see Section 6.1). There are two approaches to deal with this drawback: using higher-order accuracy FDTD methods or reducing the computational domain to a reasonable size. However, the higher-order FDTD methods are not as accurate as the Yee algorithm for the simulation at material boundaries due to the larger spatial stencil used in higher-order methods. Because the material boundaries are the important features in the pulse-echo defect detection simulation, we choose the latter alternative to deal with the long distance propagation problem — reducing the computational domain size to a reasonable size.

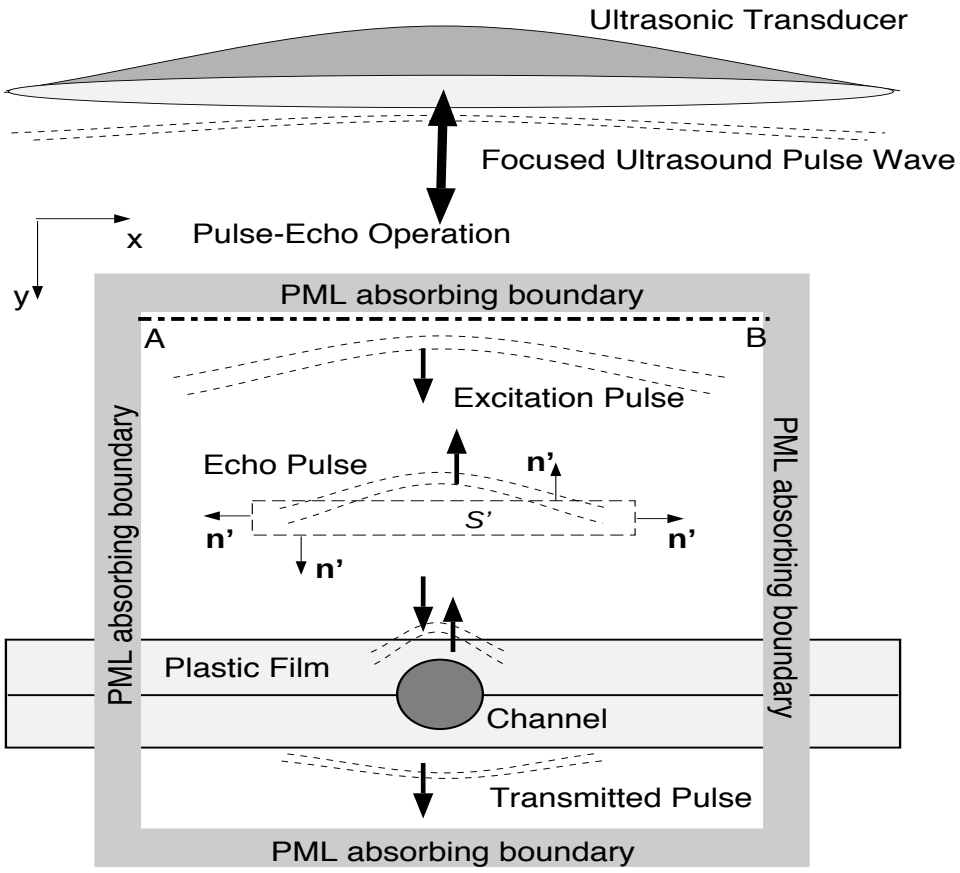

Figure 6.1 Pulse-echo simulation with FDTD and PML.

To reduce domain size, the 2D simulation uses FIELD-II[1] [97] to calculate the transmitted ultrasound pulse pressure field along the line AB in Figure 6.1. The ultrasound field along line AB (Figure 6.2) is assumed to be equivalent to the pulsed ultrasound wave that reaches line AB in FDTD simulation. The transmitted pulse in simulation is described as [98]

$$p_{inc}(t) = \frac{t}{T}\exp(-4\Delta f^2 t^2)\sin(2\pi f_0 t) \tag{6.2}$$

[1]FIELD-II is a set of programs for simulating ultrasound transducer fields and ultrasound imaging using linear acoustics. The programs use the Tupholme-Stepanishen method for calculating pulsed ultrasound fields. The programs calculate the emitted and pulse-echo fields for both the pulsed and continuous wave case for a large number of different transducers.

where $f_0 = 17.3$ MHz is the transducer center frequency, $T = 2/f_0$ is the pulse duration of the transmitted pulse, and $\Delta f = 7.35$ MHz is the -3-dB transducer bandwidth.

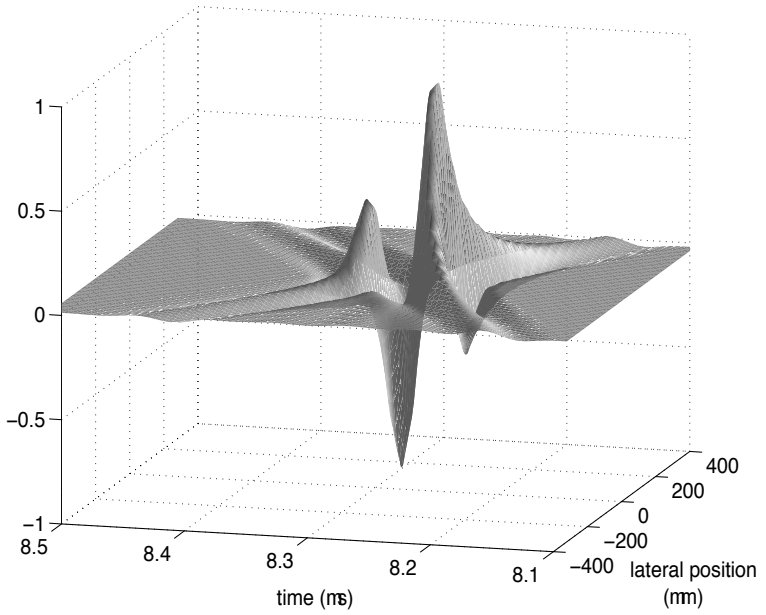

Figure 6.2 Emitted lateral pressure field along line AB.

The echo pulse pressure received by the transducer surface is extrapolated by evaluating the transient Helmholtz integral along the enclosed contour S' in Figure 6.1 [99], [100].

$$p(\mathbf{r},t) = \frac{-1}{4\pi}\oint_{s'}\left[\frac{\partial r}{\partial \mathbf{n}'}\left(\frac{\tilde{p}(t-\frac{r}{c})}{r^2}+\frac{1}{cr}\frac{\partial \tilde{p}(t-\frac{r}{c})}{\partial t}\right)+\frac{1}{r}\frac{\partial \tilde{p}(t-\frac{r}{c})}{\partial \mathbf{n}'}\right]dS' \qquad (6.3)$$

where $\mathbf{n}'$ is the outward surface norm on S', and c is the speed of sound in the medium. The enclosed surface S' consists of evenly divided radiating elements whose positions are $(x',\ y')$ (Figure 6.3). The transducer surface is partitioned with equally sized receiving elements whose positions are $(x,\ y)$. The vector between each radiating-receiving pair is $\mathbf{r} = \hat{i}(x-x') + \hat{j}(y-y')$. The pressure $\tilde{p}(t-\frac{r}{c})$ on S' is computed by the FDTD simulation at each time step.

The computational domain could be significantly reduced from 145λ long by 47λ wide to 10λ by 10λ with FIELD-II and the transient Helmholtz integral (6.3). The simulation using FDTD and PML has been implemented in MATLAB for 2D scenario (Appendix D) in Cartesian coordinates. The computational domain is a rectangle.

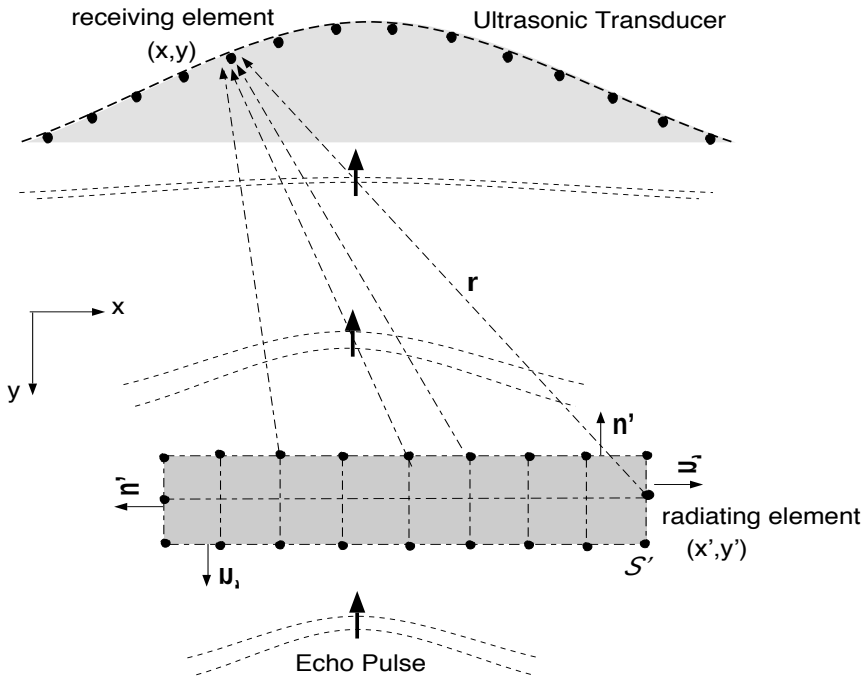

Figure 6.3 Evaluation of the transient Helmholtz integral.

A spatial-temporal update scheme similar as the well-known Yee algorithm [84] is adopted in the FDTD evolution. To ensure stability, the grid size $\triangle = \lambda_{min}/20$ and the time evolution step $h = \triangle/2c_{max}$, where λ_{min} is the smallest wavelength and c_{max} is the greatest speed of sound of all media in the computational domain. The PML has a 10-grid thickness.

Because the defect we are dealing with is a long cylindrical channel enclosure in bonded two-sheet plastic film, the channel length (typically 8 mm long) along its center axis (the axis perpendicular to the x-y plane in Figure 6.1) can be treated as infinite in comparison with package sample cross section (about 800 μm by 220 μm) in the x-y plane. The 2D simulation will be adequate to simulate the pulse-echo detection process. Besides, the 3D simulation requires much larger computer memory and longer computation time than the 2D simulation. We will concentrate on the 2D simulation for the simplicity and computation time constraint.

6.3 Code Validation

The simulation implementation has been validated by three test cases described below. The excitation signal for all these test cases was taken from (6.2) (Figure 6.2). In all the test cases, the grid size $\triangle = \lambda_{min}/20$ and the time evolution step $h = \triangle/2c_{max}$, where λ_{min} is the smallest wavelength and c_{max} is the greatest speed of sound of all media in the computational domain. The PML has a 10-grid thickness. In all the following figures, the indices N_{i1}, N_{i2}, N_{j1}, N_{j2} are the grid x- and y- labels at the interfaces between the acoustic and the PML regions. The indices N_{ic} and N_{jc} are the grid x- and y- labels at the computational domain center.

Test Case 1: Wave propagation in homogeneous medium from a point source and a line source

As the first validation check, the purpose of this test was to verify the FDTD algorithm implementation in MATLAB and the PML performance. A point source was created by feeding the excitation pulse (6.2) to a point (src) at the computational domain corner (Figure 6.4(a)). The acoustic domain is homogeneous. Three waveforms were observed in the computational domain at locations ($obv1$, $obv2$ and $obv3$ in Figure 6.4(a)). The normalized correlation coefficient between the excitation signal and the observed waveform at $obv3$ was 99.24%. The normalized correlation coefficient was used as a quantitative similarity index to evaluate two waveforms [101].

As the point source emitted a cylindrical wavefront in a lossless homogeneous medium, the power conservation law held. At $t = 0$, the total power of the system was $I(t = 0) = p_0^2 \times 4\triangle$, where p_0 was the excitation signal amplitude, and $\triangle$ was the grid size (the energy was confined within one grid square which had a perimeter of $4\triangle$). At any later time $t > 0$, the power contained in the equal-phase cylindrical wavefront could be calculated as $I(t) = p^2(i,j) \times 2\pi r(i,j)$, where $p(i,j)$ was the waveform amplitude at the field point (i,j) and $r(i,j)$ was the distance from the field point to source point (src). The waveform amplitude at any field point (i,j) could be calculated as $p(i,j) = p_0\sqrt{2\triangle/\pi r(i,j)}$. The dashed line in Figure 6.4(d) was the calculated amplitude changes along the computational domain diagonal line. The simulation amplitude changes (solid line in Figure 6.4(d)) matched with the calculated amplitude changes very well. Figure 6.4(e) showed the normalized correlation coefficient map in the entire acoustic region between the excitation signal

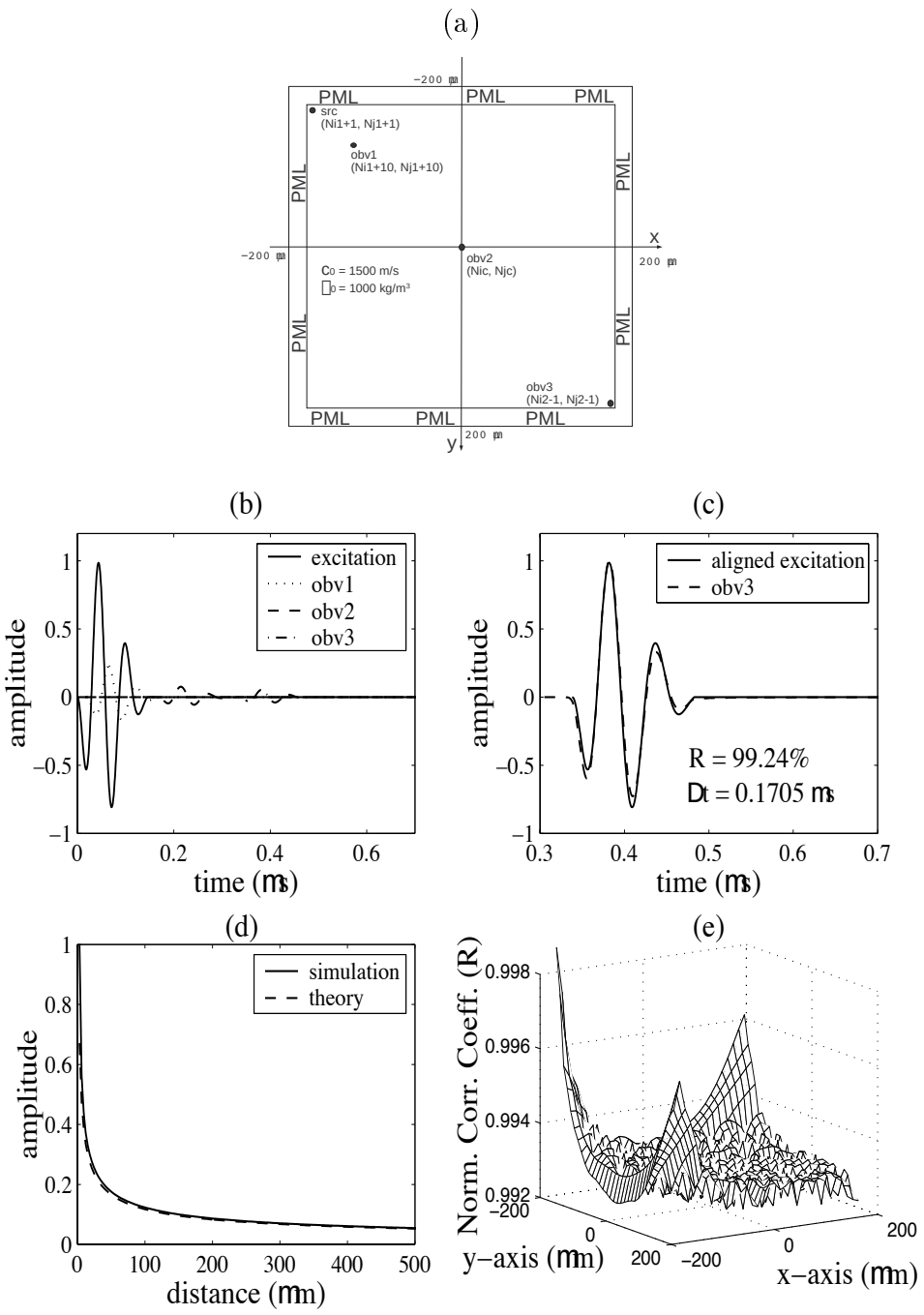

Figure 6.4 **Test Case 1**: wave propagation in homogeneous medium from a point source. (a) Configuration, (b) excitation signal and three observed waveforms, (c) comparison between the excitation signal and the waveform at $obv3$, (d) comparison between the simulated and the theoretical pulse amplitudes along the line connecting the four points in the top figure, and (e) map of the normalized correlation coefficients between the excitation signal and the observed waveforms in the computational domain.

and the observed waveforms, with minimum value of 99.24% and maximum value of 99.83%.

The validation test for wave propagation in a homogeneous medium from a line source was shown in Figure 6.5. The normalized correlation coefficients between the excitation signal and the two observed signals were 99.98% and 99.92%, respectively. The wave speed (estimated from the slope of the distance-time delay curve in Figure 6.5(e)) was 1500 m/s, exactly the same as the assigned medium property.

Test Case 2: Wave reflection and transmission at normal incidence and wave propagation in attenuating medium.

This test case verified the proper behavior of pulse-echo operation and the implementation of the attenuation in FDTD-PML code. Figure 6.6 shows the wave reflection and transmission when the acoustic region had two media and a planar interface between them (media 0 and 1). Because the acoustic impedance of medium 1 was less than that of medium 0, the reflected wave had a phase change of π. Therefore, the normalized correlation coefficient between the excitation signal and the reflected waveform was -99.97% (Figure 6.6(d)). The estimated wave speeds again accurately verified the simulation validity. The amplitude ratio between the reflected and incident waves was -0.3086. The amplitude ratio between the transmitted (dashed-line in Figure 6.6(b)) and incident waves is 0.6902. They are comparable with the calculated reflection and transmission coefficients according to (1.8): Z_1=0.8 M$rayl$, Z_0=1.5 M$rayl$, $R = (Z_1 - Z_0)/(Z_1 + Z_0) = -0.3043$, $T = 2Z_1/(Z1 + Z_0) = 0.6957$.

The simulation results for an attenuating medium were shown in Figure 6.7. The attenuation coefficient in medium 1 was set to be 20 dB/mm, assuming no frequency dependency. The attenuation coefficient estimated from the simulation results was 19.98 dB/mm (Figure 6.7(e)), which agreed with the assigned value very well.

Test Case 3: Simulated pulse-echo wire technique for transducer characterization

This test case verified the incorporation of FIELD-II functions and the transient Helmholtz integral (6.3) into the FDTD-PML code. A simulated transducer characterization was done by using the pulse-echo wire field measurement technique [19]. In the simulation, a 38-μm-diameter metal wire was placed in the computational domain to generate echo pulses. The simulated pulse intensity integral (PII) image (Figure 6.8) was generated by acquiring echo pressure pulses from each wire location

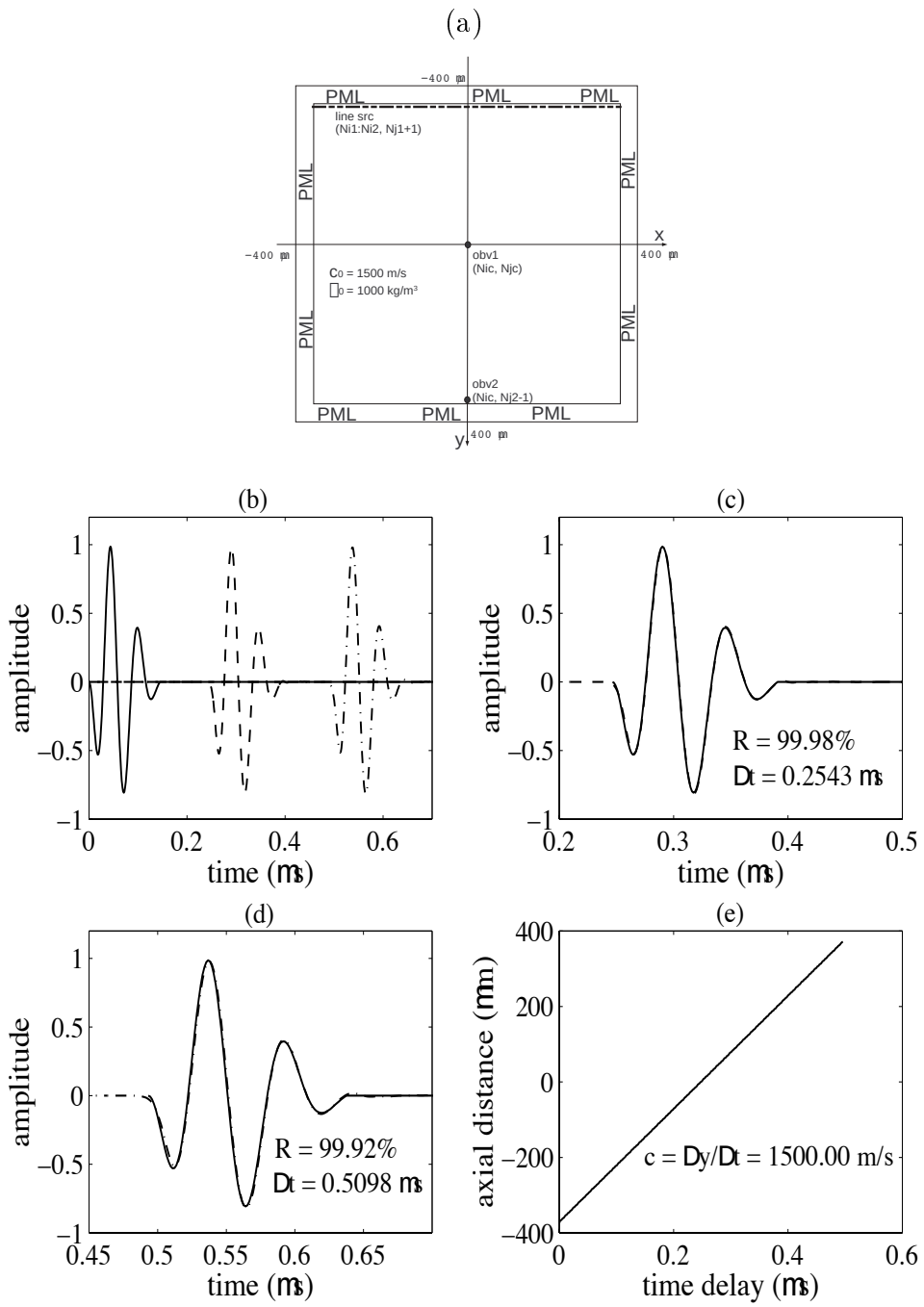

Figure 6.5 **Test Case 1**: wave propagation in homogeneous medium from a line source. (a) Configuration, (b) excitation signal (solid line) and two observed waveforms, (c) comparison between the excitation signal and the waveform at $obv1$ (dashed line), (d) comparison between the excitation signal and the waveform at $obv2$ (dash-dotted line), and (e) the distance in the y-axis versus wave propagation time delay.

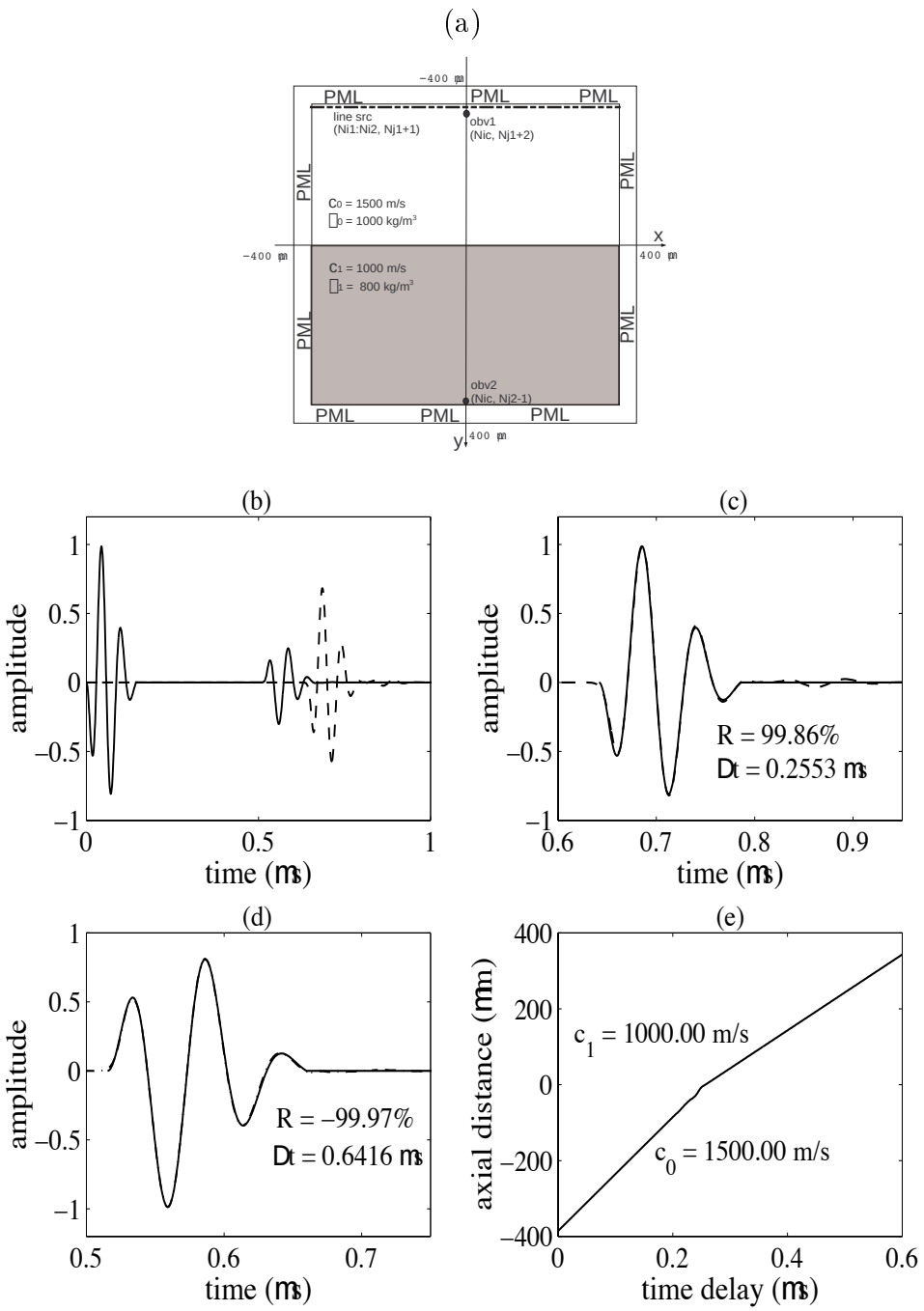

Figure 6.6 **Test case 2**: wave reflection and transmission. (a) Configuration, (b) two observed waveforms (*obv*1: solid line, *obv*2: dashed line), (c) comparison between the excitation signal (solid line) and the waveform at *obv*2 (transmitted wave, dashed line), (d) comparison between the flipped excitation signal (solid line) and the waveform at *obv*1 (reflected wave, dash-dotted line), and (e) the distance in the y-axis versus wave propagation time delay.

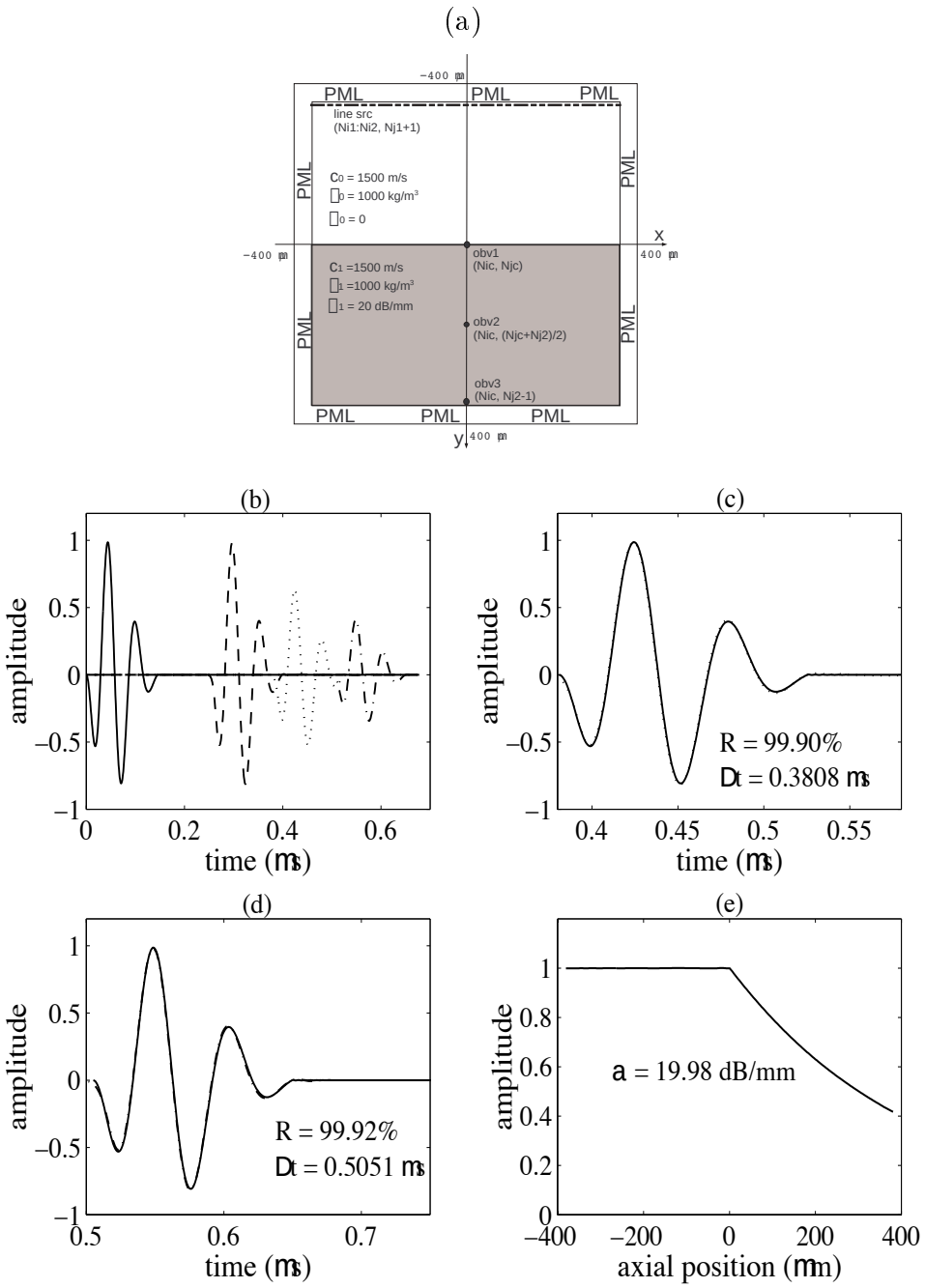

Figure 6.7 **Test case 2**: wave propagation in attenuating medium. (a) Configuration, (b) excitation signal (solid line) and three observed waveforms, (c) comparison between the excitation signal and the waveform at $obv2$ (dotted line), (d) comparison between the excitation signal and the waveform at $obv3$ (dash-dotted line), and (e) the amplitude change versus y-axis position.

in the computational domain. The transducer and its waveform parameters were extracted by using the MATLAB program "complete5.m"[2] to process the simulated echo waveform data. Table 6.1 compares the simulation results with experimental measurement and calculated results from theory [19]. The simulation agrees with experiment very well.

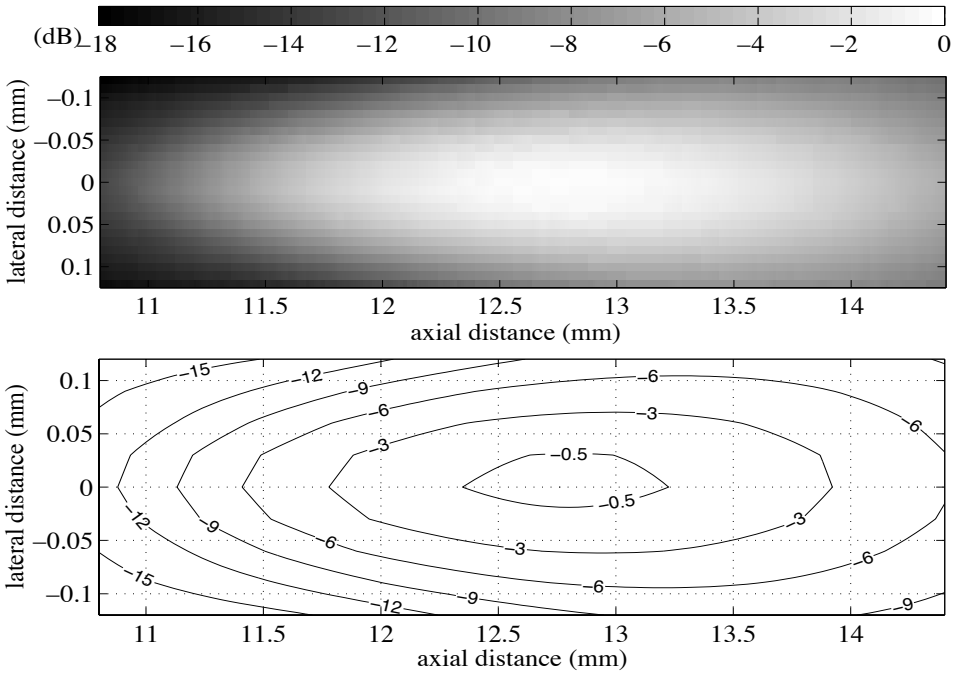

Figure 6.8 **Test Case 3**: simulation PII image and its dB scale contour plot of the pulse-echo wire technique for transducer characterization.

The three test cases provide a comprehensive validation of the 2D FDTD-PML code, which gives confidence in using the code as a reliable numerical tool to further conduct pulse-echo subwavelength defect detection mechanism study.

[2]A MATLAB script that was developed in BRL for processing pulse-echo wire measurement data. The simulated echoes were written to files with the designated format and processed by this MATLAB script as if they were "*real*"experimental measurements.

Table 6.1 Transducer characteristics obtained from numerical simulation

	Parameters in FIELD-II	Parameters from simulation	Calculated from theory
D (mm)	6.35	6.35	6.35
$f^{\#}$	2	1.98	2
f_0 (MHz)	17.3	17.8	20.0
$\Delta f_{(-3\text{dB})}$ (MHz)	7.35	8.12	5.95
Fractional BW	43.5%	34.8%	27.4%
F_L (mm)	12.7	12.65	12.7
RTT (μs)	16.8	17.0 (c = 1485 m/s)	17.1 (c = 1485 m/s)
F_z (mm)	2.15	2.72	2.42
$BD_{(-6\text{dB})}$ (μm)	173	193	176

CHAPTER 7

PACKAGE SAMPLE MICROSTRUCTURE: EXPERIMENT AND CHARACTERIZATION

The numerical evaluation tool has been developed and validated in Chapter 6. To study the wave-structure interaction, it is necessary to build a generalized impedance model for the package sample microstructure. This chapter first presents the experimental observations and characterizations of package samples through acoustic image and optical microscopic image studies. The package sample microstructure showed interesting features contrary to what we previously thought. Further, attempts had been made to investigate the microstructure formation cause. These efforts are associated with our intention to propose a generalized impedance map model for the package sample microstructure.

7.1 Sublayers Inside Package Films

The package sample with channel defect was produced by using a heat sealer (Audionvac-VM151HG, Audion Electro, Weesp, Holland) to fuse a smooth, die-drawn tungsten wire in between two plastic trilaminate package films and removing the wire along its axial direction after the package sample had cooled (Appendix B). Each trilaminate package film has three sublayers: polypropylene layer (80 μm, c = 2660 m/s, ρ = 900 kg/m^3), polyvinylidene chloride (PVDC) layer (15 μm, c = 2380 m/s, ρ = 1600 - 1700 kg/m^3), oriented nylon layer (15 μm, c = 2600 m/s, ρ = 1140 kg/m^3). A water-filled channel defect was then created by immersing the fused plastic sample in degassed water, having sandwichlike layered structure (Figure 7.1).

The ultrasound beam encounters complex structures in its propagation path: the package sample front wall, interfaces between sublayers, an impedance change in the heat-fusing zone between the two plastic sheets, the channel, impedance deviation surrounding the channel that is caused by compacting plastic medium toward the tungsten wire during the heat-sealing process, and the package sample back wall

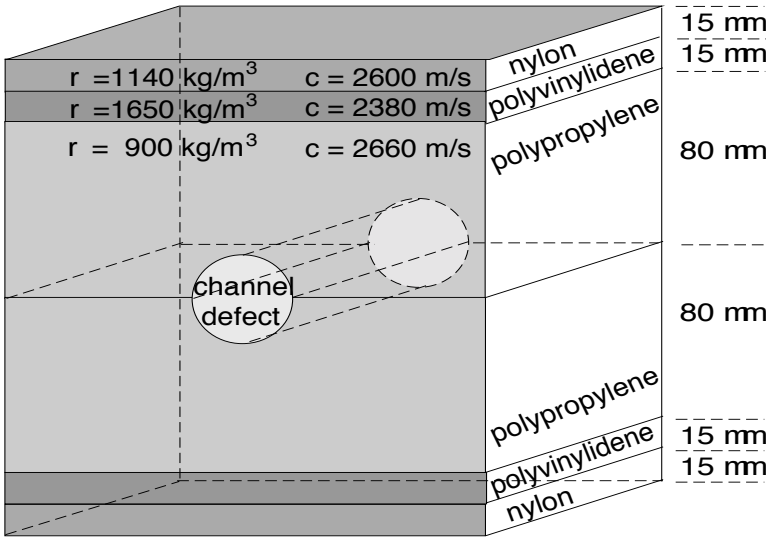

Figure 7.1 Cross section illustration of package sample with channel.

as well. The water-filled channel represents a small region of impedance mismatch. The backscattered echoes caused by the channel defect are weaker than the reflected echoes caused by the front and back walls of the plastic package. Furthermore, the echoes from the channel defect are sometimes buried in the echoes from the multiple reflections caused by the package sample. Thus, a theoretical modeling study has been undertaken to investigate the origin of the BAI-mode image contrast, and hopefully establish a generalized numerical model for the pulse-echo subwavelength defect detection system.

7.2 Sample Microstructure Measurement

An impedance profile model has to be established for the pulse-echo defect detection simulation. The impedance profile of interest is the package sample cross section distribution in the 2D simulation.

Optical microscopic images of the package sample cross section were obtained to observe the microstructure features. Several measured sample impedance profiles along the sample cross section thickness dimension were examined in order to have a quantitative measurement of the impedance (see Appendix C for experiment details). Acoustic images of the package sample cross section were constructed to understand the 2D cross section impedance map. The pixel values of an acoustic image are the

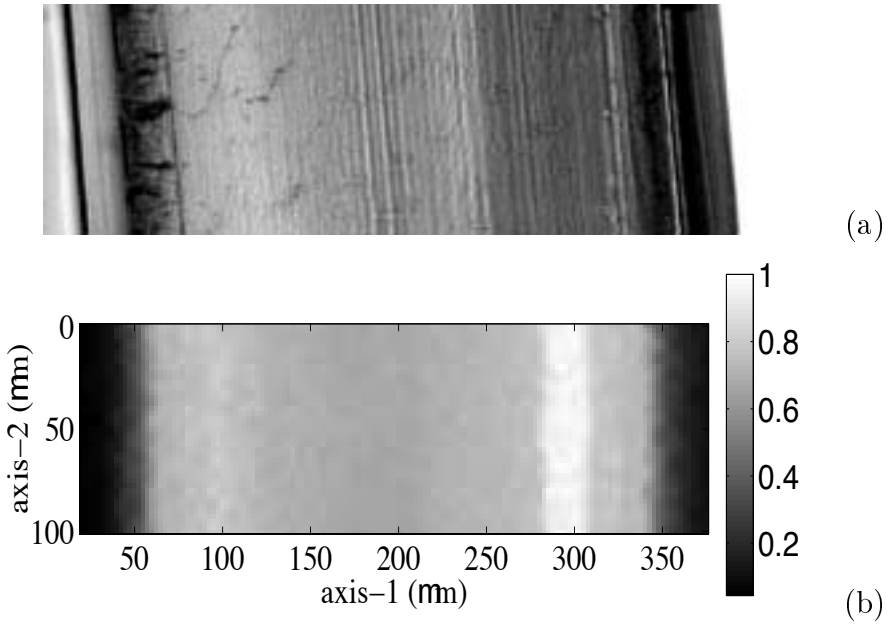

Figure 7.2 Optical microscopic image (a) and acoustic image (b) of a package sample, without channel defect.

relative echo amplitudes normalized to the maximum echo amplitude in the scanning region. In all these images and impedance measurements, the transducer was placed in the right side, which makes the sample right edge to be the "front wall," as described in Section 7.1.

The microstructure of the package sample without channel defect was investigated to establish a generalized impedance profile for the intact region. Optical microscopic and acoustic images of the package sample cross section were obtained (Figure 7.2). Both images showed clear sublayer features. They also demonstrated that the package sample had asymmetric acoustic properties. The vertical bright strip at 300 μm in axis-1 (Figure 7.2(b)) corresponded with the PVDC sublayer in one package film. This PVDC sublayer had the maximum impedance value in the acoustic image. The PVDC sublayer in the other package film should have a corresponding vertical bright strip at 100 μm in axis-1 if the impedance profile were symmetric as the nominal values predicted (see Section 7.1). However, no obvious vertical bright strip appeared in the acoustic image at 100 μm in axis-1.

Figure 7.3 showed two impedance profiles at two randomly chosen horizontal cuts in Figure 7.2(b). The maximum impedance occurred near the front wall and a dip

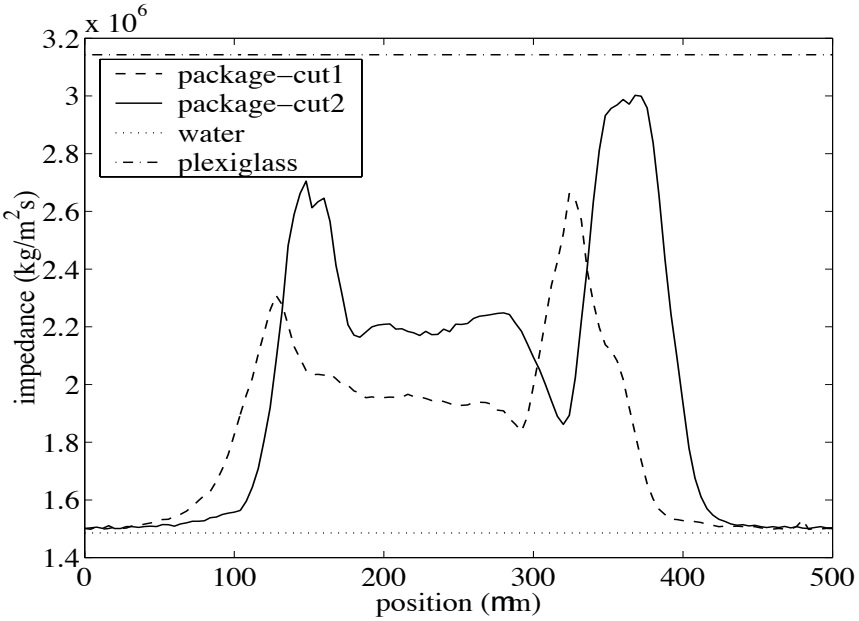

Figure 7.3 Two impedance profiles of a package sample, without defect.

appeared behind the maximum impedance sublayer. The impedance at the package sample back wall is less than that at the front wall.

Figure 7.4 showed another acoustic image of the package sample cross section. The acoustic image verified the asymmetric impedance profile observation (brighter pixel values in the right part than in the left part of the image). Moreover, the curved dark strips in the left part of the image indicated that there could be curved interfaces inside the package sample cross section, rather than purely planar sublayer interfaces.

According to Figures 7.2 - 7.4, although identical in nominal impedance properties before heat sealing, the two binding films showed an asymmetric impedance profile after sealing. The multiple reflections in the asymmetric sublayers behaved with more complexity than in the presumed symmetric sublayers.

The package samples with 75-μm-diameter (Figure 7.5) and 38-μm-diameter (Figure 7.6) water-filled channel defects were examined. The shape of the channel defects was not a perfect circle as the shape of the tungsten wire cross section. The same observation was also made in [49]. The channel defects appeared to be of elliptic shape and the channel defect contours were not smooth, demonstrating an impedance perturbation region surrounding the channel defect. The position of the

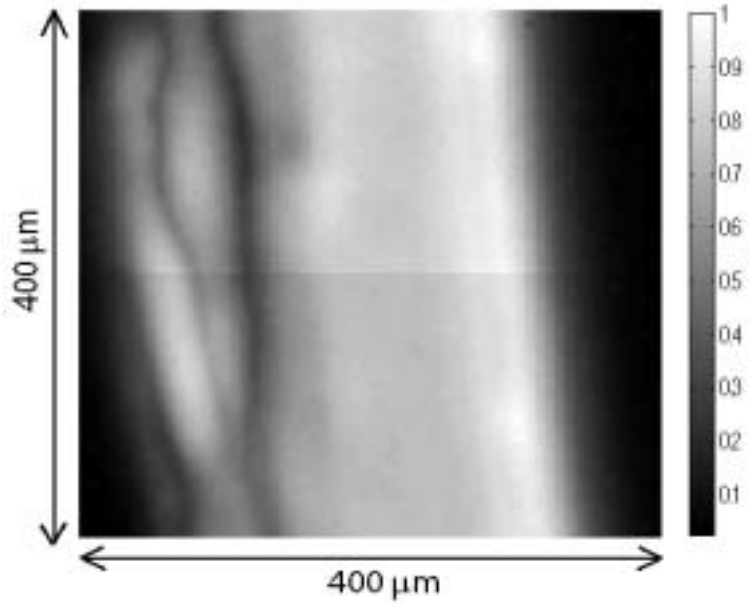

Figure 7.4 Acoustic image of a package sample sealing region, without channel defect.

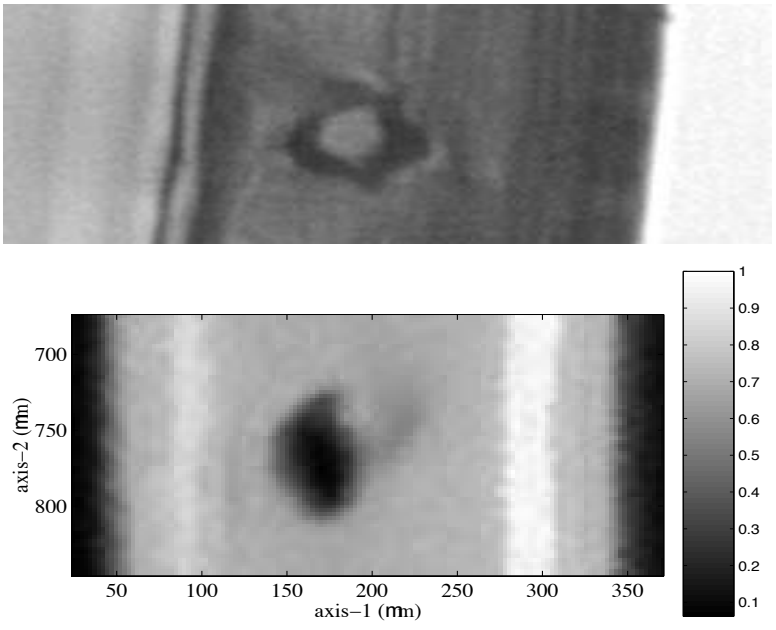

Figure 7.5 Optical microscopic image (a) and acoustic impedance image (b) of a package sample containing 75-μm-diameter water-filled channel.

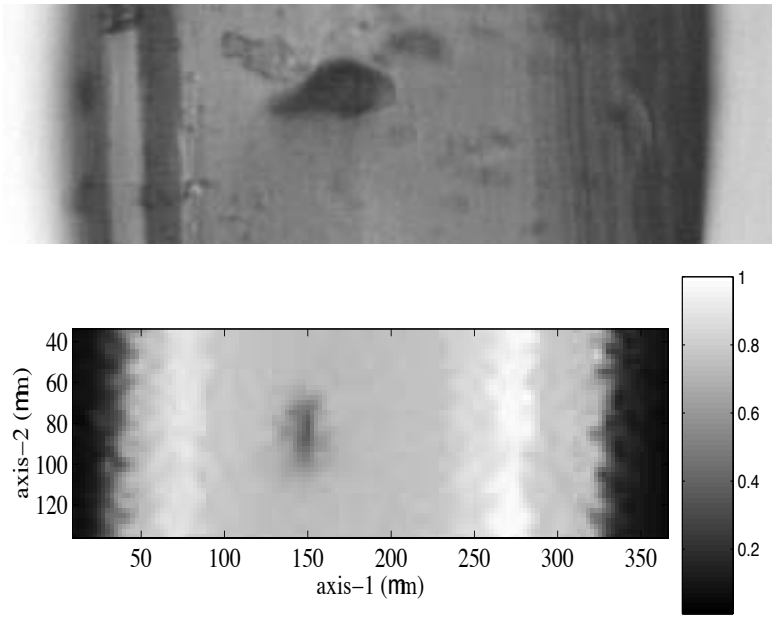

Figure 7.6 Optical microscopic image (a) and acoustic impedance image (b) of a package sample containing 38-μm-diameter water-filled channel.

channel defect was not exactly in the center point between package sample walls. Another feature is the material shrinkage and inward bending-over in the PVDC sublayer that is to the left at the channel defect and at the back wall in both Figures 7.5 and 7.6. But the bending-over is much more obvious in the 75-μm-diameter channel defect sample than in the 38-μm-diameter channel defect sample. This could be caused by the tungsten wire size and the huge thermal conductivity difference (Table 7.1) between the tungsten wire and the package sublayer materials when heat was applied on them.

7.3 Microstructure Formation Cause

The experimental measurement of the package sample cross section discovered many interesting microstructure features such as asymmetric impedance profile, elliptic channel defect shape and nonsmooth channel defect contour, position shift of channel defect and sublayer shrinkage and bending-over in defect region. The elliptic shape might be caused by the material compounding induced by the applied static pressure from both sides of the sample (axis-1) during the heat sealing process, while

there were no constraints from the other two sides (axis-2). The nonsmooth contour could be attributed to withdrawing of the wire manually after the sample had cooled. The heat conductivity of the tungsten wire is significantly greater than those of the package sample sublayer materials so that the tungsten wire acted as a heat sink which attracted more heat flow in the defect region than in the intact region during the heating process.

The microstructure formation cause was investigated. The two sheets of plastic films were tightly clamped between one heating bar (with flat nonstick coating) and one pressure bar (thick flat rubber) during the sealing process (Figure 7.7). Heat was transferred from the heating bar and reached the contacting surfaces of the two films, causing them to melt and merge together. Noticing that the impedance values at the package sample back wall were always less than those at the front wall (see Section 7.2), and the back wall was the surface in contact with the heating bar (Figure 7.7), this led to an intuitive guess that the single-sided heating during the sealing process caused the asymmetric impedance profile.

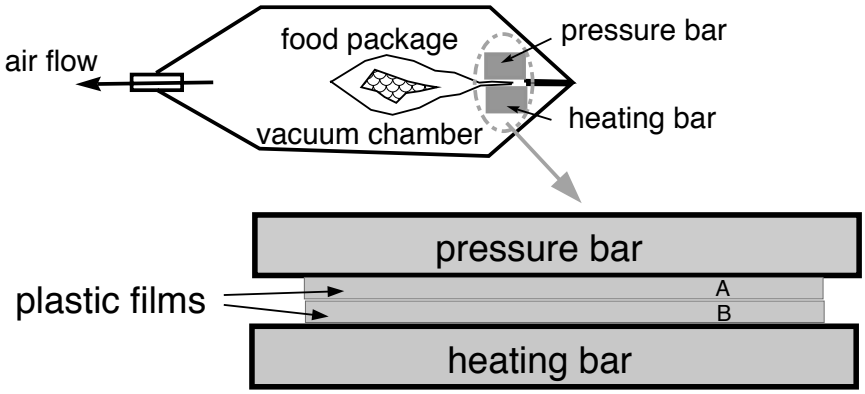

Figure 7.7 Illustration of heat sealing process.

The heat sealing process is a typical heat conduction process.[1] Temperature is associated with the kinetic energy of molecules. When molecular random motion

[1]Heat conduction is the transmission of heat through a substance without perceptible motion of the substance itself. Heat can be conducted through gases, liquids, and solids. In gases and liquids, random collisions of high-energy molecules with low-energy molecules cause a transfer of heat. Conduction of heat in solids (usually metals) is thought to be due to motion of free electrons, lattice waves, magnetic excitations, and electromagnetic radiation [102].

exists and a temperature gradient is present, heat transfer occurs via the conductive mode [102]. Temperature change affects material properties such as mass density and bulk modulus in a macroscopic sense. This is the basis for the intuitive conjecture that the single-sided heating during the sealing process caused the asymmetric impedance profile.

To verify this conjecture, evidence of a temperature gradient across the sample thickness dimension must be demonstrated. Consider the package sample thickness (220 μm) and the heating time (usually $1 \sim 2$ s), the temperature-time history inside the package sample would be our concern. A transient thermal finite element analysis (FEA) was performed in ANSYS[2] (ANSYS Inc., Canonsburg, PA, *http://www.ansys.com*) to solve the 2D heat conduction Equation (7.1).

The heat conduction Equation (7.1) can be derived from the first law of thermodynamics (thermal energy conservation law) and Fourier's law of heat conduction (experimentally observed relationship between the heat flux vector and the thermal gradient) [102]:

$$\hbar \nabla^2 \mathcal{T} + q''' = \rho c_v \frac{\partial \mathcal{T}}{\partial t} \tag{7.1}$$

where $\mathcal{T}$ is the temperature ($\mathcal{T}(x, y, z, t)$), $\hbar$ is the thermal conductivity of the material, ρ is the mass density, c_v is the specific heat, and q''' is the heat generation rate per unit volume. The operator ∇^2 is the Laplacian.

The material properties (ρ, c_v, $\hbar$) used in the ANSYS thermal analysis are listed in Table 7.1. Table 7.1 also lists the material melting points. For PVDC, the thermal conductivity and the specific heat are unavailable. Because the thermal analysis is not an exact quantitative analysis, these values are set by taking appropriate values from other similar material such as polystyrene. All the material properties in Table 7.1 are cited from [102]-[104].

The configuration of the thermal FEA is illustrated in Figure 7.8. To make the simulation more realistic to the real heat sealing situation, a 2000-μm-thick rubber layer was included to simulate the pressure bar which was in close contact with the top edge of sheet A in Figure 7.7.

[2]ANSYS is a commercial numerical simulation software that can perform finite element analysis in multiple domains such as structure mechanics, fluid dynamics, thermodynamics, acoustics, and electromagnetics. It is an industrial finite element analysis standard.

Table 7.1 Material thermal properties

material	thermal conductivity $\hbar$ [W/(mK)]	density ρ [kg/m^3]	specific heat c_v [J/(kgK)]	melting point (K)
polypropylene	0.1 - 0.13	900	2000	403
PVDC	N/A (use 0.05)	1650	N/A (use 0.157)	423
polystyrene	N/A	1050	0.157	N/A
oriented nylon	0.0138 (at 357.9 K)	1140	9.31e-7	N/A
tungsten	179 (at 273 K)	19300	134	3653
rubber	0.163	1150	2009	N/A

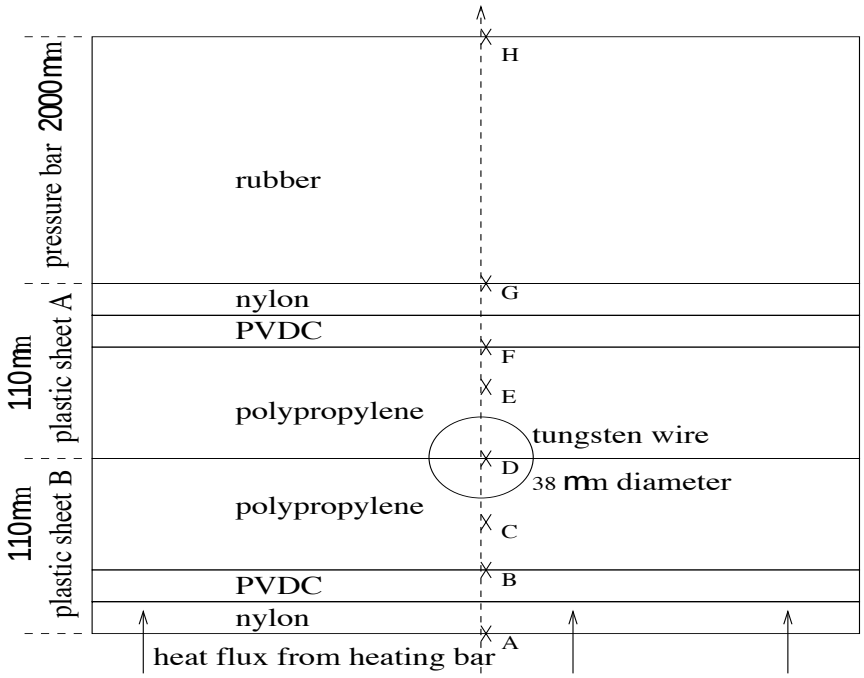

Figure 7.8 ANSYS heat conduction FEA configuration.

In the transient heat conduction FEA (Figure 7.8), the initial temperature was set at room temperature (293 K). The boundary condition on the bottom edge of sheet B was set as an incoming heat flux from the heating bar underneath, representing an intimate contact between the heating bar and the package material. The circle in Figure 7.8 was the 38-μm-diameter tungsten wire cross section. The eight X's were the designated temperature observation points (A, B, C, D, E, F, G, and H). Point A was on the bottom edge of sheet B. Point D was on the interface between sheets A and B. Point G was on the top edge of sheet A. Point H was on the top edge of the rubber layer.

Electrical AC voltage was applied on a metal strip in the heating bar. By electric-to-thermal energy conversion, heat was then emitted out from the two surfaces of the metal strip, half going to the package sample material and the other half going to the opposite direction. The measured electrical resistance of the metal strip was 1 Ω. Assuming that the electric-to-thermal energy conversion is 50%,[3] the total thermal power emited out from the heating bar would be $Q = 50\% \times 50\% \times U^2/R = 0.25 \times (24 \times 24/1) = 144$ W, where $U = 24$ V was the voltage value applied on the metal strip [105]. The area of the heating bar was 0.4 m by 0.08 m. So the heat flux would be $Q/A = 144/(0.4 \times 0.08) = 45$ kW/m^2. The heat flux function was plotted in Figure 7.9. The heat flux had a constant value of 45 kW/m^2 from 0.1 to 1.6 s, representing a heating phase. The heat flux was zero from 1.6 to 3.0 s, representing a cooling phase.

The thermal FEA was conducted on both the package samples with and without tungsten wire. The curves in Figure 7.10 showed that the temperature changed with different rates at different package sample depths. The temperature difference of about 150 K along the 220-μm sample thickness was demonstrated in the single-sided heat sealing process. The maximal temperatures of the curves in Figure 7.10 were inversely proportional to their depths from the bottom edge of the sheet B. The temperatures in sheet B (T_B, T_C, and T_D) did exceed the material melting point at the end of the heating phase. While the temperatures in sheet A (T_E, T_F, and T_G)

[3]It is hard to quantitively estimate the actual conversion percentage. The 50% estimation considers both the energy conversion efficiency and the energy loss in heat transfer from the metal strip to the package material.

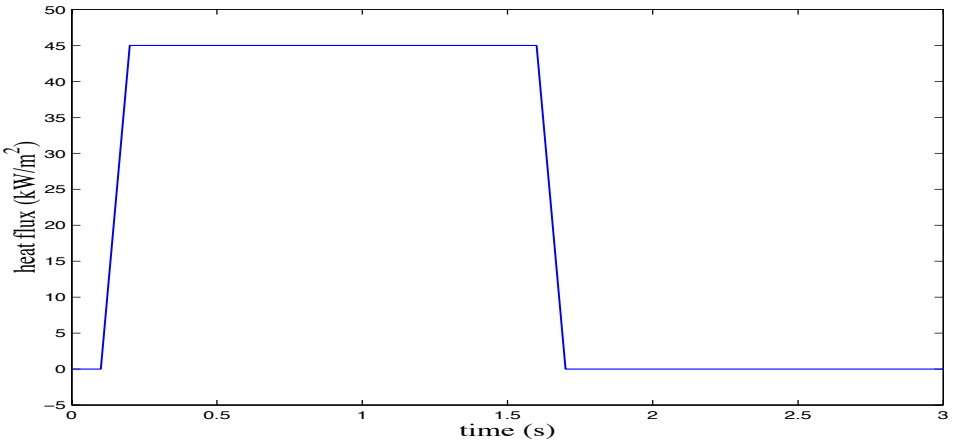

Figure 7.9 Heat flux versus time in the ANSYS heat conduction FEA.

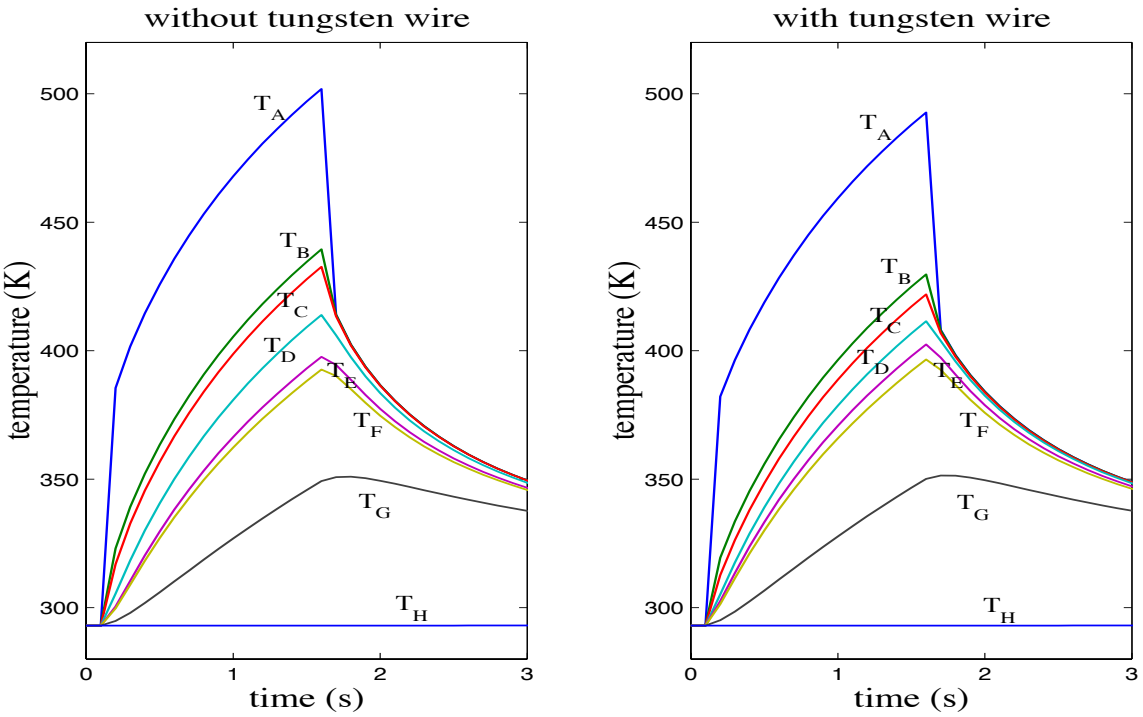

Figure 7.10 Temperature time history inside the package sample during the heat sealing process.

did not exceed the material melting point at the end of the heating phase. The two sheets would melt at their contacting surfaces but experience different temperature-time history. The actual package seal condition would depend on the amount of heat flux and the heating time in the heating process.

The introduction of the tungsten wire not only reduced the maximal temperature of each temperature curve, but also caused the curves around the tungsten wire region (T_C and T_E curves in Figure 7.10) to converge a bit more than the no tungsten wire case. It showed that the tungsten wire worked as a heat sink to attract a large amount of heat to its surrounding region. The intensive heat flow and the occupation of the tungsten wire in this region would cause material compounding around the tungsten wire.

Further experiments were done to investigate the microstructure formation cause. Figure 7.11 showed the measured package sample cross section impedance profiles for four cases. Figure 7.11(a) was the profile for a single sheet package film. The impedance profile showed a maximum impedance sublayer (PVDC sublayer). After sealing the two package film sheets (A and B in Figure 7.7), the PVDC sublayer near the top edge of sheet A had the maximum impedance but the other PVDC sublayer impedance decreased (Figure 7.11(b)). The impedance profile was asymmetric (see description for Figure 7.3). The sealed package sample underwent the second sealing process with the upper side down (flip A and B in Figure 7.7) after the first sealing was done. The measured impedance profile (Figure 7.11(c)) regained symmetry and the sharp dips after the PVDC sublayer became less striking. The double sealing made the impedance profile return to symmetry because each side of the sample experienced one heating process, exerting the balanced impact on the impedance profile. Furthermore, the third heat sealing process was done after the double sealing. This time the impedance profile (Figure 7.11(d)) became irregular because of the over-heating after the triple sealing process. But the asymmetric pattern appeared again, with the maximum occurring near the front wall.

All these experiments and FEM analysis support the intuitive conjecture about the formation cause of the package sample microstructure. It is the single-sided heating that causes the asymmetric impedance profile for the package sample. The unbalanced heat conduction induces asymmetric property changes during the sealing process.

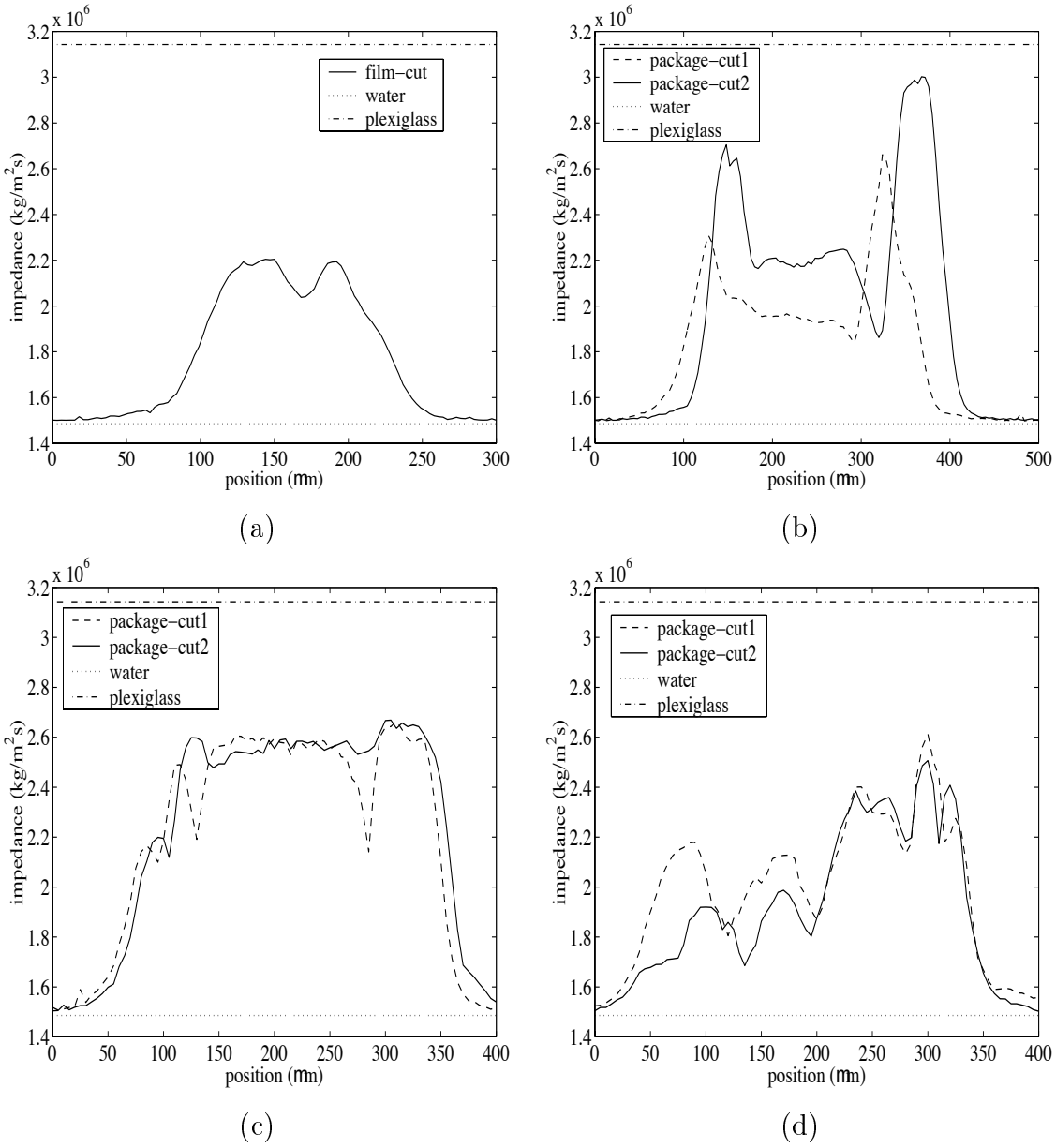

Figure 7.11 Package sample impedance profiles: (a) single sheet, no sealing; (b) double sheets, sealed once; (c) double sheets, sealed once from each side; (d) double sheets, sealed three times with two on one side and one on the other side.

CHAPTER 8

PACKAGE SAMPLE MICROSTRUCTURE: MODELING

The study in Chapter 7 revealed many interesting features and provided experimental evidence about package sample microstructure. Based on these observations, a generalized impedance model for the package sample is proposed in this chapter. The validity of this model is examined with numerical simulation of the pulse-echo defect detection behavior. The model parameters are discussed to understand the fundamental pulse-echo subwavelength defect detection mechanism.

8.1 Proposed Microstructure Modeling

Based on the nominal impedance properties and the microstructure measurement of the package sample, a generalized impedance profile was proposed. The generalized impedance model (Figure 8.1) includes features of the intact package sealing region and the channel defect region.

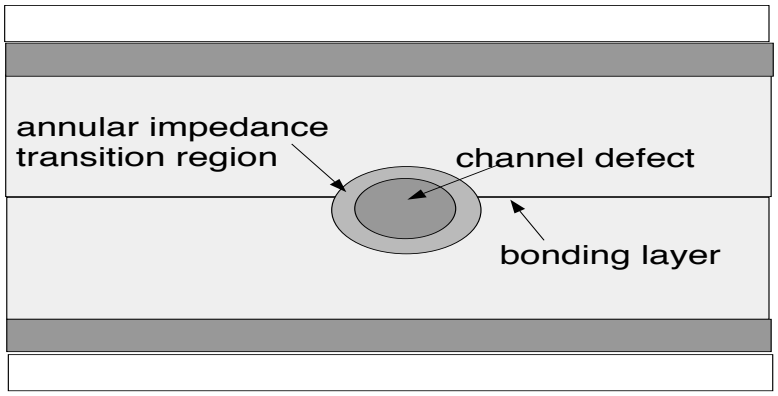

Figure 8.1 Proposed package sample microstructure impedance model. The bottom edge corresponds with the contacting surface with heating bar during heat sealing process.

For the intact package sealing region, the model considers (1) the asymmetric

impedance profile across the six sublayers whose thicknesses were depicted in Figure 7.1, (2) a bonding sublayer (impedance deviation sublayer) between the two plastic films, and (3) the frequency-independent weak attenuation inside the packaging material. The establishment of a generalized impedance model for the intact region is the prerequisite before constructing the model for the channel defect region.

For the channel defect region, the model considers (1) the channel defect elliptic shape and nonsmooth contour, (2) an annular impedance transition region surrounding the channel defect, (3) the channel defect position shift along the sample thickness dimension. These features were observed in Section 7.2.

By implementing the proposed impedance model, we hoped to establish a generalized model that would produce the simulated echoes with high similarity to the measured echoes (Figure 3.1) so that the above hypotheses could be examined in a numerical approach. Moreover, the parameters in the proposed model could be further evaluated to understand the fundamental mechanism in the pulse-echo subwavelength defect detection process.

8.2 Simulated Echoes

Figure 8.2 shows two impedance profiles along the pulse-echo beam axis. The impedance map was from a package sample with a 38-μm-diameter channel defect. The ultrasonic beam came from the right in both figures. The solid line corresponded to the intact region. The dashed line corresponded to a cut through the center of the defect. The channel defect was modeled as an ellipse with a 38-μm major axis and a 30-μm minor axis. The minor axis was parallel with the beam axis. The defect was filled with water (ρ = 1000 kg/m^3, c = 1485 m/s) and there was a 20-μm-thick surrounding annular region whose impedance was a bit higher than that of the intact region. The nonsmooth channel contour was constructed by inwardly or outwardly shifting a small position offset of 0-6 μm randomly on the smooth elliptic contour. The channel defect had a 35-μm position shift toward the package sample front wall. The package material attenuation coefficient was set as 20 dB/mm.[1] In the annular region, the attenuation coefficient was set as 40 dB/mm.[2] Both attenuation

[1]The value was taken from a measured pulse-echo insertion loss at 17.3 MHz

[2]The value was an estimation.

coefficients were assumed to be frequency independent.

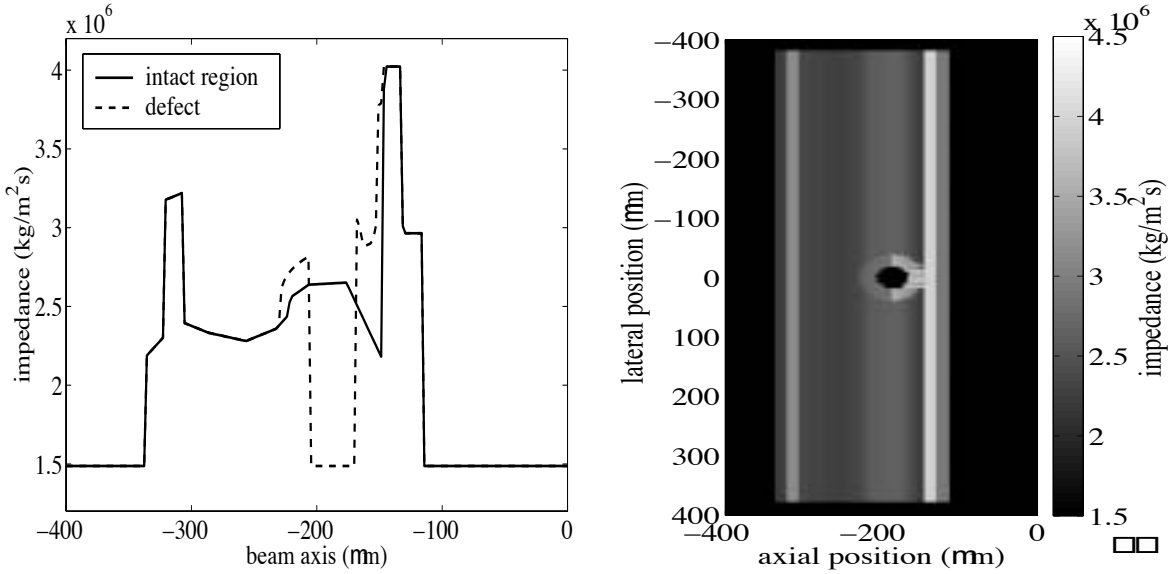

(a) (b)

Figure 8.2 Generalized impedance model: (a) impedance profile, and (b) impedance map of defect sample.

With this generalized impedance profile model, simulated echoes were obtained (Figures 8.3 and 8.4). The normalized cross correlation coefficient R between the simulated echo waveform and the experiment echo waveform was calculated as a quantitative index of similarity between them. The simulated results matched with experiment results very well ($R = 97.5\%$ for no defect situation and $R = 95.7\%$ for defect situation).

8.3 Discussion

The numerical evaluation has verified the validity of the proposed generalized impedance model in Section 8.1.

The asymmetric impedance profile, along with the uniform attenuation coefficient in the material, determined the echo waveform envelope shape in the intact region. The echo amplitude was not zero between the two echoes from package sample front and back walls because the corresponding impedance in this region was not uniform. The impedance variation caused reflection.

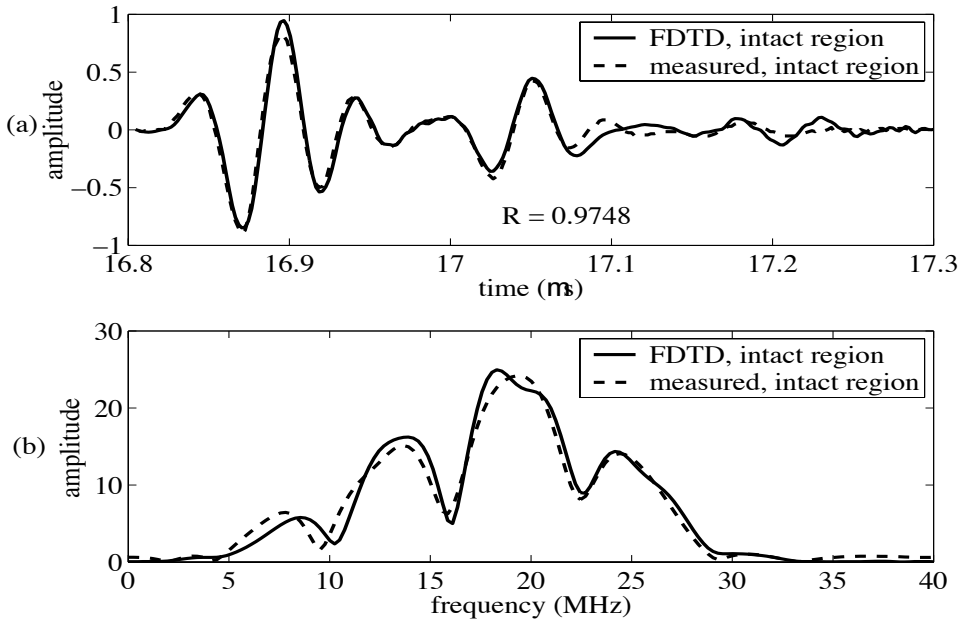

Figure 8.3 Echo waveform comparison between simulation and experiment, intact region, time domain (a) and frequency domain (b).

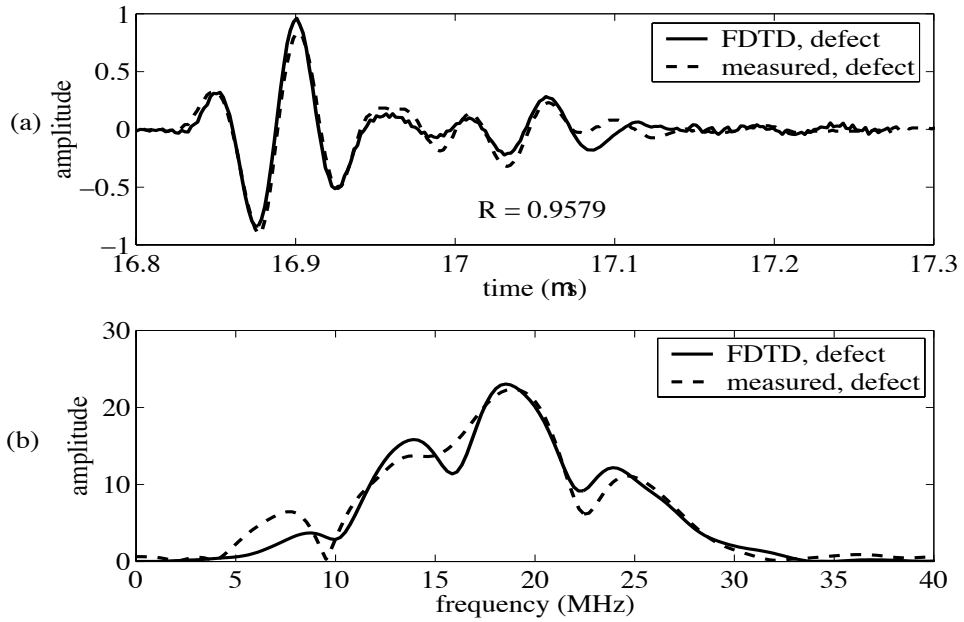

Figure 8.4 Echo waveform comparison between simulation and experiment, channel defect, time domain (a) and frequency domain (b).

It has been found that the channel defect alone could not produce significant echo amplitude variation in the time portion between the two echoes from the package sample front and back walls. The insertion of tungsten wire during the heat sealing process took up the volume originally occupied by package material. Consequently, the annular region was produced by material compounding during the heat sealing process. Because of the material compounding, this region tended to be more solid-like with an impedance value higher than that of its surrounding medium. The impedance difference between the annular region and the defect region (water) increased. So did the variation in the echo waveform portion corresponding the defect region.

The shape and position of the channel defect also played an important role in determining the echo waveform. If the defect shape were smooth and round, caustics would occur because the perturbation of the smooth scatterer acted as a focal lens to the incident acoustic rays. The consequence of the caustics would produce an enhancement of wave intensity somewhere behind the smooth scatterer, depending on the curvature. If the distance happened to be inside the package sample, the echo amplitude would increase behind the defect. However, the measured echo from the channel defect showed that the echo amplitude decreased behind the defect when compared with the echo from the intact region. The nonsmooth defect contour broke the condition to form caustics by randomly diverting the acoustic rays into different directions around the defect.

In conclusion, it is a very challenging task to model every aspect of the pulse-echo subwavelength defect detection process. Because of the limited knowledge in microstructure information, several assumptions had to be made to "guess" the true details of the package sample. For example, the acoustic impedance measurement provided only an approximated impedance map due to the transducer lateral resolution limitation ($BD_{(-6\text{dB})} = 52.9\ \mu\text{m}$). Several important microstructure features were evaluated through numerical simulation in this study. The simulation results verified the hypotheses about these features and explained the reason for the waveform variations between echoes from intact and channel defect regions in ultrasonic pulse-echo subwavelength channel defect detection.

CHAPTER 9

SUMMARY

Flexible food packages are gaining more and more popular usage nowadays for offering the consumer cheap, lightweight, durable, and easy-to-open soft containers. Scientific studies and consumer surveys have shown that flexible packages have many advantages over glass bottles or metal cans, such as better product quality and nutrition preservation for various types of foods, less energy consumption and processing time in manufacture, cheaper product shipping cost, less storage space requirement, and more enjoyable convenience.

Flexible food packages are produced by hermetically fusing the opposing seal surfaces to avoid postprocess contamination of the product. Sealing is the critical step in the use of flexible food packages because postprocess contamination of the processed foods is mostly linked to seal and package integrity issues such as channel leaks and imperfect bonds. It has been known that certain microorganisms can transit through 10-μm-diameter or smaller channels. The package seal integrity must be tested for potential defects formed during or post production because poor seal integrity could cause product loss and compromise safety and public health, and the U.S. government is pressing for zero tolerance of pathogens in foods.

However, current quality assurance techniques in the food industry only provide statistical assurance, having no safety guarantee of untested packages. They are time-consuming and expensive due to personnel costs and product loss. Therefore, effective and reliable nondestructive seal integrity tests are critically needed for quality assurance purposes.

The food packaging ultrasonic inspection project studied the feasibility of developing a novel high performance nondestructive testing modality for real-time package seal integrity inspection. Previous efforts in this project have developed several ultrasonic pulse-echo defect detection and imaging techniques, including RF sample (RFS), RF correlation entire range (RFCE), RF correlation specific range (RFCS), parametric ARX-modeling, and backscattered amplitude integral (BAI)-

mode imaging. All these methods can detect channel defects embedded in bonded two-sheet package samples. The detectable channel defect sizes (6 μm smallest possible) of these methods in laboratory experiments are much smaller than the human observer inspection limit ($\sim$50 μm).

Among all these methods, the BAI-mode imaging technique is a simple, general pulse-echo blind detection method for microchannel defects in food package samples with a decent detection rate. Like C-scan type images, the BAI-mode image is a plane projection of the internal details of sample. The image pixel values are obtained by calculating an envelope-time integral for the RF echo waveforms at each transducer scanning location. If a defect is present, the RF echo waveform will be different from the echoes in the intact region. The change in BAI-values indicates RF echo waveform change, which contains information about the defect location. The BAI-mode imaging technique has a 100% detection rate for cylindrical channels greater than 38 μm in diameter in bonded two-sheet plastic film samples (thickness 110 μm per sheet) with a spherical focusing immersion-type transducer working at 17.3-MHz center frequency. Moreover, channel defects as small as 6 μm in diameter could be detected occasionally.

There are two very interesting observations about the ultrasonic BAI-mode imaging technique: (1) The BAI-mode imaging technique requires no *a priori* information about sample (speed of sound, mass density). Therefore, it can perform blind inspection and has the potential to become an economical, real-time on-line food package sealing integrity inspection methodology. (2) On the other hand, the BAI-mode imaging technique has sensitive subwavelength defect detection capability. Although the BAI-mode imaging technique is a typical pulse-echo backscattered imaging method, the fundamental mechanism of the subwavelength defect detection capability is poorly understood.

The study presented in this thesis is closely related with the food packaging inspection project. Two research challenges were identified from the two observations mentioned above: (1) How can the BAI-mode imaging technique be applied to real world package product line inspection? and (2) Why is the BAI-mode image technique able to perform subwavelength detection?

The first research challenge was investigated through an experimental approach. To bring the BAI-mode imaging technique closer to real world application, a real-

time zigzag raster scanning pattern has been developed to replace the previously used rectilinear stop-and-go scanning pattern and to simulate the package product line inspection scenario. The engineering trade-off between the BAI-mode image quality (lateral and contrast resolutions) and the real-time spatial sampling pattern has been investigated through quantitative image assessment. Two transducers ($f^{\#}/2$ 17.3 MHz and $f^{\#}/3$ 20.3 MHz) were used to acquire RF echo data in a zigzag raster pattern from plastic film samples bearing rectilinear point reflector arrays of varying grid spacings. The average BAI-value difference (ΔBAI) between defective and intact regions and the contrast-to-noise ratio (CNR) were used to assess image quality as a function of three spatial sampling variables: transducer spatial scanning step size, array sample grid spacing and transducer -6-dB pulse-echo focal beam spot size. Our study showed that for a given grid size, the ΔBAI and CNR degraded as scanning step size in each spatial dimension increased. There was an engineering trade-off between the BAI-mode image quality and the transducer spatial sampling. The optimal spatial sampling step size had been identified to be between one and two times the -6-dB pulse-echo focal beam lateral diameter.

The second research challenge has been investigated using a numerical approach. A theoretical modeling study was undertaken to investigate the origin of the BAI-mode image contrast, and establish a generalized numerical model for the pulse-echo subwavelength defect detection system. The ultrasound beam encounters complex structures in its propagation path during pulse-echo defect detection operation: the package sample front wall, interfaces between sublayers, heat-fusing zone between the two plastic sheets, the channel itself, impedance deviation surrounding the channel, and the package sample back wall. A 2D numerical tool using the finite-difference time-domain (FDTD) method with the perfectly matched layer (PML) absorbing boundary technique was developed to simulate the ultrasonic pulse-echo defect detection process and to numerically evaluate the aforementioned interactions between ultrasound beam and sample microstructure.

Microscopic optical imaging and impedance measurement of package sample cross section microstructure revealed many interesting microstructure features such as an asymmetric impedance profile, elliptic channel defect shape and nonsmooth channel defect contour, position shift of channel defect and material shrinkage and bending in defect region. The package cross section microstructure formation cause was

studied by finite element heat conduction analysis of the heat sealing processing. The experiments and analysis provided the evidence and basis to propose a generalized impedance model about the package sample cross section microstructure. The proposed package sample microstructure model, which included the observed features was incorporated into the numerical simulation tool to examine its validity. The normalized cross correlation coefficient R between the simulated echo waveform and the experiment echo waveform was calculated as a quantitative index of similarity between them. The simulated results matched with experiment results very well (R = 97.5% for no defect situation and R = 95.7% for defect situation).

APPENDIX A

SCANNING AND DATA ACQUISITION SYSTEM DESCRIPTION

The system (Figure A.1) consists of four-axis (three linear and one rotational axes) precision positioning system (Daedal Inc., Harrison City, PA), focused transducer (model V317, Panametrics, Waltham, MA), pulser/receiver (model 5800PR/5900PR, Panametrics), digital oscilloscope (model 9354TM, LeCroy, Chestnut Ridge, NY), GPIB interface, system controller (Pentium 166 MHz PC) and control software (Microsoft Visual C++, version 6.0, Redmond, WA) developed in BRL.

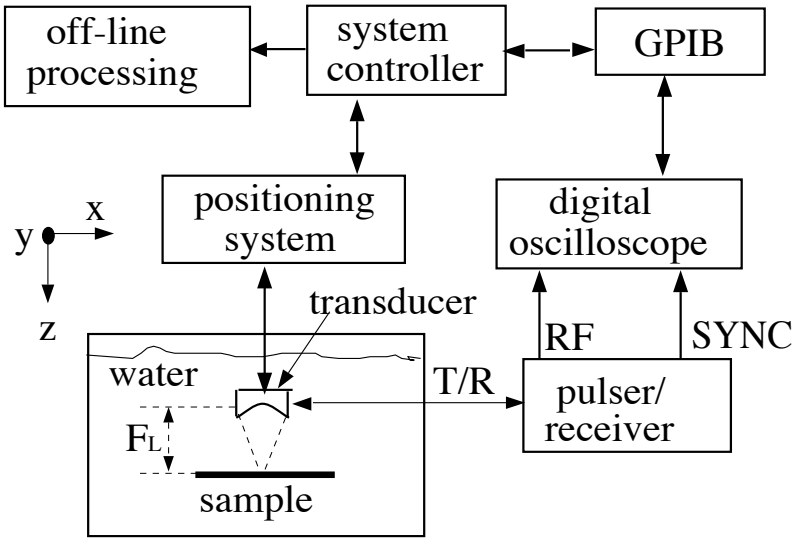

Figure A.1 Block diagram of the scanning and data acquisition system.

The precision positioning system (Figure A.2) consists of three linear axes (axes 1, 2, 3) and one rotational axis (axis 4), each controlled by separate stepper motors. Axes 1, 2, and 3 correspond with the y, x, and z translational axes. The manufacturer-specified accuracy is ± 5 μm for the linear axes and $\pm 0.01^{o}$ for the rotational axis. The motors for each axis are controlled by stepper motor drives (Zeta

Drive, Parker Hannifin Corp., Cleveland, OH), an indexer (AT6400, Parker Hannifin Corp.), and software developed for this equipment (Parker Hannifin Corp.). Each of the four motors has its own encoder and is connected to its own motor driver. The indexer is responsible for controlling and organizing the programs created to interface with the motors. The encoder with each motor can report current motor status, which in turn can be translated to current position of the axis to which the motor is attached.

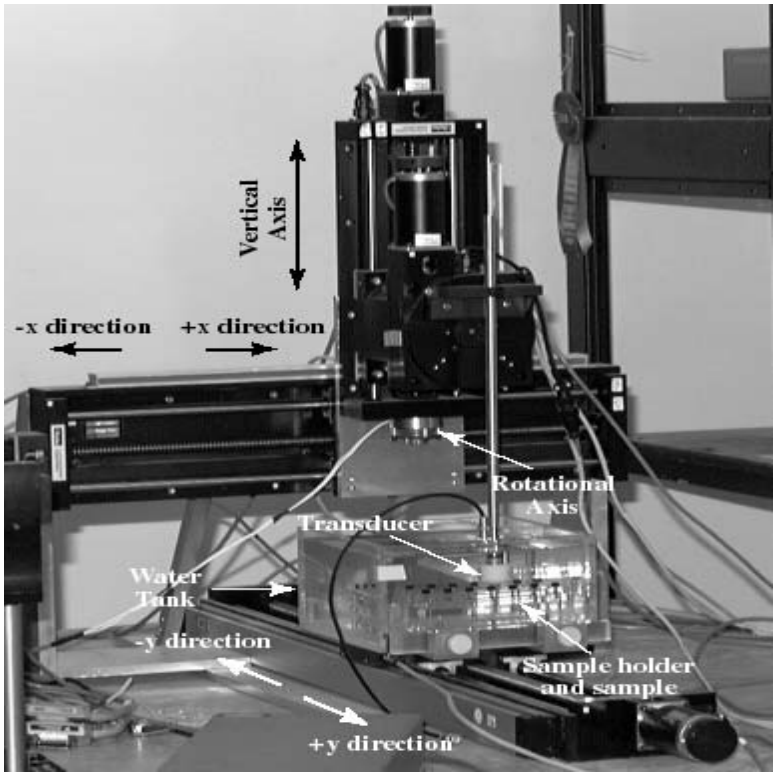

Figure A.2 Picture of precision positioning system.

The transducer is mounted on the positioning system and immersed, together with plastic sample, in degassed water ($\mathcal{T} \approx 20$ °C, $c \approx 1485$ m/s) (Figure A.3). The plastic sample is affixed to a plastic holder and placed in the focal plane (x-y plane) of the transducer by adjusting the transducer position in z-axis and the rotational axis, which are not activated while the sample is scanned. The holder is capable of tightly clamping the sample at the border between the sealed and unsealed regions. The plastic sample surface is approximately normal to the transducer beam axis (z-axis). This round-trip time span corresponding to the focal length of the transducer is found

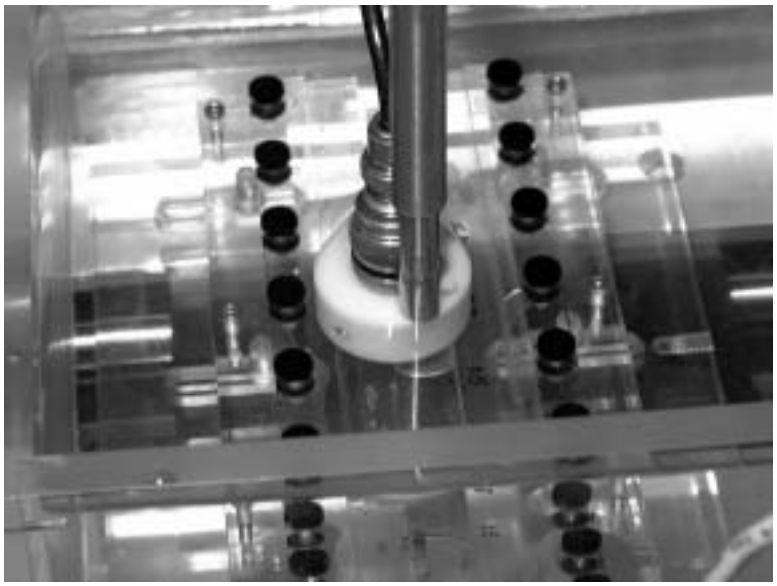

Figure A.3 Sample holder and transducer.

by calculating a time of transition $TOT = \frac{2 \times F_L}{c_{water}}$, where F_L is the focal length, and c_{water} is the speed of sound in water.

The duties of the precision positioning system are to (1) move sample and transducer in a controlled scanning manner, and (2) report position reading in each axis. In the experiments, the Plexiglas tank containing sample moves in the y direction and the transducer moves in the x direction. Every time a new echo waveform is acquired, the digital oscilloscope's status register sets itself to "true"(logical 1), which will be used to trigger the motor encoders to report motor position readings. The (x, y) position is then recorded by control software.

Operating in the pulse-echo mode, the pulser/receiver is used to generate an electric pulse and send it to the ultrasonic transducer. Ranges of parameters selected for the pulser/receiver are listed in Table A.1. Excited by the electric pulse, the transducer sends out an ultrasound wave pulse and receives the echo pulse at each scanning location (x, y) from the sample. The pulser/receiver then receives the RF echo waveform from the electric output of the transducer and sends it out to the digital oscilloscope. The digital oscilloscope collects the entire RF echo waveform between time t_1 and t_2 at 500 Msample/s with 256 time sequence samples at each scanning location and sends them to system controller via GPIB connection. The communication between the system controller and the positioning

system is over a bus-based line. The 3D ultrasound data set $\{p(x_i, y_i, t_j)$: scanning location $x_i, y_i \in$ planar sample surface to be scanned, sampling time instance $t_j \in [t_1, t_2], j = 0, 1, \cdots, 255\}$ is stored as binary data files for off-line data processing and image formation on a Unix workstation using MATLAB (The Math Works, Inc., Natick, MA).

Table A.1 Pulser/Receiver parameters

MODE	P/E	ATTENUATORS	0 dB
PRF	500Hz-10kHz	GAIN	26 dB
ENERGY	16-32 μJ	RF OUTPUT PHASE	0^o
DAMPING	30-50 W		
HP FILT	1 MHz		
LP FILT	200 MHz		

When the transducer center frequency is above 30 MHz, a remote pulse preamplifier has to be used to reduce the high frequency noise introduced by long cable between transducer and pulser/receiver. Being powered and trigged by its host pulser/receiver (5900PR, Panametrics), the remote pulse preamplifier (model 5627RPP, Panametrics) excites the high frequency transducer through a very short coaxial cable (typically 12 inch/305 mm long). The returning echoes are amplified by a high frequency broadband preamplifier, and then sent to its host pulser/receiver through a long cable (Figure A.4). The damping and energy levels can be adjusted in 5627RPP. The short cable connecting the 5627RPP to the transducer minimizes undesirable cable effect. The operating mode of the host pulser/receiver (5900PR) must be set as RPP.

Figure A.5 shows the graphical user interface (GUI) of the system control software (program name "*Package Data Acquisition*"), which is installed in "*daedal3*" computer next to the positioning system. The "*Position*"part of the software is used to position the transducer and the sample. Selecting "Axis-2"(x-axis) and "Axis-3"(z-axis) moves the transducer, and selecting "Axis-1"(y-axis) moves the sample. The "*Reading*"part always indicates the current position of the three axes with respect to updated position, and initialized to "+0.0000"in mm when the software is first opened. Pressing "*Update Position*" button will initialize the location to

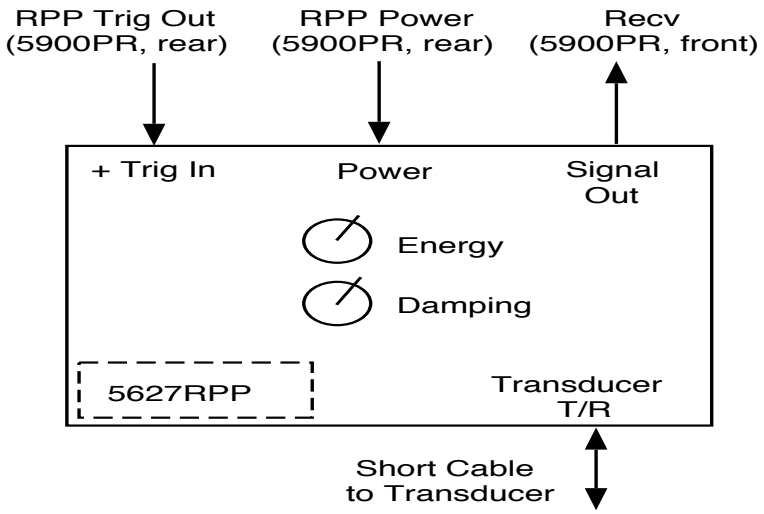

Figure A.4 Usage of 5627RPP remote pulser preamplifier.

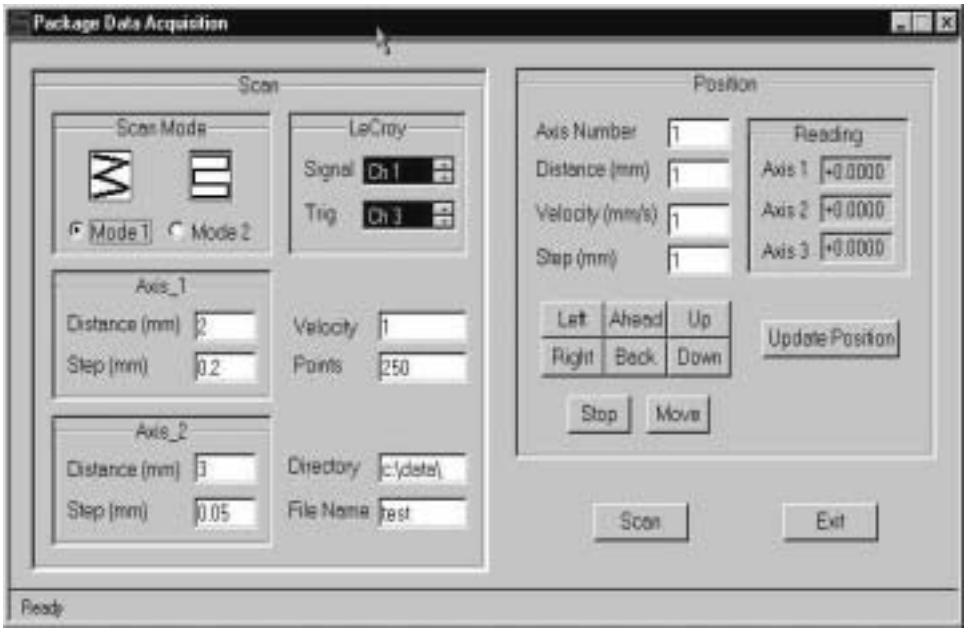

Figure A.5 Package data acquisition software interface.

"+0.0000" before proceeding for scanning. In order to move the transducer or sample, select the desired axis, distance, velocity, and step size and press "*Move*." Pressing "*Stop*" will stop the movement in the middle of the process. Another way of adjusting the transducer position is selecting buttons such as "*Left*" (-axis-2), "*Right*" (+axis-2), "*Ahead*" (-axis-1), "*Back*" (+axis-1), "*Up*" (+axis-3), and "*Down*" (-axis-3). These buttons move the transducer 1.00 mm in the corresponding direction each time. The parameters for scanning can be set by using the "*Scan*" part of the software, such as scan mode (Mode 1: zigzag raster scan, Mode 2: rectilinear scan), step sizes and total scan distance in the selected axes, channels for trigger and received signals in the oscilloscope, velocity (in millimeters per second) of axis-2, number of sampling data points in every received RF echo waveform, and the directory and file name in which these collected data are to be saved. The step size in the x direction is the distance between transducer neighboring scanning positions. The step size in the y direction is the distance between the turning points of two neighboring scan rows. These parameters are written in a single data file ("*filename.dat*").

In both scan modes, the transducer moves back and forth in axis-2. The motors collect transducer scanning positions and the oscilloscope acquires RF echo waveforms at the same time. When the transducer spans one scanning row, both axes stop long enough for the acquired waveforms to be sent from the oscilloscope to the system controller via the GPIB connection. This completes one forward scan row. Once this is done, the transducer turns back to opposite direction for the backward scan row. The acquired waveforms are again sent from the oscilloscope to the system controller after the motors stop. This process continues until the entire scan area is covered. For each row of data acquired, new data files for both the waveforms and motor positions are written as "*filenamexx.bin*" and "*filenamexx.ter*," where xx standards for scan row index number.

APPENDIX B

PACKAGE SAMPLE PREPARATION

The package sample uses two 110-μm-thick trilaminate films (Fuji Tokushu Shigyo Co. Ltd., Seto Aichi, Japan). Each trilaminate film has three sublayers: polypropylene (80 μm, c = 2660 m/s, ρ = 900 kg/m^3), polyvinylidene chloride (PVDC, 15 μm, $c = 2380$ m/s, $\rho = 1650$ kg/m^3), oriented nylon (15 μm, $c = 2600$ m/s, ρ = 1140 kg/m^3). The calculated average speed of sound in the film is about 2500 m/s. Polypropylene is the inner heat-sealing sublayer. The middle sublayer (PVDC) provides a barrier to chemical substances. The outer layer (nylon) gives strength, barrier to gases, oils and fats, and scuff resistance to the printed surface [49].

The channel defect package sample was produced by using a heat sealer (Audionvac-VM151HG, Audion Electro, Weesp, Holland) to fuse a smooth, die-drawn tungsten wire (California Fine Wire Company, Grover City, CA) in two plastic trilaminte package films. The heat sealer has a chamber with a heavy lid. Attached with the lid was a flat rubber bar to apply uniform pressure on the package sample. Inside the chamber was a flat heating bar with nonstick teflon coating. After closing the lid, the package sample was clamped between the flat rubber bar and the flat heating bar to ensure intimate contact of the two inner faces (Figure 7.7). The chamber was first evacuated to expel the air inside the food package sample. Then the heating bar was heated to the designated temperature ($\sim$ 130 ^{o}C) within a user-specified amount of time (1 $\sim$ 2 s). The heat was applied from the heating bar and passed through the sublayers to melt and fuse inner sealant layers together. The sample was then cooled to room temperature.

Tungsten wires with different diameters (6, 10, 15, 25, 38, 50, or 75 μm) were sandwiched transversely to the sealing direction between two inner sublayers to fabricate different sized channels. The wire was then removed along its axial direction after the package sample had cooled (Figure 7.1). Sealing the two channel ends would produce an air-filled channel. Immersing the fused plastic sample in degassed water would create a water-filled channel.

APPENDIX C

ACOUSTIC IMPEDANCE MEASUREMENT PROCEDURE

This appendix presents the acoustic impedance measurement experimental procedure. The so-called pulse-echo reference measurement procedure measures RF echo waveform amplitude, with the same equipment settings, from both a reference material plate whose impedance value is known and the unknown material whose impedance value is to be determined. A simple follow-up mathematical operation calculates the acoustic impedance value for the unknown material. It is a widely used procedure. This appendix briefly recites the principle and describes the procedure used in this study.

Recall the plane wave reflection phenomenon (see Section 1.5), at an infinite planar interface between two media (acoustic impedance values Z_1 and Z_2, respectively), the plane wave reflection coefficient $R = \frac{Z_2 - Z_1}{Z_2 + Z_1}$. The echo amplitude $P_{echo} = |R| P_{incident}$. Because the reflection coefficient between water and the reference material (R_{w-g}) is known, the reflection coefficient between water and the unknown material (R_{w-m}) can be calculated by comparing the echo amplitudes in both cases (C.1):

$$\begin{aligned} P_g &= |R_{w-g}|\, P_{inc} \\ P_m &= |R_{w-m}|\, P_{inc} \end{aligned} \longrightarrow \left|\frac{R_{w-m}}{R_{w-g}}\right| = \frac{P_m}{P_g} \Rightarrow |R_{w-m}| = |R_{w-g}|\,\frac{P_m}{P_g} \tag{C.1}$$

$$R_{w-g} = \frac{Z_g - Z_w}{Z_g + Z_w}, \quad R_{w-m} = \frac{Z_m - Z_w}{Z_m + Z_w} \tag{C.2}$$

The procedure uses a plexiglas plate as the reference material plate. The subscript w and g standard for water and Plexiglas, respectively. Plugging (C.2) into (C.1), the explicit expression for the unknown acoustic impedance is

$$Z_m = Z_w \frac{1 + |R_{w-g}|\,\frac{P_m}{P_g}}{1 - |R_{w-g}|\,\frac{P_m}{P_g}} \tag{C.3}$$

The above derivation is based on a continuous plane wave frequency domain propagation model. Media 1 and 2 are both assumed to be semi-infinite and the

interface between media 1 and 2 is assumed to be infinitely large. However, it is also a good approximation for the pulse convergent wave incidence at the interface between two media. There are two restrictions when using this procedure: (1) sample (medium 2) has to be thick enough (much thicker than 50λ) so that medium 2 can be approximately semi-infinite; and (2) the transducer beam spot size has to be much smaller than the lateral dimension of the interface between water (medium 1) and the sample (medium 2).

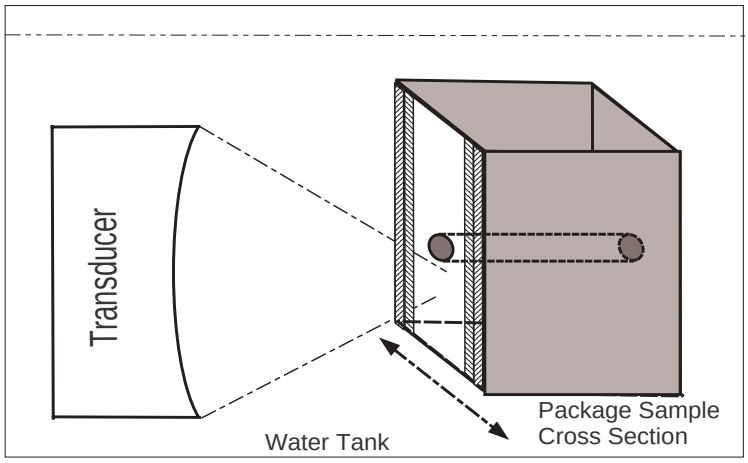

Figure C.1 Pulse-echo scan of package sample cross section.

To measure the package sample impedance profile, a package sample is perpendicularly cut by a single side razor blade to obtain its cross-section. Two steps were involved in measuring the impedance profile: (1) A focused transducer (37.4 MHz, $BD_{(-6\text{dB})} = 52.9$ μm) scanned a flat Plexiglas surface whose impedance value is known (reference echo). (2) The transducer scanned the package sample cross section (220 μm thick) at 5-μm step size, with beam axis parallel to package sample planar surface (Figure C.1). The echo amplitude at each scanning location was compared with the reference echo to determine the impedance at each scan location by (C.3). The second restriction becomes invalid in the vicinity of sample front and back edges. Value correction is thus needed at both ends of the impedance profile.

APPENDIX D

FDTD AND PML FORMULATION

The finite-difference time-domain (FDTD) method is a time domain numerical method to solve wave equations by evolving the wave field through space and time. A perfectly matched layer (PML) truncates the FDTD computational domain. The absorption inside PML provides a reflectionless boundary between the physical FDTD domain and the nonphysical PML, which emulates the free space environment for the wave propagation. The PML is a key technique for the numerical simulation related to open space wave propagation simulation.

The computer implementation of the FDTD with PML simulation is straightforward. Starting from the basic acoustic equations, this appendix presents the derivation details for the formula used in the implementation. The first order acoustic equations in a homogeneous, lossy fluid medium are

$$\begin{aligned} \nabla p(\mathbf{r},t) &= -\rho\frac{\partial}{\partial t}\mathbf{u}(\mathbf{r},t) - \alpha^*\mathbf{u}(\mathbf{r},t) \\ \nabla\cdot\mathbf{u}(\mathbf{r},t) &= -\kappa\frac{\partial}{\partial t}p(\mathbf{r},t) - \alpha p(\mathbf{r},t) \end{aligned} \tag{D.1}$$

where t is time, $\mathbf{r}$ is vector field point, p is the scalar pressure field, $\mathbf{u}$ is vector particle velocity field, ρ is the mass density of the medium, κ is the compressibility of the medium, α is the compressibility attenuation coefficient in acoustic media, α^* is the attenuation coefficient associated with mass density ($\alpha^* = 0$ in acoustic media in general). The term α^* is introduced here since the PML method relies on the introduction of a nonphysical density attenuation in the absorbing layers.

Assuming $\exp(-i\omega t)$ time dependence, the speed of sound and the complex wavenumber for (D.1) are $c = \sqrt{1/\kappa\rho}$ and $k = \frac{\omega}{c}\sqrt{\left(1 - i\frac{\alpha^*}{\omega\rho}\right)\left(1 - i\frac{\alpha}{\omega\kappa}\right)}$. If the medium property satisfies $\alpha^* = \alpha\rho/\kappa$, then $k = \left(\frac{\omega}{c} - iz_0\alpha\right)$ and $z_0 = \sqrt{\rho/\kappa}$. In such a medium, the phase speed and acoustic impedance are independent of the attenuation value. For a plane wave normally incident on a half space boundary between a lossless acoustic medium (κ, ρ, $\alpha = 0$) and a medium with (κ, ρ, α, $\alpha^* = \alpha\rho/\kappa$), there is no reflection. The second medium is called a perfectly matched

medium. If the attenuation in the perfectly matched medium is made anisotropic, the incident wave at all angles can be absorbed.

The idea behind a PML boundary condition is to define a nonphysical set of equations in the PML region which exhibit large attenuation but do not produce any reflections for a wave propagating into the PML region from an adjoining lossless acoustic region. For the 2D case, p is first split into two additive components, $p = p_x + p_y$, with p_x related to $(\partial/\partial x)u_x$ and p_y related to $(\partial/\partial y)u_y$. The term α is assumed to be anisotropic $\bar{\bar{\alpha}} \equiv \begin{bmatrix} \alpha_x & 0 \\ 0 & \alpha_y \end{bmatrix}$. The acoustic PML equations in the 2D case are then transformed to

$$\begin{aligned} -\rho\frac{\partial}{\partial t}u_x - \frac{\alpha_x\rho}{\kappa}u_x &= \frac{\partial}{\partial x}p \\ -\rho\frac{\partial}{\partial t}u_y - \frac{\alpha_y\rho}{\kappa}u_y &= \frac{\partial}{\partial y}p \\ -\kappa\frac{\partial}{\partial t}p_x - \alpha_x p_x &= \frac{\partial}{\partial x}u_x \\ -\kappa\frac{\partial}{\partial t}p_y - \alpha_y p_y &= \frac{\partial}{\partial y}u_y \end{aligned} \tag{D.2}$$

Note that if $\alpha_x = \alpha_y$, (D.2) can be simplified to (D.1). Equation (D.2) is a general form for equations in both the acoustic and PML media. Let $\hat{u}$ be the unit vector of $\mathbf{u}$, $\mathbf{a}$ be the unknown direction vector for the mathematic two-component pressure field $\mathbf{p}$, and $\mathbf{k}$ be the unknown vector wavenumber,

$$\begin{aligned} \mathbf{u} &= \hat{u}e^{i\mathbf{k}\cdot\mathbf{r}} \qquad \mathbf{p} = \mathbf{a}e^{i\mathbf{k}\cdot\mathbf{r}} \\ \mathbf{u} &= \begin{bmatrix} u_x \\ u_y \end{bmatrix} \quad p = \mathbf{p}\cdot\begin{bmatrix} 1 \\ 1 \end{bmatrix} \end{aligned} \tag{D.3}$$

Substituting (D.3) into (D.2), the solution for the unknowns $\mathbf{k}$, $\mathbf{a}$, and the plane wave solution are

$$\begin{aligned} \mathbf{k} &= \left(\tfrac{\omega}{c} - iz_0\bar{\bar{\alpha}}\right) \qquad \mathbf{a} = z_0\bar{\bar{u}}\hat{u} \\ \bar{\bar{\alpha}} &\equiv \begin{bmatrix} \alpha_x & 0 \\ 0 & \alpha_y \end{bmatrix} \quad \bar{\bar{u}} \equiv \begin{bmatrix} \hat{u}_x & 0 \\ 0 & \hat{u}_y \end{bmatrix} \end{aligned} \tag{D.4}$$

$$\begin{aligned} \mathbf{u} &= \hat{u}e^{-i\frac{\omega}{c}\mathbf{x}\cdot\hat{u}}e^{-z_0\mathbf{x}\cdot\bar{\bar{\alpha}}\hat{u}} \\ \mathbf{p} &= z_0\bar{\bar{u}}\hat{u}e^{-i\frac{\omega}{c}\mathbf{x}\cdot\hat{u}}e^{-z_0\mathbf{x}\cdot\bar{\bar{\alpha}}\hat{u}} \end{aligned} \tag{D.5}$$

The plane wave in the PML medium travels at the same speed as a plane wave in a lossless acoustic medium with (κ, ρ, $\alpha = 0$). In addition, the wave impedance is $z_{PML} = \frac{|p_x+p_y|}{|\mathbf{u}|} = z_0$.

The discretized PML boundary equations (D.9) can be derived by applying the central finite difference scheme for space derivatives (D.6) and exponential differentiation to time derivatives (D.7) into (D.2):

$$\frac{\partial f_{x,y}(i,j)}{\partial x} = \frac{f_{x,y}(i+1,j) - f_{x,y}(i-1,j)}{2\triangle} \tag{D.6}$$

$$\kappa p'\left(\left(l+\frac{1}{2}\right)h\right) + \alpha p\left(\left(l+\frac{1}{2}\right)h\right) \approx \frac{\alpha(p^{l+1} - p^l e^{-\alpha h/\kappa})}{1-e^{-\alpha h/\kappa}} \tag{D.7}$$

where $\triangle$ is the FDTD spatial grid size, h is the time sample interval, l is the time index. Causality and stability of the FDTD simulation require that

$$\triangle = \frac{\lambda_{min}}{10} \quad \lambda_{min} = \frac{\lambda_{min}}{f_{max}} \quad h = \frac{\triangle}{2c_{max}} \tag{D.8}$$

where λ_{min} is the minimal wavelength, c_{min} is the minimal speed of sound, f_{max} is the maximal frequency in the simulation domain.

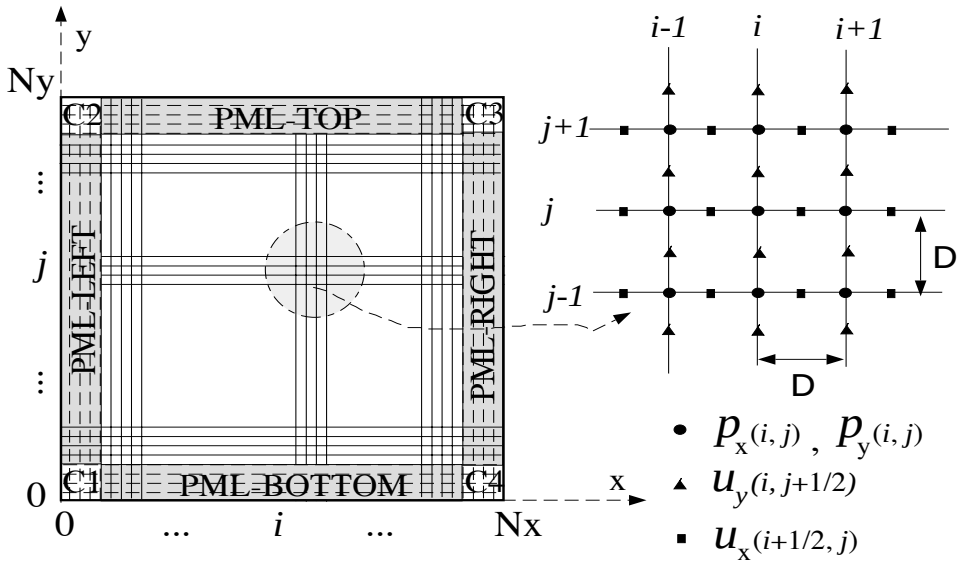

Figure D.1 FDTD grid.

Equation (D.9) constructs a spatial-temporal evolution scheme (Figure D.1) similar to the well-known Yee's grid. The term l is the time step. The expression $l = l + 1$ in (D.9) represents time step increment. The pressure variables are taken

at the grid intersections. The velocity variables are taken at half grids.

$$
\begin{aligned}
p_x^{l+1}(i,j) &= p_x^{l+1}(i,j)e_x^{(1)}(i,j) - e_x^{(2)}(i,j)\left[u_x^{l+\frac{1}{2}}(i+\frac{1}{2},j) - u_x^{l+\frac{1}{2}}(i-\frac{1}{2},j)\right] \\
p_y^{l+1}(i,j) &= p_y^{l+1}(i,j)e_y^{(1)}(i,j) - e_y^{(2)}(i,j)\left[u_y^{l+\frac{1}{2}}(i,j+\frac{1}{2}) - u_y^{l+\frac{1}{2}}(i,j-\frac{1}{2})\right] \\
l &= l+1 \qquad\qquad (D.9) \\
u_x^{l+\frac{1}{2}}(i+\frac{1}{2},j) &= u_x^{l-\frac{1}{2}}(i+\frac{1}{2},j)e_x^{(3)}(i+\frac{1}{2},j) \\
&\quad -e_x^{(4)}(i+\frac{1}{2},j)\left[p_x^l(i+1,j) - p_x^l(i,j) + p_y^l(i+1,j) - p_y^l(i,j)\right] \\
u_y^{l+\frac{1}{2}}(i,j+\frac{1}{2}) &= u_y^{l-\frac{1}{2}}(i,j+\frac{1}{2})e_y^{(3)}(i,j+\frac{1}{2}) \\
&\quad -e_y^{(4)}(i,j+\frac{1}{2})\left[p_x^l(i,j+1) - p_x^l(i,j) + p_y^l(i,j+1) - p_y^l(i,j)\right]
\end{aligned}
$$

In PML regions (Figure D.1), the coefficients in (D.9) are explicitly expressed as

$$
\begin{aligned}
e_x^{(1)}(i,j) &\equiv \exp\left[\frac{-\alpha_x(i,j)h}{\kappa(i,j)}\right] \\
e_x^{(2)}(i,j) &\equiv \frac{1-\exp\left[\frac{-\alpha_x(i,j)h}{\kappa(i,j)}\right]}{\triangle\alpha_x(i,j)} \qquad\qquad (D.10) \\
e_x^{(3)}(i+\frac{1}{2},j) &\equiv \exp\left[\frac{-\alpha_x(i+\frac{1}{2},j)h}{\kappa(i+\frac{1}{2},j)}\right] \\
e_x^{(4)}(i+\frac{1}{2},j) &\equiv \frac{1-\exp\left[\frac{-\alpha_x(i+\frac{1}{2},j)h}{\kappa(i+\frac{1}{2},j)}\right]}{\triangle\rho_x(i+\frac{1}{2},j)\frac{-\alpha_x(i+\frac{1}{2},j)}{\kappa(i+\frac{1}{2},j)}} \\
e_y^{(1)}(i,j) &\equiv \exp\left[\frac{-\alpha_y(i,j)h}{\kappa(i,j)}\right] \\
e_y^{(2)}(i,j) &\equiv \frac{1-\exp\left[\frac{-\alpha_y(i,j)h}{\kappa(i,j)}\right]}{\triangle\alpha_y(i,j)} \qquad\qquad (D.11) \\
e_y^{(3)}(i,j+\frac{1}{2}) &\equiv \exp\left[\frac{-\alpha_y(i,j+\frac{1}{2})h}{\kappa(i,j+\frac{1}{2})}\right] \\
e_y^{(4)}(i,j+\frac{1}{2}) &\equiv \frac{1-\exp\left[\frac{-\alpha_y(i,j+\frac{1}{2})h}{\kappa(i,j+\frac{1}{2})}\right]}{\triangle\rho_y(i,j+\frac{1}{2})\frac{-\alpha_y(i,j+\frac{1}{2})}{\kappa(i,j+\frac{1}{2})}}
\end{aligned}
$$

In lossless acoustic region where the α's are zero, these coefficients become

$$\begin{aligned} e_x^{(1)}(i,j) &= e_y^{(1)}(i,j) \equiv 1 \\ e_x^{(2)}(i,j) &= e_y^{(2)}(i,j) \equiv \frac{h}{\triangle\kappa(i,j)} \\ e_x^{(3)}(i+\frac{1}{2},j) &= e_y^{(3)}(i+\frac{1}{2},j) \equiv 1 \\ e_x^{(4)}(i,j+\frac{1}{2}) &\equiv \frac{h}{\triangle\rho_x(i,j+\frac{1}{2})} \\ e_y^{(4)}(i,j+\frac{1}{2}) &\equiv \frac{h}{\triangle\rho_y(i,j+\frac{1}{2})} \end{aligned} \tag{D.12}$$

An interface normal to the x axis between a lossless medium with (κ, ρ, $\alpha_x = 0$, $\alpha_y = 0$) and a PML medium with (κ, ρ, α_x, $\alpha_y = 0$) is reflectionless. In the left and right side PML regions (PML-LEFT and PML-RIGHT) in Figure D.1, $\alpha_y = 0$ and α_x increases from zero in inner surface to α_{max} in outer surface quadratically. The top and bottom PMLs are analogous to $\alpha_y = 0$, and α_y increasing from zero on the inner surface to α_max in outer surface quadratically. The corner regions are the combination of the associated side regions. A perfectly reflecting boundary condition is enforced ($p_x = 0$, $p_y = 0$) at the outer boundary. The profile of α_x and α_y in PML-RIGHT is the mirror image of that in PML-LEFT. The profile of α_x and α_y in PML-TOP is the mirror image of that in PML-BOTTOM.

$$\begin{aligned} \text{PML-LEFT} \qquad & \alpha_x(s,j) = \alpha_{max}\left(\tfrac{m-s}{m}^2\right) \qquad \alpha_y = 0 \\ & s = \tfrac{1}{2}, 1, \tfrac{3}{2}, ..., m-\tfrac{3}{2}, m-1 \quad j = 1, 2, ..., N_y \\ \text{PML-BOTTOM} \qquad & \alpha_y(i,s) = \alpha_{max}\left(\tfrac{m-s}{m}^2\right) \qquad \alpha_x = 0 \\ & s = \tfrac{1}{2}, 1, \tfrac{3}{2}, ..., m-\tfrac{3}{2}, m-1 \quad i = 1, 2, ..., N_x \end{aligned} \tag{D.13}$$

The maximum attenuation (α_{max}) at the boundary is set to give an amplitude reduction of 1/10 for propagation a distance of one grid:

$$e^{-\frac{\alpha_{max}\triangle}{c\kappa}} = 0.1 \tag{D.14}$$

which gives 106 dB absorption for an eight-layer PML with quadratic variation (D.13), considering wave propagation through twice (in to the PML and back out again).

The coefficients $e_x^{(1)}$, $e_x^{(2)}$, $e_y^{(1)}$, $e_y^{(2)}$ have the contribution from both the attenuation coefficient associated with mass density (α^*) and the attenuation coefficient associated with compressibility (α). The α^* indicates the damping mechanism in solids, which is introduced here merely for mathematic attenuation in the PML region. In fluid acoustic medium, only the α is taken into account for usual compressibility

attenuation mechanism in fluids. Assuming the attenuation coefficient α is frequency independent, the attenuation in the acoustic medium ($\alpha^* = 0, \alpha$) can be implemented by plugging in the attenuation coefficient (α) into the $e_x^{(3)}$, $e_x^{(4)}$, $e_y^{(3)}$, $e_y^{(4)}$ of (D.10) and (D.11) and calculating $e_x^{(1)}$, $e_x^{(2)}$, $e_y^{(1)}$, $e_y^{(2)}$ as lossless formulations in (D.12).

The implementation of the 3D formulation is trivial [95].

REFERENCES

[1] L. E. Kinsler, A. R. Frey, A. B. Coppens, and J. V. Sanders, *Fundamentals of Acoustics*. 4th ed. New York: John Wiley & Sons, 2000.

[2] B. Carlin, *Physical Acoustics — Principles and Methods*, Vol. I, part B. New York: Academic Press, 1964.

[3] C. J. Hellier, *Handbook of Nondestructive Evaluation*. New York: McGraw-Hill, 2001.

[4] GE Panametrics, Technical notes.

[5] NDT Resource Center, 2003, http://www.ndt-ed.org/EducationResources/CommunityCollege/Ultrasonics/Introduction/history.htm.

[6] L. C. Lynnworth, "Industrial applications of ultrasound - A review II: Measurements, tests, and process control using low intensity ultrasound," *IEEE Trans. Sonics Ultrason.*, vol. SU-22, no. 2, pp. 71–101, March 1975.

[7] R. B. Thompson, "Ultrasonic measurement of mechanical properties," in *Proc. IEEE Int. Ultrason. Symp.*, 1996, pp. 735–744.

[8] J. F. Greenleaf and C. M. Sehgal, *Biological System Evaluation with Ultrasound*. New York: Springer-Verlag, 1992.

[9] A. Goldstein, *Medical Ultrasonic Diagnostics*. New York: Academic Press, 1999.

[10] L. M. Hinkelman, T. L. Szabo, and R. C. Wagg, "Measurements of ultrasonic pulse distortion produced by human chest wall," *J. Acout. Soc. Am.*, vol. 101, pp. 2365–2373, 1997.

[11] B. A. Kimmelman, "Medical diagnostic ultrasound: A retrospective on its 40th anniversary," Eastmann Kodak, Rochester, NY, 1988. Copies may be obtained from Dr. B. B. Goldberg, chairman of the AIUM Archives Committee.

[12] NCRP, "Biological effects of ultrasound: Mechanism and clinical implications," National Council on Radiation Protection and Measurements, Bethesda, MD, Tech. Rep. 74, 1983.

[13] W. N. McDicken, *Diagnostic Ultrasonics: Principles and Use of Instruments*. 2nd ed. New York: John Wiley & Sons, 1981.

[14] A. D. Pierce, *Acoustics: An Introduction to Its Physical Principles and Applications*. Woodbury, NY: The Acoustical Society of America, 1989.

[15] A. G. Webster, "Acoustical impedance and the theory of horns and of the phonograph," *Proc. Natl. Acad. Sci.*, vol. 5, pp. 275–282, 1919.

[16] A. E. Kennelly and K. Kurokawa, "Acoustic impedance and its measurement," *Proc. Am. Acad. Arts Sci.*, vol. 61, pp. 3–37, 1921.

[17] G. S. Kino, *Acoustic Waves: Devices, Imaging, and Analog Signal Processing.* Englewood Cliffs, NJ: Prentice-Hall, Inc., 1987.

[18] Herzfeld and Litovitz, *Absorption and Dispersion of Ultrasonic Waves.* New York: Academic Press, 1959.

[19] K. Raum and W. D. O'Brien, Jr., "Pulse-echo field distribution measurement technique for high-frequency ultrasound sources," *IEEE Trans. Ultrason. Ferroelect. Freq. Contr.*, vol. 44, no. 4, pp. 810–815, July 1997.

[20] B. G. Lucas and T. G. Muir, "The field of a focusing source," *J. Acout. Soc. Am.*, vol. 72, no. 4, pp. 1289–1296, 1982.

[21] F. A. Firestone, "Flaw Detecting Device and Measuring Instrument," U.S. Patent 2,280,226, 1942.

[22] M. I. Skolnik, *Introduction to Radar Systems.* New York: McGraw-Hill, 1962.

[23] A. Macovski, "Ultrasonic imaging using arrays," *Proc. IEEE*, vol. 67, pp. 484–495, 1979.

[24] A. Briggs, *Acoustic Microscopy.* Oxford: Clarendon Press, 1992.

[25] A. Goldstein, "Ultrasonic imaging," in *Encyclopedia of Medical Devices and Instrumentation*, J. G. Webster, Ed. New York: John Wiley & Sons, 1988.

[26] A. Fenster and D. B. Downey, "3-dimensional ultrasound imaging: A review," *IEEE Engin. Med. Biol.*, vol. 15, pp. 41–51, 1996.

[27] R. C. Gonzalez and P. Wintz, *Digital Image Processing.* 2nd ed. Reading, MA: Addison-Wesley, 1987.

[28] M. O'Donnell, S. Y. Emelianov, A. R. Skovoroda, M. A. Lubinski, W. F. Weitzel, and R. C. Wiggins, "Quantitative elasticity imaging," in *Proc. IEEE Ultrason. Symp.*, 1993, pp. 893–903.

[29] J. Ophir, I. Cesoedes, H. Ponnekanti, Y. Yazdi, and X. Li, "Elastography: A quantitative method for imaging the elasticity of biological tissues," *Ultrasonic Imag.*, vol. 13, pp. 111–134, 1991.

[30] J. Oppenheim and A. S. Willsky, *Signals and Systems.* Englewood Cliffs, NJ: Prentice Hall, 1985.

[31] M. Born and E. Wolf, *Principles of Optics*. New York: Academic Press, 1975.

[32] A. Papoulis, *Systems and Transforms with Applications in Optics*. Melbourne, FL.: R. E. Krieger Publishing Co., Inc., 1981.

[33] K. H. Hu, A. I. Nelson, R. R. Legault, and M. P. Steinberg, "Feasibility of using plastic film packages for heat processed foods," *Food Technol.*, vol. 19, no. 9, pp. 236–240, 1955.

[34] A. I. Nelson and M. P. Steinberg, "Retorting foods in plastic bags," *Food Eng.*, vol. 28, no. 1, pp. 92–93, 1956.

[35] A. I. Nelson, K. H. Hu, and M. P. Steinberg, "Heat processible food films," *Mod. Packag.*, vol. 20, no. 10, pp. 173–179, 1956.

[36] N. H. Mermelstein, "The retort pouch in the U.S.," *Food Technol.*, vol. 30, no. 2, pp. 28–37, 1976.

[37] F. E. Long, "Flexible packages now withstand heat processing temperatures of foods," *Package Engineering*, vol. 7, no. 3, pp. 63–80, 1962.

[38] A. F. Badenhop and H. P. Milleville, "Institutional size retort pouches," *Food Processing*, vol. 44, pp. 82–86, 1980.

[39] C. E. Morris, "Return of the pouch," *Food Eng.*, vol. 2, pp. 44–46, 1989.

[40] R. A. Lampi, "Flexible packaging for thermoprocessed foods," in *Advance Food Research*, E. M. Mark, C. O. Chichester, and G. F. Stewart, Eds. New York: Academic Press, 1977, pp. 305–428.

[41] J. P. Adams, W. R. Peterson, and W. S. Otwell, "Processing of seafood in institutional-sized retort pouches," *Food Technol.*, vol. 37, pp. 123–127, 1983.

[42] T. D. Durance and L. S. Collins, "Quality enhancement of sexually matured chum salmon oncorhynchus keta in retort pouches," *J. Food Science*, vol. 56, no. 5, pp. 1282–1286, 1991.

[43] R. A. Kluter, D. T. Nattress, C. P. Dunne, and R. D. Popper, "Shelf life evaluation of cling peaches in retort pouches," *J. Food Science*, vol. 59, no. 4, pp. 849–865, 1994.

[44] P. J. Delaquis, R. Baker, and A. R. McCurdy, "Microbiological stability of pasteurized ham subjected to a secondary treatment in retort pouches," *J. Food Protection*, vol. 49, no. 1, pp. 42–46, 1986.

[45] J. F. Steffe, J. R. Williams, M. S. Chinnan, and J. R. Black, "Energy requirements and costs of retort pouch vs. can packaging system," *Food Technol.*, vol. 34, no. 9, pp. 39–43, 1980.

[46] J. R. Williams, J. F. Steffe, and J. R. Black, "Sensitivity of selected factors on costs of retort pouch packaging systems," *Food Technol.*, vol. 37, pp. 92–100, 1983.

[47] C. L. Harper, B. S. Blakistone, J. B. Litchfield, and S. A. Morris, "Developments in food package integrity testing," *Food Technol.*, vol. 6, no. 10, pp. 336–340, 1995.

[48] F. A. Paine and H. Y. Paine, *A Handbook of Food Packaging*. London: Blackie Academic & Professional, 1992.

[49] A. Ozguler, "Inspection of defects in the seal region of flexible food packages using the ultrasonic pulse-echo technique," Ph.D. dissertation, University of Illinois, Urbana, IL, 1999.

[50] A. B. Blakistone, S. W. Keller, J. E. Marcy, G. H. Lacy, C. H. Hackney, and W. H. Carter, Jr., "Contamination of flexible pouches challenged by immersion biotesting," *J. Food Protection*, vol. 59, pp. 764–767, 1996.

[51] H. M. C. Put, H. Van Doren, W. R. Warner, and J. T. Kruiswjik, "The mechanism of microbiological leak spoilage of canned foods: A review," *J. Appl. Bacteriol.*, vol. 35, pp. 7–27, 1972.

[52] H. M. C. Put, W. R. Witvoet, and W. R. Warner, "The mechanism of leaker spoilage of canned foods: Biophysical aspects," *J. Food Protection*, vol. 43, pp. 488–497, 1980.

[53] S. McEldowney and M. Fletcher, "The effect of physical and microbiological factors on food container leakage," *J. Appl. Bacteriol.*, vol. 69, pp. 190–205, 1990.

[54] J. D. Floros, "Critical leak size and package integrity," in *Packaging Technologies and Inspection News*, vol. IV, pp. 3, PTI, Tukahoe, NY, 1994.

[55] G. Howard and R. Duberstein, "A case of penetration of 0.2 micron rated membrane filters by bacteria," *J. Parental Drug. Assoc.*, vol. 34, no. 2, pp. 95–102, 1980.

[56] R. A. Lampi, "Retort pouch: The development of a basic packaging concept in today's high technology era," *J. Food Processing Engin.*, vol. 4, pp. 1–18, 1980.

[57] S. W. Keller, J. E. Marcy, B. A. Blakistone, and G. H. Lacy, "Bioaerosol exposure method for package integrity testing," *J. Food Protection*, vol. 59, no. 7, pp. 768–771, 1995.

[58] L. Axelson, S. Cavlin, and J. Nordstörm, "Aseptic integrity and microhole determination of packages by electrolytic conductance measurement," *Packag. Technol. Science*, vol. 3, pp. 141–162, 1990.

[59] J. E. Gilchrist, U. S. Rhea, R. W. Dickerson, and J. E Campbell, "Helium leak test for micron-sized holes in canned foods," *J. Food Protection*, vol. 48, no. 10, pp. 856–860, 1985.

[60] C. Chen, B. Harte, C. Lai, J. Pestka, and D. Henyon, "Assessment of package integrity using a spray cabinet technique," *J. Food Protection*, vol. 54, no. 8, pp. 643–647, 1991.

[61] D. Rose, "Risk factors associated with post-processing contamination of heat sealed semi-rigid packaging," Campden & Chorleywood Food Research, Gloucestershire, UK: Campden & Chorleywood Food and Drink Association, Memorandum No. 708, 1994.

[62] A. Ozguler, S. A. Morris, and W. D. O'Brien, Jr., "Ultrasonic monitoring of the seal quality in flexible food packages," *Polym. Eng. Science*, vol. 41, no. 5, pp. 830–839, May 2001.

[63] A. A. Safvi, H. J. Meerbaum, S. A. Morris, A. L. Harper, and W. D. O'Brien, Jr., "Acoustic imaging of defects in flexible food packages," *J. Food Protection*, vol. 60, no. 3, pp. 309–314, March 1997.

[64] S. A. Morris, A. Ozguler, and W. D. O'Brien, Jr., "New sensors help improve heat-seal microleak detection. Part 1," *Packag. Technol. Engin.*, vol. 7, no. 7, pp. 42–49, July 1998.

[65] S. A. Morris, A. Ozguler, and W. D. O'Brien, Jr., "New sensors help improve heat-seal microleak detection. Part 2," *Packag. Technol. Engin.*, vol. 7, no. 8, pp. 52–68, August 1998.

[66] Mathworks, Inc., *MATLAB Documentation*. 2003.

[67] C. H. Frazier, Q. Tian, A. Ozguler, S. A. Morris, and W. D. O'Brien, Jr., "High contrast ultrasound images of defects in food package seals," *IEEE Trans. Ultrason. Ferroelect. Freq. Contr.*, vol. 47, no. 3, pp. 530–539, May 2000.

[68] H. Eriksson, P. O. Börjesson, P. Ödling, and N.-G. Holmer, "A robust correlation receiver for distance estimation," *IEEE Trans. Ultrason. Ferroelect. Freq. Contr.*, vol. 41, no. 5, pp. 596–603, 1994.

[69] A. M. Sabatini, "Correlation receivers using laguerre filter banks for modeling narrow-band ultrasonic echoes and estimating their time-of-flights," *IEEE Trans. Ultrason. Ferroelect. Freq. Contr.*, vol. 44, no. 6, pp. 1253–1263, November 1997.

[70] H. Vincent Poor, *An Introduction to Signal Detection and Estimation.* 2nd ed. New York: Springer-Verlag, 1994.

[71] Q. Tian, B. Sun, A. Ozguler, S. A. Morris, and W. D. O'Brien, Jr., "Parametric modeling in food package defect imaging," *IEEE Trans. Ultrason. Ferroelect. Freq. Contr.*, vol. 47, no. 3, pp. 635–643, May 2000.

[72] K. Raum, A. Ozguler, S. A. Morris, and W. D. O'Brien, Jr., "Channel defect detection in shelf-stable food packages using high-frequency pulse-echo imaging," *IEEE Trans. Ultrason. Ferroelect. Freq. Contr.*, vol. 45, no. 1, pp. 30–40, January 1998.

[73] A. Ozguler, S. A. Morris, and W. D. O'Brien, Jr., "Evaluation of defects in the seal region of food packages using the ultrasonic contrast descriptor, ΔBAI," *Packg. Technol. Sci.*, vol. 12, pp. 161–171, 1999.

[74] A. Ozguler, S. A. Morris, and W. D. O'Brien, Jr., "Evaluation of defects in seal region of food packages using the backscattered amplitude integral (BAI) technique," in *Proc. IEEE Int. Ultrason. Symp.*, 1997, pp. 689–692.

[75] N. N. Shah, P. K. Rooney, A. Ozguler, S. A. Morris, and W. D. O'Brien, Jr., "A real-time approach to detect seal defects in food packages using ultrasonic imaging," *J. Food Protection*, vol. 64, no. 9, pp. 1392–1398, September 2001.

[76] D. T. Sandwell, "Biharmonic spline interpolation of geos-3 and seasat altimeter data," *Geophys. Res. Lett.*, vol. 14, no. 2, pp. 139–142, 1987.

[77] T. Sato and S. Wadaka, "Incoherent ultrasonic imaging system," *J. Acoust. Soc. Am.*, vol. 58, no. 5, pp. 1013–1017, 1975.

[78] X. Yin, S. A. Morris, and W. D. O'Brien, Jr., "Investigation of spatial sampling resolution of the real-time ultrasound pulse-echo BAI-mode imaging technique," in *Proc. IEEE Int. Ultrason. Symp.*, Atlanta, GA, October 2001, pp. 729–732.

[79] J. J. Bowman, T. B. A. Senior, and P. L. E. Uslenghi, *Electromagnetic and Acoustic Scattering by Simple Shapes*, New York: Hemisphere Publishing, 1987.

[80] P. M. Morse and K. U. Ingard, *Theoretical Acoustics.* New York: McGraw-Hill, 1968.

[81] J. J. Faran, Jr., "Sound scattering by solid cylinders and spheres," *J. Acoustic. Soc. Am.*, vol. 23, pp. 405–418, July 1951.

[82] P. P. Silvester and R. L. Ferrari, *Finite Elements for Electrical Engineers.* 2nd ed. Cambridge: Cambridge University Press, 1990.

[83] R. F. Harrington, *Field Computation by Moment Methods.* New York: The Macmillan Co., 1968.

[84] K. S. Yee, "Numerical solution of initial boundary value problems involving Maxwell's equations in isotropic media," *IEEE Trans. Antennas Propag.*, vol. 14, no. 3, pp. 302–307, May 1966.

[85] A. Taflove, *Computational Electromagnetics: The Finite-Difference Time-Domain Method.* Norwood, MA: Artech House, 1995.

[86] K. S. Yee and J. S. Chen, "The finite-difference time-domain (FDTD) and the finite-volume time-domain (FVTD) methods in solving Maxwell's equations," *IEEE Trans. Antennas Propag.*, vol. 45, pp. 354–363, March 1997.

[87] K. L. Shlager and J. B. Schneider, "A selective survey of the finite-difference time-domain literature," *IEEE Antennas Propag. Mag.*, vol. 37, no. 4, pp. 39–57, August 1995.

[88] J. P. Berenger, "A perfectly matched layer for the absorption of electromagnetic waves," *J. Comput. Phys.*, vol. 114, pp. 185–200, October 1994.

[89] A. Taflove, "Review of the formulation and applications of the finite-difference time-domain method of numerical modeling of electromagnetic wave interactions with arbitrary structures," *Wave Motion*, vol. 10, no. 10, pp. 547–582, 1988.

[90] C. W. Manry, Jr., S. L. Broschat, and J. B. Schneider, "Higher-order FDTD methods for large problems," *J. Appl. Comput. Electromag. Soc.*, vol. 10, no. 2, pp. 17–29, 1995.

[91] H. Chang and R. M. D'Angelo, "Experimental verification of finite-difference model for ultrasonic evaluation of complex structures," in *Proc. IEEE Int. Ultrason. Symp.*, 1990, pp. 965–969.

[92] P. H. Johnston and E. I. Madaras, "Modeling the pulse-echo response of a two-dimensional phase-insensitive array for NDE of layered media," in *Proc. IEEE Int. Ultrason. Symp.*, 1988, pp. 1021–1025.

[93] R. Stacey and J. P. Weight, "Ultrasonic pulse-echo responses from targets in solid media using finite difference methods," *IEE Proceedings-A*, vol. 140, no. 4, pp. 303–316, 1993.

[94] L. P. Martin, D. H. Chambers, and G. H. Thomas, "Experimental and simulated ultrasonic characterization of complex damage in fused silica," *IEEE Trans. Ultrason. Ferroelect. Freq. Contr.*, vol. 49, no. 2, pp. 255–265, February 2002.

[95] X. Yuan, D. Borup, J. W. Wiskin, M. Berggren, R. Eidens, and S. A. Johnson, "Formulation and validation of Berenger's PML absorbing boundary for the FDTD simulation of acoustic scattering," *IEEE Trans. Ultrason. Ferroelect. Freq. Contr.*, vol. 44, no. 4, pp. 816–822, July 1997.

[96] J. P. Berenger, "Improved PML for the FDTD solution of wave-structure interaction problems," *IEEE Trans. Antennas Propag.*, vol. 45, no. 3, pp. 466–473, March 1997.

[97] J. A. Jensen, *User's Guide for the FIELD-II Program (Version 2.70).* Oersted*DTU, DK, 2001, http://www.es.oersted.dtu.dk/staff/jaj/field.

[98] V. A. Dumane and P. M. Shanker, "Use of frequency diversity and Nakagami statistics in ultrasonic tissue characterization," *IEEE Trans. Ultrason. Ferroelect. Freq. Contr.*, vol. 48, no. 5, pp. 1139–1146, September 2001.

[99] R. Lerch, H. Landes, and H. T. Kaarmann, "Finite element modeling of the pulse-echo behavior of ultrasound transducers," in *Proc. IEEE Int. Ultrason. Symp.*, 1994, pp. 1021–1025.

[100] E. Skudrzyk, *The Foundations of Acoustics.* New York: Springer-Verlag, 1971.

[101] I. A. Hein and W. D. O'Brien, Jr., "Current time-domain methods for assessing tissue motion by analysis from reflected ultrasound echoes - A review," *IEEE Trans. Ultrason. Ferroelect. Freq. Contr.*, vol. 40, no. 2, pp. 84–102, March 1993.

[102] W. S. Janna, *Engineering Heat Transfer.* 2nd ed. Boca Raton, FL: CRC Press LLC, 2000.

[103] Thermophysical Properties Research Center of Purdue University, *Thermophysical Properties of Matter, Vol. 1–13.* New York: IFI/Plenum, 1970-79.

[104] Matweb, Material Property Data, 2002, http://www.matweb.com.

[105] AUDION ELEKTRO, *AUDIONVAC (101/105) Heat Sealer Manual.* 1996.

VITA

Xiangtao Yin was born in Nanjing, China, on December 21, 1971. He received the BSEE and MSEE degrees with an acoustics major from Nanjing University, China in 1994 and 1997, respectively. He came to United States to pursue his PhD study in 1997. He studied in George Mason University from 1997 to 1998. He has been in the PhD program of the Department of Electrical and Computer Engineering of the University of Illinois since 1998.

From 1994 to 1995, he worked as an application engineer in Jiangsu Jin Ling Science and Technology Company, Nanjing, China, where he participated in developing an adaptive noise cancellation algorithm for a microphone phase array.

His graduate study and research span a broad range of topics in acoustics, ultrasonics, electromagnetics, numerical modeling, and signal processing. At Nanjing University, he worked as a graduate research assistant on design, simulation and prototyping of surface acoustic wave signal processing devices for high frequency wireless communication and radar applications. At George Mason University, he worked as a graduate research assistant in the Institute for Computational Sciences and Informatics on quantitative assessment of numerical models for atmospheric applications. At the University of Illinois, he worked from 1998 to 2000 as a graduate research assistant in the Center for Computational Electromagnetics to develop a fast numerical algorithm for large scale complex scatterer radar cross section prediction problems. He has been a graduate research assistant working on ultrasonic nondestructive evaluation techniques in Bioacoustics Research Laboratory (BRL) under the direction of Dr. William D. O'Brien, Jr. since August 2000.

During his academic pursuit and research practices, he has developed a strong background and interest in experimental and numerical simulation aspects of wave-structure interaction problems. Currently, his research in BRL involves experimental spatial sampling analysis of ultrasonic imaging techniques, numerical modeling of pulse-echo defect detection system, evaluation of the fundamental subwavelength defect detection mechanisms and finite element modeling of acoustic wave propagation in human head for hearing protection purpose.

He is a student member of IEEE and a student member of the Acoustic Society of America.